===== **PHYSICS** =====

Bragg Reflection as a Mechanism of Light Localization in One-Dimensional Systems

A. P. Vinogradov and A. M. Merzlikin
Presented by Academician A.M. Dykhne March 4, 2004

This study is devoted to investigating the mechanism of localization of electromagnetic waves in one-dimensional systems. Historically, the problem on the wave localization appeared in quantum mechanics of disordered media [1], in which the single-particle wave function ψ was described by the Schrödinger equation

$$\nabla^2\psi + k^2\psi = 0. \qquad (1)$$

Here, $k^2 = \dfrac{2m(E - V(x))}{\hbar^2}$, $V(r)$ is the random potential, E is the energy of state, and $\hbar$ is Planck's constant. It is known (see [1, 2]) that, in a one-dimensional system, all states are localized.

The distribution of an electric field E in a randomly layered system is described by a similar equation:[1]

$$\nabla^2 E + k^2 E = 0, \qquad (2)$$

where $k^2 = \dfrac{\varepsilon(x)\omega^2}{c^2}$, ω is the frequency, $\varepsilon(x)$ is the electric permittivity, and c is the speed of light. The similarity of Eqs. (1) and (2) allows us to assume that the light is also localized in a randomly layered system. The light localization is characterized by certain features. In contrast to quantum mechanics, which operates most often with the subbarrier tunneling ($E < \max[V(x)]$), electrodynamics deals with above-barrier scattering ($\varepsilon(x) > 0$).

In addition, the specific character of electrodynamics consists in the fact that the emphasis is concentrated on the scattering problem rather than on the eigenvalue problem. We imply as the light localization the total

---

[1] For simplicity, we assume that the wave propagation occurs along a normal to the layers.

Institute of Theoretical and Applied Electrodynamics,
Joint Institute of High Temperatures,
Russian Academy of Sciences,
Izhorskaya ul. 13/19, Moscow, 127412 Russia

light reflection from the half-space filled with a nonabsorbing disordered material [3, 4]. This assumes the transmission coefficient t to be exponentially dropped with increasing sample thickness L. The characteristic scale of this drop, i.e., the localization length L_{loc}, is defined as

$$L_{\text{loc}} = \frac{1}{\gamma_{\text{loc}}} = -\lim_{L \to \infty} \frac{L}{\langle \ln|t| \rangle}, \qquad (3)$$

where γ_{loc} is the Lyapunov index and $\langle \cdot \rangle$ denotes averaging over an ensemble of realizations.

It is worth noting that the exponential wave attenuation is also observed in ordered systems (e.g., photon crystals) at frequencies lying in the forbidden zone. However, if the mechanism responsible for the formation of forbidden zones in ordered systems is well known (this is the Bragg reflection), the physical mechanism of the light localization, despite the presence of the rigorous mathematical results of [2, 4, 5] and problems exactly solved in [4, 6–10], remains unknown. Moreover, in the literature [11], there exists an opinion that the causes leading to wave attenuation in random and ordered systems are totally different.

In what follows, we try to look at these phenomena from a unified point of view. For this purpose, we use the formalism of T matrices [12].[2] We now consider properties of T matrices. Taking into account that $\det T = 1$ for any system, the T matrix of any system (cell) of thickness d can be represented in the form

$$T = S \left\|
\begin{matrix}
\exp(ik_{\text{ef}}d) & 0 \\
0 & \exp(-ik_{\text{ef}}d)
\end{matrix}
\right\| S^{-1}.$$

The T matrix of a system consisting of N such systems (cells) differs from the T matrix of a single system only in the replacement of d by $L = Nd$. This makes it possible to consider k_{eff} and the equation $\text{Tr}(T) = 2\cos(k_{\text{eff}}d)$ (where T relates to one cell) as an effective wave number and the dispersion relation, respectively. The for-

---

[2] A T matrix relates the amplitudes of incoming and outgoing waves on each side of the system under consideration.
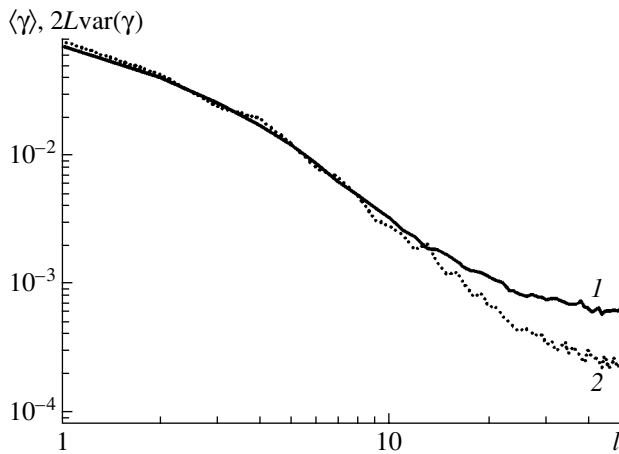
$\langle\gamma\rangle, 2L\mathrm{var}(\gamma)$

Fig. 1. Dependences of $\langle\gamma\rangle$ (*1*) and $2L\mathrm{var}(\gamma)$ (*2*) on the length *l* of eliminated Bragg reflectors. The electric permittivity is equiprobably distributed within the interval [2, 13]. The wavelength is $k_0 d = 0.5$ and the thickness of the entire system attains $L = 2000$ layers. Averaging is performed over 400 realizations.
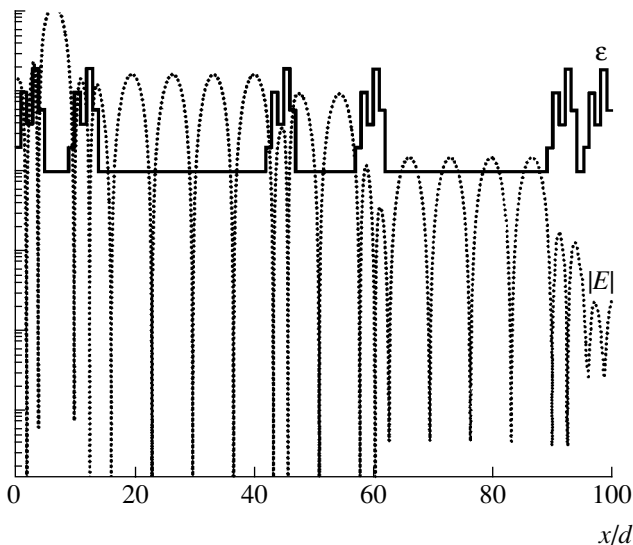
Fig. 2. Electric-field modulus $|E|$ of the propagating electromagnetic wave in the system of Bragg reflectors and electric permittivity ε as functions of the depth of the electromagnetic-field penetration into the system.

bidden zones of the regular system are found from the condition $|\mathrm{Tr}(T)| > 2$ [13, 14].

After detailed examination of the field distribution in a disordered system, we noticed that the system contains regions in which the field amplitude sharply drops, whereas the field amplitude in the remaining regions is almost unchanged. On the average, exponential decay is observed. Our calculations indicate that regions with the sharp field dropping, which we call Bragg reflectors, have T matrices with traces exceeding 2 in absolute value; i.e., in them, the wave has a purely

imaginary effective wave number. In the regions in which the field amplitude is nearly constant, the field has the real effective wave number k (correspondingly, $|\mathrm{Tr}T| < 2$). Our numerical experiment showed that the size of the Bragg reflectors with the maximum $\gamma_{\mathrm{loc}}^{\mathrm{Tr}} = \frac{1}{L}\mathrm{Im}\left[\arccos\frac{\mathrm{Tr}(T)}{2}\right]$ is on the order of $\frac{2\pi}{k_0\langle\sqrt{\varepsilon}\rangle}$ (in the case, when $k_0 d < 1$) or is equal to two layers at higher frequencies. In other words, relatively small regions of a random system mainly contribute to the localization.

This observation implies that the presence of the Bragg reflectors is a necessary and sufficient condition of the light localization in the system. In the course of numerical simulation, we found a realization of a random system containing no Bragg reflectors. It turns out that the wave in such a system is not localized: $\gamma = 0$. Systems with short- and long-range correlations, which are known from the literature and demonstrate delocalization [2, 3, 15], also contain no Bragg reflectors.

To obtain representative results, we considered an algorithm of eliminating the Bragg reflectors from an arbitrary random system. We examined successively all layers in a certain random realization and calculated the trace of the T matrix in the region consisting of the given layer and previous $l - 1$ layers. If this region was proved to be the Bragg reflector, then it was replaced by a random sequence with the same length but with the trace of the T matrix smaller than 2 in absolute value. In this case, only realizations free of the Bragg reflectors of shorter length were taken into account. After examination of the entire system, we arrived at a disordered system that contained only Bragg reflectors consisting of more than l layers. Figure 1 shows the quantities $\langle\gamma\rangle$ and $\mathrm{var}(\gamma)$ as functions of l. In order to obtain this dependence, we performed averaging over the ensemble of initial realizations and the algorithm of cutting out the Bragg reflectors was successively applied for lengths equal to 2, 3, ..., l. As is seen, eliminating the Bragg reflectors from the system results in a sharp drop of $\langle\gamma\rangle$ (an increase in L_{loc}). In other words, in the absence of the Bragg reflectors, an electromagnetic wave is delocalized; i.e., the presence of the Bragg reflectors is necessary for the appearance of localization. The sufficiency of this condition follows from the fact that, in numerical experiments for a system of Bragg reflectors randomly localized in vacuum, the exponential drop of the transition coefficient is nearly always observed (Fig. 2).

To summarize, we can conclude that the effect of light reflection from both regular and disordered nonabsorbing systems is determined exclusively by the presence of Bragg reflectors in the system. In these Bragg reflectors, the effective wave number is purely imaginary. In this case, the problem on above-barrier scattering is reduced to that on subbarrier tunneling.

REFERENCES

1. P. W. Anderson, Phys. Rev. **109**, 1492 (1958).
2. K. Ishii, Prog. Theor. Phys. Suppl. **53**, 77 (1973).
3. P. Sheng, *Introduction to Wave Scattering, Localization, and Mesoscopic Phenomena* (Academic Press, London, 1995).
4. V. I. Klyatskin and A. I. Saichev, Usp. Fiz. Nauk **162**, 161 (1992) [Sov. Phys. Usp. **162**, 231 (1992)].
5. N. F. Mott, Adv. Phys. **50**, 865 (2001).
6. A. A. Abrikosov, Solid State Commun. **37**, 997 (1981).
7. V. Freilikher, M. Pustilnik, and I. Yurkevich, Phys. Rev. Lett. **73**, 810 (1994).
8. I. M. Suslov, Zh. Éksp. Teor. Fiz. **83**, 1079 (1982) [Sov. Phys. JETP **56**, 612 (1982)].
9. D. R. Grempel, S. Fishman, and R. E. Prange, Phys. Rev. Lett. **49**, 833 (1982).
10. S. Fishman, D. R. Grempel, and R. E. Prange, Phys. Rev. B **29**, 4272 (1984).
11. S. A. Bulgakov and M. Nieto-Vesperinas, Waves Random Media **7**, 183 (1997).
12. A. P. Vinogradov and A. M. Merzlikin, Dokl. Akad. Nauk **381**, 472 (2001) [Dokl. Phys. **46**, 832 (2001)].
13. H. F. Kramers, Physica **2**, 483 (1935).
14. B. Y. Tong, Phys. Rev. **175**, 710 (1968).
15. Z. Ye and A. Alvarez, Phys. Rev. Lett. **80**, 3503 (1998).

Translated by Yu. Vishnyakov

===================== **PHYSICS** =====================

Mechanism of the Appearance of Ball Lightning from Usual Lightning

V. P. Torchigin

Presented by Academician A.F. Andreev March 31, 2004

Received February 4, 2004

In [1–3], a hypothesis of the optical nature of ball lightening was discussed. According to this hypothesis, ball lightning is a thin spherical layer of compressed air, where intense white light circulates over all possible directions. Such a layer has an index of refraction higher than that of the surrounding air and presents a thin-film light guide trapping light circulating in it. In turn, circulating light generates electrostriction pressure and compresses air in this layer. As was shown in [1], the behavior of the spherical compressed-air layer according to theoretical analysis of its motion along the gradient of the refractive index of the inhomogeneous atmosphere coincides with the observed motion of ball lightning. The most intriguing features of the behavior of ball lightning such as its penetration through narrow slots and window glasses, as well as mechanisms of the penetration of ball lightning into the cabins of flying aircraft, are explained in [3].

In the present work, mechanisms of the appearance of ball lightning upon the electric discharge of usual linear lightning are analyzed in the framework of the above concept of the nature of ball lightning. The basic problem is the determination of conditions under which light usually propagating along straight lines circulates along closed paths within a thin spherical layer of compressed air. An analogue with the formation of a soap bubble is very useful. As is known, a soap bubble arises if a soap film manages to take an almost closed-surface shape. There are one-dimensional spatial optical solitons that are stable plane infinite films of intense light propagating in a homogeneous nonlinear optical medium whose index of refraction depends on the light intensity [4]. If this film is rolled into an infinite cylindrical surface whose axis is perpendicular to the direction of light propagation, light circulates perpendicularly to the generatrices of this surface. Then, instead of the infinite cylindrical film, one can consider a film in the form of the barrel-like surface of revolution with finite length, where light is concentrated in the maxi-

mum-diameter section. Finally, similar to the collapse of a hole in a soap film when forming a soap bubble, two holes at the edges of the barrel-like film collapse, and a light bubble is formed [2]. We now consider how this mechanism can be realized when ball lightning arises in nature.

A usual lightning stroke is accompanied by the formation of a cylindrical shock wave due to large current in the lightning core. In this case, the air temperature increases up to 25000–30000°C, and the current duration is equal to about 100 μs [5]. The air pressure in the pressure shock attains 0.3 GPa, the air density is by an order of magnitude larger than that under normal conditions, and the cylindrical wave expands with a velocity of 1.6×10^4 m/s, which is higher than the speed of sound in the atmosphere by a factor of about 50 [6]. Under these conditions, the index of refraction of air in the pressure shock is equal to $n \simeq 1.0027$. This value is sufficient for the formation of a thin-film cylindrical light guide from the pressure shock. This light guide completely traps light circulating around the axis of a cylinder with a diameter of 10 cm, which is the typical diameter of ball lightning. In 1 μs, light undergoes 1000 revolutions around the cylinder axis, and the cylinder radius increases by 1.6 cm. According to estimates, the energy density emitted by a heated gas in the pressure shock is insufficient for the formation of an energy clot of hundreds of kilojoules [1].

The processes that can proceed sequentially and/or simultaneously and lead to the accumulation of energy in the pressure shock with further formation of ball lightning are the following.

(i) Accumulation of light energy in the pressure shock in time.

(ii) Concentration of light energy in a domain near the maximum diameter of the barrel-like cylindrical layer.

(iii) Self-compression of the barrel-like cylindrical layer in width.

(iv) Collapse of two holes in the barrel-like cylindrical layer that leads to the formation of a spherical layer.

The first process occurs because the pressure shock is optically transparent [5]. In this process, the light-

---

Institute of Informatics, Russian Academy of Sciences,
ul. Vavilova 30/6, Moscow, 117900 Russia
e-mail: v_torchigin@mail.ru

energy density increases by a factor of 1000 per microsecond, because the radiation energy of heated air is added at each revolution to the energy of light circulating around the cylinder axis. The radiation energy of heated air in the pressure shock is recovered due to the linear-lightning current. The second process is attributed to the features of propagating whispering-gallery light waves in the barrel-like cylindrical layer, whose shape varies with time [2]. The third process, width self-compression of the barrel-like cylindrical layer, where light circulates along closed trajectories, is an analogue of the known process of self-focusing of a rectilinearly propagating intense laser beam. In both cases, light propagating in peripheral sections deviates to the side where the index of refraction is maximal. The index of refraction in the barrel-like cylindrical layer is maximal at the center of the layer. Self-focusing and self-compression proceed until the thickness of radiation becomes commensurate with the light wavelength. The thickness of the barrel-like cylindrical layer decreases from several centimeters to several micrometers, i.e., by four orders of magnitude. Therefore, the light energy density increases by four orders of magnitude. The joint action of these processes can lead to a necessary increase in the light energy density in the pressure shock.

Let us estimate the self-compression time to be sure that light is not strongly scattered in this time. We assume that radiation sections most remote from the center of the cylindrical layer are in an inhomogeneous medium, where the gradient of the index of refraction is directed to the center of the cylindrical layer and equals $g_n = 2\dfrac{\Delta n}{h}$, where $n \simeq 10^{-6}$ is the maximum increase in the index of refraction at the center of the layer and $h \simeq 3$ cm is the thickness of the cylindrical layer. According to the eikonal equation, $\dfrac{d^2 h}{dt^2} = 2g_n c^2$. In this case, peripheral sections reach the center in time $t = c^{-1}\left(\dfrac{h}{2g_n}\right)^{1/2} \simeq 0.4\ \mu\text{s}$, which is much shorter than the lifetime of radiation in air.

The fourth process, collapse of two holes in the barrel-like cylindrical layer, is not accompanied by the concentration of light energy but is very important for the formation of ball lightning. Much as the formation of a soap bubble requires a soap film whose shape is close to the shape of the soap bubble, the formation of "light bubbles" requires the corresponding object, i.e., the pronounced barrel-like cylindrical layer.

We consider facilities that can be used to obtain ball lightning in the laboratory. First, it is necessary to ensure the appearance of a barrel-like cylindrical layer; i.e., the barrel-like shape of the cylindrical layer must become more pronounced with time. To this end, the velocity of the pressure shock at the edges of the barrel-
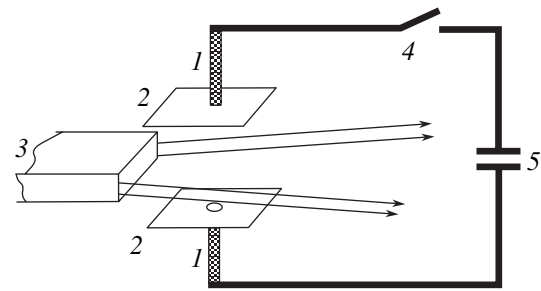

Fig. 1. Layout of a setup for the laboratory generation of ball lightning: (*1*) electrodes, (*2*) plates, (*3*) nozzle for the supply of a light-gas jet to the center of the interelectrode gap, (*4*) knife-switch, (*5*) capacitor battery.

like cylindrical layer must be made lower than the velocity at the center. This can be ensured by placing certain means decreasing the velocity of the pressure shock near the upper and lower bases of the barrel-like cylindrical layer. In the laboratory setup shown in Fig. 1, parallel plates *2* near electrodes *1* between which an electric discharge occurs are used as these means. In addition, substances increasing the velocity of the pressure shock can be placed in the domain near the maximum diameter of the barrel-like cylindrical layer. Any gases including water vapor or gas mixtures with the molecular masses lower than the average molecular mass of air can be used as such substances [7]. Figure 1 shows nozzle *3* through which a light gas mixture is blown into the interelectrode gap.

We note that water in a certain form is present in all known experiments on the artificial formation of ball lightning. Water is used when forming long-lived plasmoids by means of an electric discharge [8]. It is also used when luminous spherical structures are formed by an electric explosion of thin wires by intense electric current from a capacitor battery [9, 10]. The above discussion makes it possible to explain successful attempts [8] to obtain ball lightning in the laboratory. In those experiments (Fig. 2), surface *1* of water poured into a polyethylene vessel was used as one of the electrodes. Between the first electrode and second electrode *4*, water *2* in an amount of about 0.1 ml was placed at a distance of 3–8 mm from the water surface. A light gas in the form of water vapor between electrodes was formed upon the water evaporation induced by an electric discharge of a capacitor battery that had a capacitance of 600 μF and was charged up to 5 kV. Egorov and Stepanov [8] emphasized that there was an optimum potential difference between electrodes. This is likely associated with the water evaporation regime. Water is sprayed at high voltage.

In those experiments, the electrodes had such a shape that a hemispherical rather than cylindrical shock wave was formed at the initial stage. In this case, the index of refraction in the pressure shock increases due to an increase in both the temperature and amount of gas when water is evaporated. The velocity of propagat-
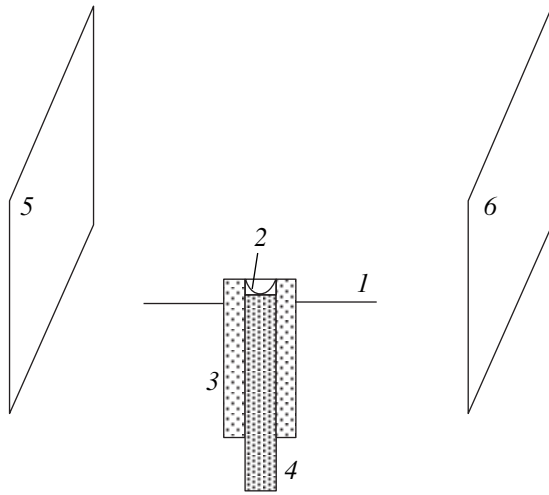
Fig. 2. Shape and arrangement of the electrodes for the formation of ball lightning in the laboratory [8]: (*1*) water surface in a vessel, (*2*) water drop, (*3*) quartz tube, (*4*) second electrode, and (*5*) and (*6*) hot and cold plates for deviating ball lightning towards the cold plate.

ing the pressure shock in radial directions decreases near the liquid surface. As a result, the maximum-diameter section of the pressure shock lies above the liquid surface. In this case, the pressure shock has only one hole, which collapses under the action of forces that arise due to intense light and compress the gas. Similarly, a hole in a soap bubble collapses due to surface tension forces in a soap film. In experiments [8], the capacitor battery had an energy of 7.5 kJ, which is obviously insufficient. The energy of long-lived ball lightning, where intense light compresses air so that the loss of light in air considerably decreases, must be much higher [1]. Multiple discharges can be used in the following manner. The first discharge evaporates water and prepares the pressure shock. Then, the subsequent discharges introduce additional light energy into the pressure shock. Such pulsed discharges are often observed in nature [5].

Thus, the above hypothesis provides an explanation of the strange behavior of ball lightning in nature and mechanism of its appearance. Moreover, this hypothesis enables one to determine the functions of the individual parts of the setup used to obtain ball lightning and to outline the methods of increasing the lifetime of ball lightning. The hypothesis under consideration can be tested in the following simple experiment. It is necessary to place two plates *5* and *6* with different temperatures such as is shown in Fig. 2. The plates create the gradient of the index of refraction of air in the horizontal direction, and the arising ball lightning must deviate towards the colder plate.

REFERENCES

1. V. P. Torchigin, Dokl. Akad. Nauk **389**, 41 (2003) [Dokl. Phys. **48**, 108 (2003)].

2. V. P. Torchigin, Laser Phys. **13**, 919 (2003).

3. V. P. Torchigin and A. V. Torchigin, Phys. Scr. **68**, 388 (2003).

4. H. A. Haus, *Waves and Fields in Optoelectronics* (Prentice-Hall, Englewood Cliffs, 1983; Mir, Moscow, 1988).

5. É. M. Bazelyan and Yu. P. Raĭzer, *Physics of Lightning and Lightning Protection* (Fizmatlit, Moscow, 2001).

6. N. M. Kuznetsov and Yu. P. Raĭzer, Shock Wave, in *Encyclopedia of Physics* (Bol'shaya Ross. Éntsiklopediya, Moscow, 1998), Vol. 5, pp. 206–211.

7. A. L. Polyakova, Velocity of Sound, in *Encyclopedia of Physics* (Bol'shaya Ross. Éntsiklopediya, Moscow, 1994), Vol. 4, pp. 546–548.

8. A. I. Egorov and S. I. Stepanov, Zh. Tekh. Fiz. **72** (12), 102 (2002) [Tech. Phys. **47**, 1584 (2002)].

9. L. I. Urutskoev, V. I. Liksonov, and V. G. Tsinoev, Zh. Radioélektron., No. 3 (2000); http://jre.cplire.ru/win/mar00/4/text.html.

10. A. L. Pirozerski and S. E. Emelin, http://balllightning.narod.ru.

Translated by R. Tyapaev

═══════════════════ **PHYSICS** ═══════════════════

Dust Particles in a Track Plasma
Produced by a Proton Beam

Academician V. E. Fortov*, V. A. Rykov**, V. I. Vladimirov*, L. V. Deputatova*, V. I. Molotkov*, O. F. Petrov*, V. S. Filinov*, A. P. Budnik**, P. P. D'yachenko**, K. V. Rykov**, and A. V. Khudyakov**

The fundamental property of plasma produced by accelerated ions is the existence of its track structure. Fast charged particles penetrating a medium at an initial velocity much higher than the Bohr velocity ($v_B = 2.18 \times 10^8$ cm s^{-1}) produce electron-ion pairs in a very narrow region near the particle trajectory. In the process of deceleration, the ion energy decreases almost continuously since, in each interaction with atoms of a medium, only a small portion of the ion energy is lost. As a result, a monoenergetic ion beam virtually does not lose its energy to the end of its path. The use of accelerated ions for producing plasma significantly changes the experimental conditions compared to studies carried out previously [1–3]. A beam of ionizing particles has a small divergence caused by ion-atomic collisions. The beam current can be sufficiently high for ion tracks to be significantly overlapped in their lifetime. In this case, the plasma becomes quasi-homogenous.

The goal of the present study is the experimental investigation of the behavior of dust particles in track plasmas produced by an accelerated proton beam. The results obtained made it possible to observe new effects associated with collective phenomena in plasma-dust structures. The analysis of these phenomena can be of interest for both fundamental science and practical use in plasma and beam technologies, which are vigorously being developed at present.

The experiments under consideration were carried out at the Russian State Research Center, Institute of Physics and Power Engineering, at the EP-2.5 acceler-

ator. The layout of the experimental setup is shown in Fig. 1. A 2-MeV horizontal proton beam was directed into an experimental cell through a window covered by thin titanium foil. This window, 1.2 cm in diameter, also served as both a diaphragm and a reference electrode. The beam current was 1 μA. Passing through the foil, protons lost 0.5 MeV and heated it to 150°C.

The experimental cell had the shape of a rectangular parallelepiped with a base side of 8 cm and height of 12 cm. The lateral cell boundaries were made of glass. The cell was illuminated by a plane laser beam with a neck from 100 to 200 μm in size. The laser light scattered by dust particles was transformed into a video image using a CCD video camera.

Inside the experimental cell, a high-voltage electrode 3 cm in diameter was located at a distance of 7 cm from the reference electrode. This electrode was used to perform several basic functions, in particular, to set up the electric field inside the experimental cell after the negative or positive potential has been applied and to measure the proton current inside the evacuated experimental cell. It was also used as a probe for estimating the plasma floating potential inside the gas-filled cell. In the absence of an external applied electric field, the floating potential U_f for the gases under study (He, Kr, Xe) was within the range from –0.4 to –0.5 V. The charge q of a dust particle was estimated by the formula

$$q = CU_f, \qquad (1)$$

where C is the dust particle capacity. Polydisperse particles made of cerium dioxide with a mean diameter of 1 μm were used in the experiments. The charges calculated according to expression (1) lay within the range from 140 to 170 units of negative electron charge.

The gas–dust mixture was produced by a sudden injection of gas flow from a metering tank with constant volume into a container with a gridlike bottom in which the dust particles being studied were placed.

The experimental results obtained with krypton gas for two pressure values are shown in Figs. 2–4. In the first case (Fig. 2), the 870-torr pressure was chosen to

─────────────

* *Institute of Extreme States in Thermal Physics,*
  Joint Institute of High Temperatures,
  Russian Academy of Sciences,
  ul. Izhorskaya 13/19, Moscow, 127412 Russia
** *State Research Center Leĭpunskiĭ Institute of Physics*
  and Power Engineering,
  ul. Bondarenko 1, Obninsk, Kaluga oblast,
  249020 Russia
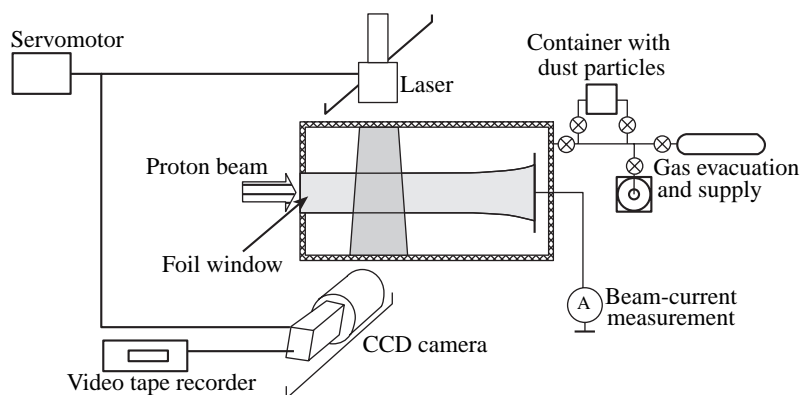 *e-mail: div@ihed.ras.ru; rykov@ippe.obninsk.ru*

Fig. 1. Layout of the experimental setup.

prevent decelerated protons from reaching the high-voltage electrode forming an external electric field. The volume of recombining track plasma emitting light characteristic of each gas is clearly seen in Fig. 2. In the case of a negative potential of several hundred volts (from 100 to 500 V) applied to the electrode, the formation of an extended region (void) free of particles was observed. This region is more clearly expressed, the higher the negative potential. In the case of disconnecting the source of the potential from the electrode or using the source to supply the electrode with a positive potential, the void is filled with dust particles.

At a reduced pressure (150–400 torr), when protons can reach the electrode, after the gas–dust mixture has been injected, dust particles form a vortex located near the electrode and below the proton beam (Fig. 3). The vortex rotation velocity increases with the potential. At larger concentrations of dust particles, they aggregate for several minutes into a cloud with clearly pronounced boundaries (Fig. 4). In the cloud, instabilities periodically arise leading to changes in the cloud shape.

All structures are conserved for tens of minutes, and, as was mentioned in [4], in the absence of an external electric field, the dust component is stratified. It is important that dust particles in the vortex and in the cloud do not hit the electrode but form a flow around its flat part at a distance of several millimeters and then move away from the electrode edges.

Dissociative recombination is the basic mechanism of neutralizing charged particles in low-temperature plasma at a relatively low degree of ionization, characteristic of nuclear-excited and track plasma. In a time on the order of about 1 ns, monatomic ions of noble gases are transformed into molecular ions and the recombination reaction is realized:

$$e + A_2^+ \rightarrow A + A^*, \qquad (2)$$

where A is an atom of noble gas, A_2^+ is its molecular ion, and A* is an excited atom. In steady-state conditions, the number of electron-ion pairs produced by
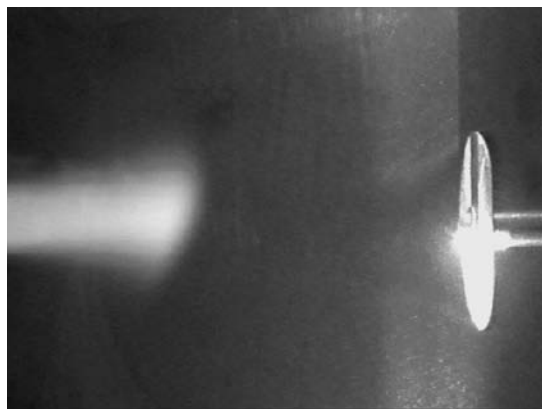

Fig. 2. Proton beam does not reach the high-voltage electrode. The experiment is performed with krypton gas under a pressure of 870 torr and with CeO_2 dust particles; the voltage is 300 V; the proton energy is 2 MeV; the beam current is 1 μA.
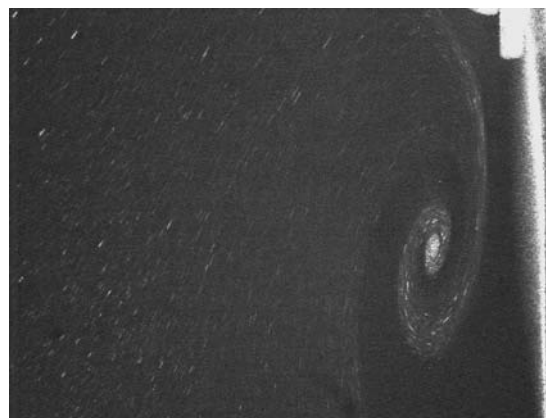

Fig. 3. Vortex in a dust structure. Krypton pressure is 128 torr; CeO_2 dust particles are used; the voltage is 200 V; the proton energy is 2 MeV; the beam current is 1 μA.

protons is equal to the number of recombinations. This leads to the following equation for determining the electron and ion concentrations:

$$\frac{IE}{ewV} = \alpha n_- n_+, \qquad (3)$$

where I is the proton beam current, E is the proton energy, e is the proton charge, w is the energy required to produce an electron-ion pair by a fast ion (for all gases, it is about 30 eV), α is the dissociative-recombination factor, $n_\pm$ is electron (or ion) concentration, and V is the volume occupied by the plasma. This volume is observed visually in the experimental cell, since the electron-ion recombination causes luminescence characteristic of the gas under study. Estimation of electron-ion concentration according to Eq. (3) yields $n_+ \approx n_- \approx 1 \times 10^{11}$ cm^{-3}. The electron temperature was estimated according to the floating potential using the relationship [5]

$$T_e \text{ (eV)} \approx e|U_f| \times 10^{-1}, \qquad (4)$$

the ion temperature T_i being assumed to be equal to room temperature. The equation of dust-particle charging was solved numerically:

$$\frac{dq}{dt} = I_+ - I_-. \qquad (5)$$

The currents of positive ions I_+ and electrons I_- per dust particle were calculated according to the formulas of [3, 6]. The values of charges for mean-diameter dust particles corresponded to 130–160 electron-charge units and were in good agreement with estimates based on formula (1).

The following arguments should be taken into account for explanation of the dust-particle behavior in a track plasma. The proton beam introduces energy into the cell at a rate of about 2 J s^{-1}, then convective gas flow entrains dust particles upwards. Then, ions accelerated by the electric field transfer their momentum to gas atoms in multiple collisions and set the gas in motion towards the negative electrode [7, 8]. In addition, each dust particle is shot through by a proton for about 10 μs. In this case, two to five secondary electrons with energies of about 2 eV are knocked out from a dust particle, and each proton is capable of shooting through several dust particles. This mechanism of changing a charge plays the leading role at low gas pressures, whereas in our experimental conditions, the basic process is changing a charge according to mechanism (5).

In our experiment, the external-field intensity near the high-voltage electrode attains several thousand V m^{-1}. In the case of a negative potential of the probing electrode, dust particles having a negative charge are pushed out
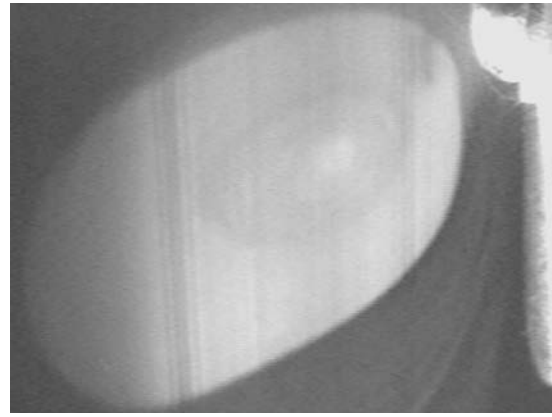
Fig. 4. Dust-particle cloud. Helium, pressure is 523 torr; CeO_2 dust particles are used; the voltage is 200 V; the proton energy is 2 MeV; the beam current is 1 μA.

from the near-axis region of the experimental cell by the electric field (Fig. 2). Dust particles colliding with the proton beam abruptly ascend due to convection. In the case that the proton beam occupies the entire near-axis region of the experimental cell, far from high-voltage electrode, the basic mechanism initiating the combined motion of dust particles and the gas toward the electrode is gas acceleration by ions and entrainment of dust particles. This conclusion is confirmed by an increase in the dust-particle velocity with elevating modulus of the negative potential. However, in the immediate vicinity of the electrode, the field intensity is sufficient for repelling dust particles. This is confirmed by the existence of a void gap near the electrode. The maximum gap is observed in the vicinity of the boundaries, where the field intensity is the highest. Convective flows cause vertical motion of dust particles.

Thus, in our experiments, the collective motion of cerium dioxide dust particles was observed for the first time in plasma formed as a result of deceleration of a proton beam generated by a particle accelerator. Compact vortex structures rotating about their axes with a large number of dust particles were discovered. Evolving dense dust clouds with clearly pronounced boundaries were also observed. Under invariable conditions, dust structures of both types exist for tens of minutes. The behavior of dust particles critically depends on the intensity of the external electric field.

ACKNOWLEDGMENTS

the Program of the Presidium of the RAS "Thermal Physics and Mechanics of Extremely Intense Actions."

REFERENCES

1. V. E. Fortov, A. P. Nefedov, V. M. Torchinsky, *et al.*, Phys. Lett. A **258**, 305 (1999).

2. V. E. Fortov, V. I. Vladimirov, L. V. Deputatova, *et al.,* Dokl. Akad. Nauk **366**, 184 (1999) [Dokl. Phys. **44**, 279 (1999)].

3. V. E. Fortov, A. P. Nefedov, V. A. Rykov, *et al.*, Phys. Lett. A **284**, 118 (2001).

4. V. I. Vladimirov, L. V. Deputatova, V. A. Rykov, *et al.*, in *Proc. XVII Int. Conf. "Physics of Extremal States of a Medium–2002"* (El'brus, 2002), pp. 142–143.

5. Yu. P. Raizer, *Physics of Gas Discharge* (Nauka, Moscow, 1987).

6. B. M. Smirnov, *Aerosols in Gases and Plasmas* (IVTAN, Moscow, 1990).

7. V. E. Fortov, V. I. Vladimirov, L. V. Deputatova, *et al.*, Dokl. Akad. Nauk **380**, 610 (2001) [Dokl. Phys. **46**, 697 (2001)].

8. V. I. Vladimirov, L. V. Deputatova, V. A. Rykov, *et al.*, Zh. Éksp. Teor. Fiz. **120**, 353 (2001) [JETP **93**, 313 (2001)].

Translated by G. Merzon

===== **PHYSICS** =====

Statistical Laws of Macroprocesses: Random Walks in the Momentum Space

Academician G. S. Golitsyn

Received May 31, 2004

1. In this paper, it is shown that a large number of statistical laws for a wide variety of natural processes and phenomena can be described under two natural assumptions. These are the ergodicity and the smallness of the correlation time of random forces acting on the system under consideration compared to the time of the system response to these forces. In other words, this implies that the system performs random walks in the momentum space. We first consider continuous stochastic processes. In the study, examples of these processes are locally homogeneous and isotropic Kolmogorov–Obukhov turbulence, described in 1941 mainly on the basis of the similarity and dimensionality considerations; the sea roughness frequency spectrum obtained by Zakharov in 1966; and the statistical structure of the planet surface relief. Then, we consider the event flow statistics. We propose the theoretic-probability interpretation to formula (4), which is basic in the study and provides an insight into many empirical cumulative frequency–size distributions such as, e.g., the Gutenberg–Richter law for the earthquake repetition rate. Using simple but practically important formula (13), we estimate the generation rate for the energy released in events. As an illustration, we calculate the generation rate for the energy released in earthquakes and find that it is on the order of 0.1% of the total geothermal-flux power.

2. The foundation for describing natural processes can be given by the Newton equation

$$\frac{dp}{dt} = f, \qquad (1)$$

where p is the momentum and f is the force. For simplicity, we refer both quantities to the unit mass of the system under consideration. Thus, we arrive at the velocity–acceleration relation. We assume that the forces are random, their correlation time being much smaller than the system response time. Then, in the lim-

iting case, we can represent the correlation function of the random forces in the form

$$B_f(\bar{\tau}) = \langle f(t+\tau)f(t) \rangle = \sigma_f^2 \tau_0 \delta(\tau) \equiv \varepsilon \delta(\tau). \qquad (2)$$

In this case, we also assume that the forces represent a stochastic stationary time process and the distributed systems possess the ergodicity property, i.e., the ensemble averages of separate parts of the system are equal to their time averages. Numerical calculations [1] show that this is fulfilled already when the number of ensemble members is on the order of 10 or greater. In Eq. (2), σ_f^2 is the random force variance and τ_0 is the characteristic minimum time of the system response. For example, in the case of the locally homogeneous and isotropic Kolmogorov–Obukhov turbulence (in what follows, it is referred to as KO41), we have $\tau_0 = \left(\frac{\nu}{\varepsilon}\right)^{1/2}$, where ν is the kinematic viscosity and ε is the kinetic energy generation/dissipation rate in the fluid [2, 3]. For other media, it can be shown that $\varepsilon = \frac{dF}{dt}$, where F is the free deformation energy [4]. Below, in Section 4, we show that the condition $\tau \gg \tau_0$ and all conclusions made of it are well fulfilled already for $\tau \geq 4\tau_0$.

Correlation function (2) corresponds to the energy frequency spectrum

$$E_f(\omega) = \int_0^\infty B_f(\tau)\cos\omega\tau = \varepsilon = \text{const}, \qquad (3)$$

i.e., to the white noise. For the acceleration field of Lagrangian particles in the KO41 inertia interval, this was shown in [3].

As far as the momentum is concerned, integrating Eq. (1) and using [2], we derive the following expression for the structure function:

$$D_p(\tau) = \langle [p(t+\tau) - p(t)]^2 \rangle = 2\varepsilon\tau, \qquad (4)$$

the $p(t)$ process being stochastic with stationary increments. A formula of type (4) was first published in 1944

Obukhov Institute of Atmospheric Physics,
Russian Academy of Sciences,
Pyzhevskiĭ per. 3, Moscow, 119017 Russia

in [5] in the part of the book concerning the presentation of the KO41. The history of numerous rediscoveries of this formula and the range of its applicability in hydrodynamics are presented in [2]. Here, we emphasize that it is a direct consequence of the assumption $\tau \gg \tau_0$ leading to Eq. (2) and, further, to Eq. (11).

Structure function (4) is associated with the spectrum [2]

$$E_p(\omega) = \varepsilon\omega^{-2}, \tag{5}$$

i.e., with the red noise. As is shown in [1, 6], in the case of turbulence, the following results of KO41 for the Lagrangian-particle displacement spectrum are obtained:

$$E_r = \varepsilon\omega^{-4}, \tag{6}$$

which are associated with the structure displacement function

$$\langle \delta r^2 \rangle = r^2 = \varepsilon\tau^3. \tag{7}$$

Hence, we obtain $\tau = \left(\dfrac{r^2}{\varepsilon}\right)^{1/3}$. Substituting this expression into Eq. (4), we arrive at the results of KO41 for the second spatial moments of the velocity field, which were derived by the authors of that theory from the similarity and dimensionality considerations. Here, these results are obtained by us only under the assumptions of the ergodicity and the condition $\tau \gg \tau_0$. It can be said that KO41 represents the projection onto the spatial coordinates (the Eulerian description) of the red noise of the Lagrangian-particle velocity field induced by the white noise of the random forces acting on the Lagrangian particles. Displacement spectrum (6) completely corresponds to the universal part of the rough-sea spectrum first derived by Zakharov [7], who used a more sophisticated approach. The spatial spectra for these two processes are obtained using the relation

$$E(k) = E(\omega)\frac{d\omega}{dk}, \tag{8}$$

which is derived under the assumptions of the ergodicity and the probability conservation at a change of variables, namely, the equality of the variances obtained by integrating $E(\omega)$ over frequencies or $E(k)$ over wavenumbers $k = \dfrac{2\pi}{r}$. In addition to this equation, the dispersion equation $\omega(k)$ should also be known. It takes the form $\omega = \varepsilon^{1/3}k^{2/3}$ in the case of KO41 and $\omega = (kg)^{1/2}$ in the case of waves on a fluid surface in the gravity field. Then, we obtain $E_u(k) = \varepsilon^{2/3}k^{-5/3}$ and $E_r(k) = \varepsilon^{1/2}k^{-5/2}$, where in the latter case, $\varepsilon = u_*g$ and u_* is the friction rate [1, 6] characterizing the momentum exchange

between the atmosphere and the underlying surface. For rough sea, the spatial velocity spectrum is derived from formulas (5), (8), and $\omega^2 = gk$ and turns out to equal $E_v(k) = u_*g^{1/2}k^{-3/2}$. It corresponds to the spatial structure function $D_v(r) = u_*g^{1/2}r^{1/2}$ and to the turbulent mixing coefficient

$$K(r) = r[D_v(r)]^{1/2} = u_*^{1/2}g^{1/4}r^{5/4}. \tag{9}$$

In these formulas, as in all the formulas of this study, we do not write numerical coefficients that should be determined from experimental data. We note the weaker dependence of turbulent mixing coefficient (9) on the spot size than in the case of the turbulent mixing in the three-dimensional locally homogeneous and isotropic turbulence, for which the exponent of r is equal to 4/3, as in the Richardson–Obukhov law [2].

As is shown in [8], the spatial spectrum of the Earth's surface relief is an example of the red noise in the wave space. In this case, the spectrum of slopes along which the relief-forming forces act is a white noise. The formula derived in [8] yields one million years as the lower estimate for the time scale of relief-forming processes and several tens of millions of years as the time scale for the formation and decay of supercontinents.

3. All the aforesaid ending with formula (5) can be applied to the description of event flows. Usually, cumulative histograms are plotted, especially when the sampling size in the form of the number of events $N(\geq E)$ for an observation interval is insufficient. Here, $N(\geq E)$ is the frequency of the events of a size equal to or greater than E. For the physical interpretation of such empirical probability distributions, the parameter E could advantageously be associated with the event energy. Sometimes, differential histograms

$$N(\geq E) = \int_E^{E_{max}} N(E)dE, \quad N(E) = E^{-1}N(\geq E), \tag{10}$$

are used, where the second equality is fulfilled with an accuracy to a numerical coefficient being usually on the order of unity. The quantity $N(E)$ is the empirical probability density for the flow of the events E.

In the interpretation expressed by formulas (9), it was shown in monograph [9] that the time standing for the event flow in relation (5) is actually the mean time of the occurrence of the event with an amplitude $\geq E$ in the flow, i.e.,

$$\tau = \tau(\geq E) = \frac{1}{N(\geq E)}. \tag{11}$$

Then, two important formulas follow from Eq. (5):

$$N(\geq E) = \frac{\varepsilon}{E}, \qquad (12)$$

$$EN(\geq E) = \varepsilon. \qquad (13)$$

Formula (13) provides an explanation for the fact that many empirical frequency–size distributions of the $N(\geq E) \sim E^{-n}$ type have exponents $n \approx 1$. Examples can be found in [1, 10]. These are tsunami $N(\geq h)$, where h is the height and $n = 1.01$; landslides $N(\geq m)$, where m is the ground mass and $n = 0.95$; and lakes $N(\geq S)$, where S is the lake area and $n = 0.93$–0.95 [11, 12].

The deviation of the empirical exponent n from unity can occur due to many reasons, such as an inadequate sampling size, its spatial and/or temporal nonuniformity, a dependence of the dimensionless numerical coefficient on some dimensionless similarity parameters characterizing the phenomenon, and finally the fact that the random-force spectrum can be frequency-dependent. For $n > 1$, the contribution of lower frequencies into the spectrum increases.

For earthquakes in the thin oceanic thrust or intense earthquakes with magnitude $m \geq 8$, the $N(\geq M) \sim M^{-n}$ law with $n \approx 1$ is also fulfilled [10]. Here, M is the seismic moment related to the magnitude by the equation

$$m = \frac{2}{3}\log M - 6.$$

Hence it follows for $m = 8$ that $M = 10^{21}$ N/m. The quantity M is related to the energy E_s of the seismic waves radiated in the case of the occurrence of the event by the empirical formula $E_s \sim 6 \times 10^{-5} M$, the quantity E_s amounting to 7% of the total energy of the event [1, 10].

4. Naturally, the question arises as to what is the meaning of the requirement that the times under consideration be much greater than the inherent time of the system τ_0. To answer this question, we choose the random-force correlation function in the form

$$B_f(\tau) = \frac{\varepsilon}{\tau_0}\exp\left(-\frac{\tau}{\tau_0}\right), \qquad (14)$$

which transforms into $\delta(\tau)$ in the limit $\tau_0 \longrightarrow 0$. On integrating (1) and averaging, the corresponding structure function for the momentum takes the form

$$D_p(\tau) = \varepsilon\tau_0\left[\frac{\tau}{\tau_0} - 1 + \exp\left(-\frac{\tau}{\tau_0}\right)\right]. \qquad (15)$$

With an accuracy better than 1%, we can already at $\frac{\tau}{\tau_0} = 4$ ignore the exponential term in this formula, arriving at the result

$$D_p(\tau) = \varepsilon(\tau - \tau_0) = \left\langle[\bar{\delta}p(\tau)]^2\right\rangle \approx \left\langle p^2(\tau)\right\rangle = E \quad (16)$$

and include the τ_0 dependence into formulas of type (12) and (13) in which a small quantity $E_0 = \varepsilon\tau_0$ is added to the quantity E.

5. In conclusion, we formulate the results obtained. Within the framework of the second moments and using stochastic-process theory and probability theory, many well-known results are derived and some empirical laws that have been long known are explained. These results are obtained under two natural assumptions, namely, the ergodicity and the smallness of the correlation time of random actions on the system under consideration compared to the time of the system response to external actions. By analogy with the Brownian motion, the processes being analyzed can be called random walks in the momentum space, and the parameter ε in our formulas can be considered as the diffusivity in the momentum space, as was done in 1958 by A.M. Obukhov for the Lagrangian-particle turbulence [13].

Throughout the entire study, we did not touch upon the question of numerical coefficients. These can be completely verified by the comparison with data of laboratory and numerical experiments and observation data. Moreover, these coefficients can also be dependent on dimensionless similarity parameters inherent in the problem under discussion. It is worth noting that almost all of the presented results can be obtained from the similarity and dimensionality considerations or on the basis of the so-called fastest-response principle [6–8]. Here, we propose the mathematical and physical substantiation of these approaches of heuristic nature.

REFERENCES

1. G. S. Golitsyn, in *Nonlinear Waves* (Institute of Applied Physics of the RAS, Nizhni Novgorod, 2003), pp. 117−132.

2. A. S. Monin and A. M. Yaglom, *Statistical Hydromechanics* (Fizmatgiz, Moscow, 1967), Vol. 2.

3. A. M. Yaglom, Dokl. Akad. Nauk SSSR **67**, 795 (1949).

4. L. D. Landau and E. M. Lifshitz, *Elasticity Theory* (Fizmatgiz, Moscow, 1978).

5. L. D. Landau and E. M. Lifshitz, *Mechanics of Continua* (GITTL, Moscow, 1944).

6. G. S. Golitsyn, Izv. Ross. Akad. Nauk, Fiz. Atm. Okeana **37** (4), 438 (2001).

7. V. E. Zakharov and N. N. Filonenko, Dokl. Akad. Nauk SSSR **170**, 1292 (1966).

8. G. S. Golitsyn, Fiz. Zemli, No. 7, 3 (2003).

9. W. Feller, *An Introduction to Probability Theory and Its Applications* (Wiley Text Books, New York, 1968), Chap. 13.

10. G. S. Golitsyn, Vychisl. Seĭsmologiya, No. 32, 138 (2001).

11. S. V. Ryanzhin, in *Proceedings of IV Int. Lake Ladoga Symp., 2002*, pp. 496–502.

12. D. Turcotte, *Chaos and Fractals in Geology and Geophysics* (Cambridge Univ. Press, Cambridge, 1997).

13. A. M. Obukhov, Adv. Geophys. **6**, 113 (1959); in *Atmospheric Diffusion* (Mir, Moscow, 1963).

Translated by M. Lebedev

=== **PHYSICS** ===

Suppression of Toroidal Alfvén Eigenmodes by the Density Gradient of Hot Ions in Tokamaks

A. B. Mikhaĭlovskiĭ*,**, M. S. Shirokov*,***, S. V. Konovalov*,****, and V. S. Tsypin*****

Presented by Academician A.M. Fridman March 2, 2004

Received April 12, 2004

Nowadays, two equilibrium toroidal configurations with different current profiles are considered as basic scenarios of operation of magnetic thermonuclear reactors such as ITER (International Thermonuclear Experimental Reactor) [1]. The first is an equilibrium configuration with a monotonic safety factor, i.e., with a positive magnetic shear. This configuration, as is expected, can provide a maximal power yield characterized by the parameter Q. The second is a configuration with a non-monotonic safety factor, i.e., with inverse shear. These configurations can demonstrate the best conditions for quasi-stationary reactor regimes. It is well known that, in the case of a large fraction of thermonuclear particles, they can generate various kinds of instabilities in the Alfvén frequency range, i.e., so-called Alfvén modes. In the case of the configurations with a monotonic safety-factor profile, the riskiest situation from the standpoint of hot-ion confinement is represented by toroidal Alfvén eigenmodes (TAEs). Therefore, the methods of suppression of these modes is a central problem in physics of magnetic thermonuclear reactors.

Depending on the relation between the shear s and the local inverse aspect ratio ϵ, two principal versions of analytical TAE theory were previously developed. One of

―――――――――――――

  * *Institute of Nuclear Fusion,
    Russian Research Centre Kurchatov Institute,
    pl. Akademika Kurchatova 1, Moscow,
    123182 Russia
    e-mail: mikh@nfi.kiae.ru;
    shirokovmephi@yandex.ru; konoval@nfi.kiae.ru*
 ** *Moscow Institute of Physics and Technology,
    Institutskiĭ per. 9, Dolgoprudnyĭ,
    Moscow oblast, 141700 Russia*
 *** *Moscow Engineering Physics Institute,
    Kashirskoe sh. 31, Moscow, 115409 Russia*
 **** *Naka Fusion Research Establishment,
    Japan Atomic Energy Research Institute*
***** *Physics Institute, University of São Paulo,
    Cidade Universitaria, 055008-90, Sao Paolo, Brazil
    e-mail: tsypin@fap01.if.usp.br*

them deals with the case $s > \epsilon$, (s and ϵ are shear and inverse aspect ratio, respectively; see, for example, [2]), whereas the other corresponds to the case $s < \epsilon$ [3]. Both these versions ignore the delocalizing (or localizing) effect of the density gradient of hot ions with large orbits [4–6]. (Physical aspects of this effect were analyzed in [7].) Recently, this effect was included into theory of so-called Alfvén cascades [8], which represent the Alfvén eigenmodes in discharges with a non-monotonic safety-factor profile, i.e., in discharges with an inverse shear. The goal of the present study is to investigate the role of the indicated effect in the TAE problem in the case $s \lesssim \epsilon$.

We are based on the linearized current-continuity equations $\nabla \cdot \tilde{\mathbf{j}} = 0$, where $\tilde{\mathbf{j}}$ is the perturbed current density. We use the transformations of this equation given in [9, Sections 7.1 and 29.1]. In addition, following [4–6], we supplement this equation with a term allowing for the density gradient of hot ions with large orbits.

We consider a perturbation (mode) consisting of the mth and $(m-1)$th poloidal harmonics and assume that it is localized in the vicinity of the radius $r = r_m$, where r_m satisfies the relationship $q(r_m) = \dfrac{m - 1/2}{n}$, where q is the safety factor and m and n are the poloidal and toroidal mode numbers, respectively. We also assume that $m > 1$. Similarly to [3], we introduce a dimensionless parameter $\hat{\omega} = \dfrac{\omega}{2\omega_0}$ instead of the mode frequency ω.

Here, $\omega_0 = \dfrac{v_A}{2q(r_m)R}$, v_A is the Alfvén velocity, and R is the major radius of the torus. The shear is assumed to be positive $(s > 0)$. Then, we take the function $y \equiv n[q(r) - q(r_m)]$ as a radial coordinate.

In analogy with [9], we characterize the perturbation field by displacements X_m and X_{m-1}. Then, we arrive at

the following set of equations for X_m and X_{m-1}:

$$\frac{d}{dy}\left\{\left[\hat{\omega}^2 - \left(y - \frac{1}{2}\right)^2\right]\frac{dX_m}{dy}\right\} - \frac{1}{s^2}\left[\hat{\omega}^2 - \left(y - \frac{1}{2}\right)^2 + h\right]X_m$$

$$= -\frac{5\epsilon}{4}\frac{d^2 X_{m-1}}{dy^2} + \frac{3\epsilon}{4s}\frac{dX_{m-1}}{dy} - \frac{\epsilon}{8s^2}X_{m-1}, \qquad (1)$$

$$\frac{d}{dy}\left\{\left[\hat{\omega}^2 - \left(y + \frac{1}{2}\right)^2\right]\frac{dX_{m-1}}{dy}\right\} - \frac{1}{s^2}\left[\hat{\omega}^2 - \left(y + \frac{1}{2}\right)^2 + h\right]X_{m-1}$$

$$(2)$$

$$= -\frac{5\epsilon}{4}\frac{d^2 X_m}{dy^2} - \frac{3\epsilon}{4s}\frac{dX_m}{dy} - \frac{\epsilon}{8s^2}X_m.$$

Here, h is the parameter describing the above effect of the density gradient of hot ions having large orbits. This parameter is determined by the relation

$$h = -\frac{\Omega_h}{4m\omega}\frac{n_{0h}}{n_{0c}}\kappa_h r_m, \qquad (3)$$

where $\kappa_h = \left(\dfrac{d\ln n_{0h}}{dr}\right)_{r = r_m}$, n_{0c} and n_{0h} are the densities of a thermal plasma and hot ions, respectively, for $r = r_m$; and Ω_h is the cyclotron frequency of hot ions. In the limit $h \longrightarrow 0$, Eqs. (1) and (2) are transformed into the corresponding equations of [3] with the replacement of m by $m - 1$. The factors in front of the toroidal terms on the right-hand sides of these equations ignore the additions taking into account the so-called poloidal beta coefficients, which are associated with the radial derivatives of the Shafranov shift (see [3] for details).

Similarly to [3], we introduce $X_+ = X_m + X_{m-1}$ and $X_- = X_m - X_{m-1}$, while the mode dimensionless frequency squared $\hat{\omega}^2$ we express in terms of the parameter g under the assumption that $\hat{\omega}^2 = \frac{1}{4} + \eta g$, where $\eta = \frac{5\epsilon}{8}$. In addition, following [3], we introduce $\epsilon^* = \frac{\eta}{s} \equiv \frac{5\epsilon}{8s}$, $z = \frac{y}{s}$ and ignore the terms as small as s. As a result, Eqs. (1) and (2) are reduced to

$$\epsilon^*(g + 1)X_+'' - \epsilon^*(g - c_0 + \hat{h})X_+$$
$$+ z(X_-'' - X_-) + (\epsilon^* c_1 + 1)X_-' = 0, \qquad (4)$$

$$\epsilon^*(g - 1)X_-'' - \epsilon^*(g + c_0 + \hat{h})X_-$$
$$+ z(X_+'' - X_+) - (\epsilon^* c_1 - 1)X_+' = 0. \qquad (5)$$

Here, the prime denotes the derivative with respect to z,

$$\hat{h} = \frac{4c_0}{1 + c\epsilon}\frac{h}{\epsilon} \equiv 0.64\frac{h}{\epsilon}, \qquad (6)$$

and the factors c_0, c_1, and c imply the same as in [3]; i.e., $c_0 = 0.2$, $c_1 = 1.2$, and $c = 0.25$.

Below, we assume that $\epsilon^* \gg 1$. Then, in analogy with [3], Eqs. (4) and (5) can be solved analytically.

We now assume that $g = c_0 - \hat{h} - \lambda$, where λ is a small parameter. In this case, similarly to [3], it follows from Eqs. (4) and (5) that

$$\epsilon^{*2}[c_1^2 - 2c_0(1 + c_0) - \hat{h}]X_+''$$
$$+ (\epsilon^* c_1 - 2c_0\epsilon^{*2}\lambda - z^2)X_+ = 0. \qquad (7)$$

The modes described by Eq. (7) we call even. Equation (7) has localized solutions if

$$c_1^2 - 2c_0(1 + c_0 - \hat{h}) > 0. \qquad (8)$$

In this case,

$$\lambda = \{c_1 - (2l + 1)[c_1^2 - 2c_0(1 + c_0 - \hat{h})]^{1/2}\}(2c_0\epsilon^*)^{-1}, \qquad (9)$$

where l is an integer satisfying the relation

$$l \ll c_0^2\epsilon^*[c_1^2 - 2c_0(1 + c_0 - \hat{h})]^{-1/2}. \qquad (10)$$

Equations (9) and (10) generalize the corresponding results of [3] for the case $\hat{h} \neq 0$.

We now assume $g = -c_0 - \hat{h} - \lambda$, where, as above, λ is considered to be a small parameter. Then, as in the case of Eq. (7), we arrive at the equation

$$\epsilon^{*2}[c_1^2 - 2c_0(1 + c_0) - \hat{h}]X_-''$$
$$+ (\epsilon^* c_1 + 2c_0\epsilon^{*2}\lambda + z^2)X_- = 0. \qquad (11)$$

The modes described by Eq. (11) we call odd.

The condition determining the existence of localized solutions to Eq. (11) has the form [cf. Eq. (8)]

$$c_1^2 - 2c_0(1 + c_0 + \hat{h}) > 0. \qquad (12)$$

Similarly to Eq. (9), the eigenvalues λ are found from the relation

$$\lambda = \{c_1 + (2l + 1)[c_1^2 - 2c_0(1 + c_0 + \hat{h})]^{1/2}\}(2c_0\epsilon^*)^{-1}. \qquad (13)$$

The mode radial number is confined by the condition [cf. Eq. (10)]

$$l \ll c_0^2\epsilon^*[c_1^2 - 2c_0(1 + c_0 + \hat{h})]^{-1/2}. \qquad (14)$$

As $\hat{h} \longrightarrow 0$, Eqs. (13) and (14) are consistent with the results of [3].

Equations (8) and (12) indicate that the effect of density gradient of hot ions is substantial provided that $|\hat{h}| \gtrsim 1$, i.e., using Eq. (6), that

$$|h| \gtrsim \epsilon. \qquad (15)$$

This effect results in the disappearance of even and odd modes for $h < 0$ and $h > 0$, respectively.

Taking into account Eq. (10), we can see that, in the case of even modes, positive values of h under the condition of the validity of Eq. (15) result in the narrowing

of the range of their radial numbers l. Then, Eq. (10) is reduced to the form $l \ll \epsilon^{3/2}(sh^{1/2})^{-1}$. This condition is not satisfied for $l = 1$ if (qualitatively) the following inequality takes place:

$$h > \frac{\epsilon^3}{s^2}. \tag{16}$$

At the same time, as follows from Eq. (9), provided that Eq. (16) is valid, the quantity λ is no longer a small parameter. Therefore, Eq. (16) can be interpreted as a condition for the disappearance of even modes with a small λ. The same analysis of odd modes in the case $h < 0$ shows that they disappear when

$$-h > \frac{\epsilon^3}{s^2}. \tag{17}$$

At the limits of applicability of the assumption $\epsilon > s$, i.e., for $s \simeq \epsilon$, inequalities (16) and (17) are reduced to inequality (15). The additional analysis of modes with large values of λ shows that such modes are not realized. Therefore, inequalities (16) and (17) can be considered as conditions for suppression of all modes of the type under discussion.

We also consider modes propagating in the direction of the equilibrium magnetic field ($\frac{\omega}{\Omega_h} > 0$). Then, according to Eq. (3), for a conventional decreasing profile of the hot-ion density ($\kappa_h < 0$), we have $h > 0$. In this case, the most important effect is the disappearance of odd modes. The qualitative condition of such a disappearance, which follows from Eqs. (15) and (3), has the form

$$m < \frac{1}{4\epsilon}\left|\kappa_h\right|r_m\frac{n_{0h}}{n_{0c}}\frac{\Omega_h}{\omega}. \tag{18}$$

Since we assume that $m > 1$, this condition can be satisfied only for a relatively strong effect of hot ions,

$$\left|\kappa_h\right|r_m\frac{n_{0c}}{n_{0h}}\frac{\Omega_h}{\omega} > 4\epsilon. \tag{19}$$

Even modes should disappear under the qualitative condition

$$m < \frac{s^2}{4\epsilon^3}\left|\kappa_h\right|r_m\frac{n_{0h}}{n_{0c}}\frac{\Omega_h}{\omega}. \tag{20}$$

Allowing for $m > 1$, we find that this condition can be met only for a relatively large shear:

$$2\epsilon^{3/2}\frac{n_{0c}}{n_{0h}}\frac{\omega}{\Omega\left|\kappa_h\right|r_m} < s < \epsilon. \tag{21}$$

Evidently, to satisfy the double inequality, it is also necessary to meet condition (19).

We now consider modes propagating in the direction opposite to the equilibrium magnetic field ($\frac{\omega}{\Omega_h} < 0$). In this case, the description of the effect of hot ions on the odd modes is similar to that in the case of even modes

for $\frac{\omega}{\Omega_h} > 0$. On the other hand, the general tendency of the effect of hot ions on even modes for $\frac{\omega}{\Omega_h} < 0$ turns out to be the same as on odd modes for $\frac{\omega}{\Omega_h} > 0$.

The analytical regularities considered above concerning the effect of the density gradient of hot ions having large orbits can be used as reference points in the numerical calculation of the TAE problems, which is based on the MISHKA-H-type code [6].

REFERENCES

1. ITER Physics Expert Group on Disruptions, Plasma Control, and MHD, ITER Physics Basis Editors, Nucl. Fusion **39**, 2251 (1999).

2. B. N. Breizman and S. E. Sharapov, Plasma Phys. Controlled Fusion **37**, 1057 (1995).

3. J. Candy, B. N. Breizman, J. W. van Dam, *et al.,* Phys. Lett. A **215**, 299 (1996).

4. H. L. Berk, D. N. Borba, B. N. Breizman, *et al.,* Phys. Rev. Lett. **87**, 185002 (2001).

5. B. N. Breizman, H. L. Berk, M. S. Pekker, *et al.,* Phys. Plasmas **10**, 3649 (2003).

6. S. E. Sharapov, A. B. Mikhailovskiĭ, and G. T. A. Huysmans, Phys. Plasmas **11**, 2286 (2004).

7. S. V. Konovalov, A. B. Mikhaĭlovskiĭ, V. S. Tsypin, *et al.*, Dokl. Akad. Nauk **385**, 44 (2002) [Dokl. Phys. **47**, 488 (2002)].

8. S. V. Konovalov, A. B. Mikhailovskiĭ, M. S. Shirokov, *et al.*, Phys. Plasmas **11**, 2303 (2004).

9. A. B. Mikhailovskiĭ, *Instabilities in a Confined Plasma* (Inst. Phys., Bristol, 1998).

Translated by V. Bukhanov

Self-Consistent Description
of Charged-Particle Flux Catastrophes

N. D. Naumov

Presented by Academician A.F. Andreev May 19, 2004

Received April 6, 2004

In a number of analytical models describing the propagation of a charged-particle flux, there exist points at which the particle density takes infinite values. The appearance of a singularity of the particle density at certain instants of time $t = t_k$ can be treated as time catastrophes [1–3]. Thus, the analysis of flux dynamics at times $t \geq t_k$, which is based on the particle density, encounters certain difficulties, especially in the case of a self-consistent problem (see [4]). In the present paper, we propose a new approach to a self-consistent description of one-dimensional motion of a cold charged-particle flux which allows us to avoid the appearance of singularities.

For brevity, we restrict our analysis to the consideration of a plane problem. In this case, describing the motion of a particle flux, we can use instead of the particle density $n(x, t)$ the function $N(x, t)$ characterizing the time dependence of the particle number in a volume of thickness x:

$$N(x, t) = \int_0^x n(x, t)dx.$$

Under the condition of displacement of particle layers without interpenetration, we can obtain from equations corresponding to the Eulerian description of a cold charged-particle gas a self-consistent set of equations for both the function $N(x, t)$ and the gas-dynamic velocity $V(x, t)$:

$$\frac{\partial N}{\partial t} + V\frac{\partial N}{\partial x} = 0, \tag{1}$$

$$\frac{\partial V}{\partial t} + V\frac{\partial V}{\partial x} = \frac{e}{m}\left(E_0 + 4\pi e\left[N(x, t) - \frac{1}{2}N_0\right]\right). \tag{2}$$

Here, e and m are the particle charge and mass, respectively; N_0 is the total number of particles; and E_0 is the external electromagnetic field. We also assume that the origin of coordinates was chosen in such a manner that the flux motion occurs within the domain $0 \leq x \leq L$.

If, at the initial instant of time, the flux characteristics are specified, i.e., $N(x, 0) = M(x)$, $V(x, 0) = U(x)$, then the expressions describing them at an arbitrary

instant of time can be obtained on the basis of the law for Lagrangian-particle motion. In the absence of interpenetration of layers, the collective field acting on a Lagrangian particle with the coordinates $s(t, x_0)$ is determined by its initial position x_0. This makes it possible to write the equation of particle motion as

$$\frac{\partial^2 s}{\partial t^2} = \frac{e}{m}\left(E_0 + 4\pi e\left[M(x_0) - \frac{1}{2}N_0\right]\right). \tag{3}$$

The initial conditions to Eq. (3) have the form

$$s(0, x_0) = x_0, \quad u(0, x_0) = U(x_0).$$

Here, the notation $u(t, x_0) = \dfrac{\partial s}{\partial t}$ is used.

We denote the root of the transcendental equation $s(t, q) = x$ as $q(x, t)$, i.e., $s(t, q(x, t)) \equiv x$. Then, the function $s(t, q(x, t))$ satisfies the following relationships:

$$\frac{\partial s}{\partial q}\frac{\partial q}{\partial x} = 1, \quad u(t, q(x, t)) + \frac{\partial s}{\partial q}\frac{\partial q}{\partial t} = 0.$$

Using these relationships, we can immediately verify that the solutions to Eqs. (1) and (2) have the form

$$N(x, t) = M(q(x, t)), \quad V(x, t) = u(t, q(x, t)). \tag{4}$$

Evidently, expressions (4) can be constructed in the case where $s(t, x_0)$ is a single-valued function of the variable x_0. In order to clarify this question, it is convenient to use the function $R(t, x_0) = \dfrac{\partial s}{\partial x_0}$. If the function R does not vanish with time, then $s(t, x_0)$ is a single-valued function of the variable x_0. If, at a certain instant of time $t = t_k$ at the point $x_0 = x_{0k}$ lying within the region of the gas motion, the condition $R(t_k, x_{0k}) = 0$ is fulfilled, then the function $s(t_k, x_0)$ is a single-valued function of the variable x_0 only in the case that $x_0 = x_{0k}$ is an inflection point of the function $f(x_0) = s(t_k, x_0)$, i.e., when

$Q(t_k, x_{0k}) = 0$ (here, the notation $Q(t, x_0) = \dfrac{\partial R}{\partial x_0}$ is used).

Therefore, under validity of the condition $R(t_k, x_{0k}) = 0$, the expansion of the single-valued function $s(t_k, x_0)$

into a Taylor series in the vicinity of the point $x_0 = x_{0k}$ has the form

$$s(t_k, x_0) \approx s(t_k, x_{0k}) + P(x_0 - x_{0k})^3,$$

where $P = \dfrac{1}{6}\dfrac{\partial Q(t_k, x_0)}{\partial x_0}\bigg|_{x_0 = x_{0k}}$. Assuming $q_k = q(x_k, t_k)$,

$x_k = s(t_k, x_{0k})$, we find

$$q(x, t_k) \approx q_k + P^{-1/3}(x - x_k)^{1/3}.$$

This result allows us to estimate the number of particles in the vicinity of the point $x = x_k$:

$$\Delta N = N(x, t_k) - N(x_k, t_k)$$

$$\approx P^{-1/3}(x - x_k)^{1/3}\frac{dM(q)}{dq}\bigg|_{q = q_k}, \qquad (5)$$

i.e., at the time instant $t = t_k$ and a distance ε from the point $x = x_k$, the mean particle density is $\dfrac{\Delta N}{\varepsilon} \sim \varepsilon^{-2/3}$.
This order of magnitude for the mean density is characteristic of the cuspidal edge [1].

As an illustration, we consider standing waves of electron gas in plasma under the assumption of the steady-state ion distribution. In this case, it is sufficient to study the particle-flux motion in a domain with a thickness equal to the wavelength L. Let the initial electron velocity be zero and the initial distribution of the electron density be of the form

$$n(x, 0) = n_0 v(x), \quad n_0 = \frac{N_0}{L},$$

$$v(x) = 1 - 4\zeta(1 - 2|\zeta|).$$

The plot of the function $v(x) - \dfrac{1}{2}$ is shown in the figure (curve 4).

Allowing for $E_0 = -4\pi e n_0\left(x - \dfrac{L}{2}\right)$, we find from Eq. (3) the following expression for the law of motion of a Lagrangian particle:
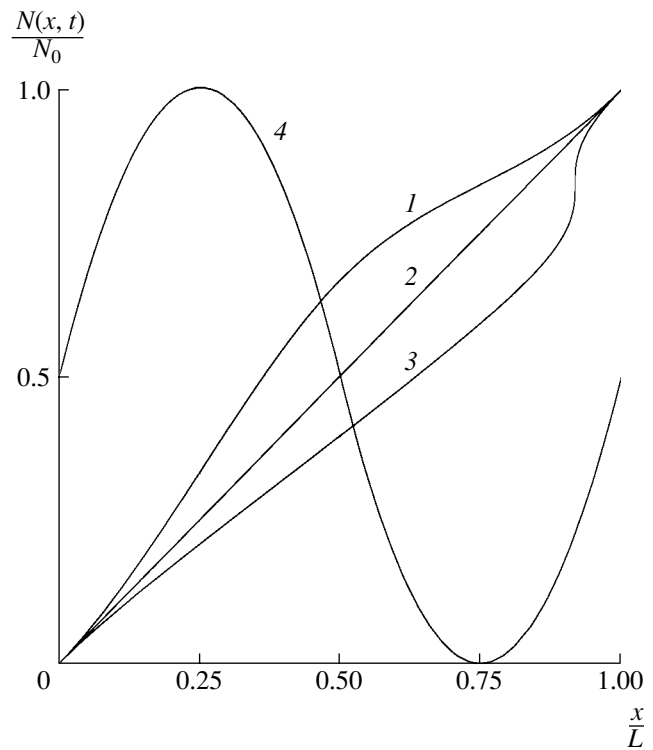
$$s(t, x_0) = L\left[\eta + \frac{4}{3}(4\eta^3 - 9\eta^2 + 6\eta - 1)\sin^2\tau\right]. \quad (6)$$

Hereinafter, the notation

$$\zeta = \xi - \frac{1}{2}, \quad \xi = \frac{x}{L}, \quad \eta = \frac{x_0}{L}, \quad \tau = \frac{\omega t}{2},$$

$$\omega^2 = \frac{4\pi n_0 e^2}{m}$$

is used.

$$\frac{N(x, t)}{N_0}$$

Particle number distribution for $\sin\dfrac{\omega t}{2} = 0$, 0.5, and 1 (curves 1, 2, and 3, respectively); curve 4 corresponds to the function $v(x) - \dfrac{1}{2}$.

The function $R(t, x_0) = 1 + 8(2\eta^2 - 3\eta + 1)\sin^2\tau$ vanishes for $\eta_k = \dfrac{3}{4}$, $t_k = \dfrac{(2l + 1)\pi}{\omega}$, $l = 0, 1, 2, \ldots$. The point $x_{0k} = \dfrac{3L}{4}$ is an inflection point since $Q(t_k, x_0) = \dfrac{8(4\eta - 3)}{L}$ vanishes at this point. A catastrophe of the flux occurs at the point $x_k = s\left(t_k, \dfrac{3L}{4}\right) = \dfrac{11L}{12}$. Using formula (5) for the number of particles in the vicinity of this point, we arrive at

$$\Delta N \approx \frac{1}{4}N_0 \sqrt[3]{\frac{3}{2}\xi - \frac{11}{8}}. \qquad (7)$$

We now compare the estimate obtained with the exact solution of the problem. From the equation $s(t_k, q) = x$, where $s(t, x_0)$ is determined by expression (6), we find

$$\frac{1}{L}q(x, t_k) = \frac{3}{4} + \sqrt[3]{\frac{3}{2}\xi - \frac{11}{8}}.$$

Taking into account expression (4) for the function $N(x, t_k)$, we can write

$$N(x, t_k) = N_0\left(\frac{3}{8} + \frac{1}{2}\xi + \frac{1}{4}\sqrt[3]{\frac{3}{2}\xi - \frac{11}{8}}\right), \quad \frac{5}{6}L \le x \le L.$$

Hence, it follows that

$$N(x, t_k) - N\left(\frac{11}{12}L, t_k\right)$$

$$= N_0\left[\frac{1}{2}\left(\xi - \frac{11}{12}\right) + \frac{1}{4}\sqrt[3]{\frac{3}{2}\xi - \frac{11}{8}}\right],$$

i.e. in the vicinity of the point $x_k = \frac{11L}{12}$, estimate (7) differs negligibly from the exact result. The coordinate dependences of the function $N(x, t)$ for $\sin\tau = 0, 05,$ and 1 (curves *1*, *2*, and *3*, respectively) are plotted in the figure.

A situation is possible that the condition $Q(t_k, x_{0k}) = 0$ becomes unnecessary, e.g., if the point $x_0 = x_{0k}$ corresponds to the boundary of the flux motion domain. Assuming for definiteness that the time catastrophe occurs at the left boundary of this domain, we can in a similar manner obtain the following estimate for the particle number in the vicinity of the flux boundary $x = x_k$:

$$\Delta N \approx \sqrt{\frac{2}{Q_k}(x - x_k)}\frac{dM(q)}{dq}\bigg|_{q = q_k}, \qquad (8)$$

where Q_k is the value of the right derivative of the function $R(t_k, x_0)$ at the point $x_0 = x_{0k}$. Here, at a distance ε from the flux boundary, the mean particle density is proportional to $\sim\varepsilon^{-1/2}$, i.e., the boundary point is a fold point [1].

For example, let the initial electron density be specified as a piecewise linear function: $\nu(x) = \frac{3}{2} - 2|\zeta|$. In this case, it is evident that the motion of the electron flux should be symmetric with respect to the plane $x = \frac{L}{2}$. Therefore, we may restrict our analysis to the consideration of the domain $0 \le x \le \frac{L}{2}$:

$$s(t, x_0) = L\eta[1 + (2\eta - 1)\sin^2\tau],$$

$$R(t, x_0) = 1 + (4\eta - 1)\sin^2\tau.$$

From this, it follows that catastrophes of the flux occur at the domain boundaries and at the same instants of time as in the previous example. Since $Q_k = \frac{4}{L}$, formula (8) is applicable for estimating the number of particles: $\Delta N = \frac{N_0}{2}\sqrt{\frac{\xi}{2}}$. For comparison, we present the expression for the function

$$N(x, t_k) = \frac{1}{2}N_0\left(\xi + \sqrt{\frac{\xi}{2}}\right), \quad 0 \le x \le \frac{L}{2}.$$

In conclusion, we should note that the approach proposed for describing the one-dimensional gas motion also does not lead to singularities in the case of spatial catastrophes (focusing) of a charged-particle flux. For example, if the initial flux characteristics have the form

$$\nu(x) = \left(\frac{3}{2} - 2|\zeta|\right)H(1 - 2|\zeta|),$$

$$U(x) = -\omega\zeta\sqrt{3 - 2|\zeta|}\,H(1 - 2|\zeta|),$$

then in the absence of an external field, we find for $0 \le x_0 \le \frac{L}{2}$:

$$\frac{1}{L}s(t, x_0) = \frac{1}{2} + \left(\eta - \frac{1}{2}\right)(1 - \tau\sqrt{2(1 + \eta)})^2, \qquad (9)$$

$$R(t, x_0) = 2\left(\tau - \frac{1}{\sqrt{2(1 + \eta)}}\right)$$

$$\times\left[\tau\left(2\eta + \frac{1}{2}\right) - \frac{1 + \eta}{\sqrt{2(1 + \eta)}}\right]. \qquad (10)$$

Here, $H(x)$ is the Heaviside step function. As in the previous example, the flux motion is symmetric with respect to the plane $x = \frac{L}{2}$.

As is seen from expression (10), under the validity of the condition $\tau = \frac{1}{\sqrt{2(1 + \eta)}}$, the function R is zero; in this case, $x_k = \frac{L}{2}$. For the first time, this function vanishes at $x_{0k} = \frac{L}{2}$, $t = t_1 = \frac{2}{\omega\sqrt{3}}$. Then, in the domain $x \le \frac{L}{2}$,

$$N(x, t_1) = N_0\left(\frac{1}{2} - \frac{3}{2}\chi + \chi^2\right)H(1 - 2|\chi|),$$

$$\chi = \frac{3}{4}\sqrt{\frac{1}{\varphi}(1 - 2\xi)} + \sqrt{\frac{3}{2}\sqrt{\varphi(1 - 2\xi)} - \varphi^2},$$

$$\varphi = \frac{1}{2}(\sqrt[3]{1 + \sigma} + \sqrt[3]{1 - \sigma})_3\sqrt{\frac{9}{4}(1 - 2\xi)},$$

$$\sigma = \sqrt{1 - \frac{16}{81}(1 - 2\xi)}.$$

Thus, it follows from expressions (9) and (10) that, during the time period from t_1 to $t_2 = \dfrac{\sqrt{2}}{\omega}$, time catastrophes permanently occur at the flux center. At the time instant $t = t_2$, the spatial catastrophe of the flux arises,

$N(x, t_2) = N_0H\left(\xi - \dfrac{1}{2}\right)$, i.e., all particles turn out to be in the plane $x = \dfrac{L}{2}$.

REFERENCES

1. V. I. Arnol'd, *Catastrophe Theory* (Nauka, Moscow, 1990).
2. A. A. Samarskiĭ and A. P. Mikhaĭlov, *Mathematical Simulation* (Fizmatlit, Moscow, 1997).
3. V. P. Bykov, A. V. Gerasimov, and V. O. Turin, Usp. Fiz. Nauk **165**, 955 (1995).
4. N. D. Naumov, Dokl. Akad. Nauk **392**, 467 (2003) [Dokl. Phys. **48**, 537 (2003)].
5. R. C. Davidson, *Theory of Nonneutral Plasma* (W.A. Benjamin, Inc., 1974; Mir, Moscow, 1978).

Translated by G. Merzon

=========================== **PHYSICS** ===========================

Optical-Radiation Power Limiting in High-Scattering Media

S. A. Tereshchenko and V. M. Podgaetskiĭ

Presented by Academician F.V. Bunkin March 3, 2004

Received April 5, 2004

INTRODUCTION

Great current interest in investigating limiters of the energy and power of dangerous laser radiation is associated with the enhancing intensity of optical range finders and target designators operating in the visible and IR spectral ranges. The action of ecological laser lidars also presents a certain hazard. Modern devices of such and similar types, even after achievement of the international agreement on the prohibition of blinding laser weapons [1], can cause permanent blindness of people and destroy sensitive elements in optical-radiation sensors. By virtue of these reasons, the problem of the development of optical-radiation power limiters with a response time much shorter than a laser radiation pulse time was considered in a number of international conferences [2, 3]. Recently, this problem has attracted much attention in Russia as well [4].

In designing experimental prototypes of optical-radiation limiters, efforts were made to use various physical phenomena, such as the induced nonlinear radiation absorption by dye molecules, thermal defocusing of laser radiation in liquids and gases, two-photon light absorption in organic dyes, light scattering and the Kerr effect in liquid crystals, nonlinear absorption and light-induced refraction in semiconductors, radiation absorption in plasma of a laser-induced breakdown in the case of multiphoton ionization in the strong electromagnetic field of a light wave, self-focusing and self-defocusing effects of laser radiation in polar liquids, and intermolecular complexing via the Förster mechanism. The use of darkening organic dyes turned out to be most promising. Investigation of the nonlinear optical properties of such organic molecules is of special interest not only in connection with their use for optical-radiation limiters but also with the possibility of their application in other optical technologies [5].

The basic approach to the theoretical description of optical power limiting is reduced to the following procedure [6, 7]. A certain hypothetical physical mechanism (effect) underlying optical-radiation power limiting on the microscopic level is considered. Parameters of this effect, which make it possible to find the macroscopic characteristics of the limiter material, such as absorption and scattering coefficients entering into the radiation-transfer equation, are given or calculated. Using this equation, the transmission of the laser radiation through the limiter is calculated, and the dependence of the output-radiation intensity on the intensity of input radiation (output characteristic) is determined. Finally, at the last stage, the dependence obtained is compared with that observed experimentally, and the conclusion is drawn on the correspondence between the theoretical description and the experimental data. It should be noted that known attempts to apply such an approach indicate the clear disagreement between the theory and experiment. One can list at once certain reasons leading to this result. First, as a rule, in an actual limiter, several mechanisms responsible for the interaction of radiation with a medium act simultaneously, and their relative contribution being known insufficiently. Second, the description of each of the mechanisms is based on a large number of numerical parameters whose values can differ from those of an actual limiter. Third, the calculation of macroscopic characteristics is a complicated problem which still remains not exhaustively solved. Assumptions used in these calculations can result in significant differences compared to the parameters of an actual limiter. Fourth, numerical simulation of the radiation-transfer equation is not a simple task, since in solving this problem, we have to additionally use various approximations, which can also lead to discrepancies. Thus, although such an approach can be useful in searching for new limiter materials, it is of little use in describing the properties of actual limiters.

We can propose another approach, in a certain sense, inverse to the method described above. As initial data, we consider the experimental characteristics of a particular limiter. Then, it is possible to set the problem of determining (directly from experimental data) the dependence of the optical characteristics of the limiter material (e.g., absorption coefficient) on either the intensity of continuous radiation or the pulse energy in the case of pulsed radiation. The solution to this problem makes it possible to predict properties of limiters for various values of their thickness, as well as to compare limiters of various types with each other. In addi-

Moscow Institute of Electronic Technology
(Technical University), Zelenograd,
Moscow, 103498 Russia

tion, this solution allows us to investigate at the microscopic level the contribution of different mechanisms responsible for the optical-radiation power limiting.

In the problem of optical-radiation power limiting by a limiter, the radiation-transfer equation for the continuous radiation can be written in the form

$$\mathbf{\Omega}\,\mathrm{grad}\,I(\mathbf{r}, \mathbf{\Omega}) + \mu(I)I(\mathbf{r}, \mathbf{\Omega})$$

$$-\oint_{4\pi} I(\mathbf{r}, \mathbf{\Omega}')\mu_s(I, \mathbf{\Omega}' \to \mathbf{\Omega})d\mathbf{\Omega}' = S(\mathbf{r}, \mathbf{\Omega}), \qquad (1)$$

where $I(\mathbf{r}, \mathbf{\Omega})$ is the intensity of radiation at the point $\mathbf{r} = (x, y, z)$, which propagates in the direction $\mathbf{\Omega}$; $\mu_s(I, \mathbf{\Omega}' \longrightarrow \mathbf{\Omega})$ is the differential (with respect to angles) radiation scattering coefficient (scattering indicatrix) depending on the radiation intensity; $\mu_a(I)$ is the radiation absorption coefficient also depending on the radiation intensity; $S(\mathbf{r}, \mathbf{\Omega})$ is the distribution function of radiation sources; and $\mu(I)$ is the attenuation (extinction) coefficient

$$\mu(I) = \mu_a(I) + \oint_{4\pi}\mu_s(I, \mathbf{\Omega} \to \mathbf{\Omega}')d\mathbf{\Omega}'. \qquad (2)$$

For the pulsed radiation, we imply as $I(\mathbf{r}, \mathbf{\Omega})$ the total energy of a pulse. However, in this case, the characteristics of the medium additionally depend on the pulse duration τ: $\mu_a = \mu_a(I, \tau)$; $\mu_s = \mu_s(I, \mathbf{\Omega}' \longrightarrow \mathbf{\Omega}, \tau)$, and $\mu = \mu(I, \tau)$.

LIMITING OF THE RADIATION INTENSITY IN A PURELY ABSORBING MEDIUM

We consider a limiter representing a layer of thickness d and made of a homogeneous purely absorbing material for which $\mu_s(I, \mathbf{\Omega}' \longrightarrow \mathbf{\Omega}) = 0$. The source is assumed to be point and unidirectional, i.e., $S(\mathbf{r}, \mathbf{\Omega}) = U_0\delta(x)\delta(y)\delta(z)\delta_2(\mathbf{\Omega}\mathbf{\Omega}_0)$, where z is the coordinate perpendicular to the limiter layer, $\delta(\bullet)$ is the one-dimensional Dirac delta-function, $\delta_2(\bullet)$ is the surface delta-function, and $\mathbf{\Omega}_0$ is the direction along the laser beam, which coincides with the z axis. Then, we can write

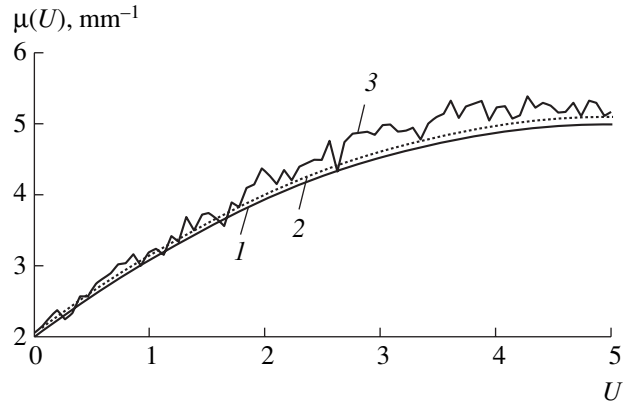$$I(\mathbf{r}, \mathbf{\Omega}) = U(z)\delta(x)\delta(y)\delta_2(\mathbf{\Omega}\mathbf{\Omega}_0)$$

and Eq. (1) takes the form

$$U'(z) + \mu_a(U)U(z) = U_0\delta(z). \qquad (3)$$

The output radiation $U(d)$ is a nonlinear function of the input radiation U_0. To find this dependence, we denote $U(d) = \varphi(U_0)$ and write the solution to Eq. (3) in the form

$$\int_{U_0}^{\varphi(U_0)} \frac{dU}{\mu_a(U)U} = -d. \qquad (4)$$

In implicit form, Eq. (4) determines the output characteristic $\varphi(U_0)$ provided that the dependence of the

Fig. 1. Reconstruction of the absorption coefficient depending nonlinearly on the radiation intensity: (*1*) given absorption coefficient, (*2*) reconstructed absorption coefficient in the absence of noise, and (*3*) reconstructed absorption coefficient in the case of imposing onto the output characteristics of the 3% additive noise.

absorption coefficient on radiation intensity $\mu_a(U)$ and the limiter thickness d are known. For example, for a linear dependence of the absorption coefficient on the radiation intensity $\mu_a(U) = \alpha_a + \beta_a U$, we have the well-known expression for the output characteristic

$$\varphi(U_0) = \frac{U_0\alpha_a e^{-\alpha_a d}}{\alpha_a + \beta_a U_0(1 - e^{-\alpha_a d})}. \qquad (5)$$

If the output characteristic is known, then, differentiating Eq. (4) with respect to U_0, we obtain the functional equation for determining an arbitrary dependence of the absorption coefficient on the radiation intensity $\mu_a(U)$:

$$\varphi'(U)\mu_a(U)U - \varphi(U)\mu_a(\varphi(U)) = 0. \qquad (6)$$

In this case, the value of $\mu_a(0)$ can be found from the initial segment of the output characteristic as $U \longrightarrow 0$ (under the assumption that the Bouguer–Lambert–Beer law is valid).

The obtained dependence of the absorption coefficient on the radiation intensity $\mu_a(U)$ can be used above all to calculate the output characteristic $U(d) = \varphi(U_0)$ for other values of the limiter thickness d.

To solve Eq. (6) numerically, we developed an algorithm that made it possible to reconstruct from the known output characteristic an arbitrary dependence of the absorption coefficient on the radiation intensity. An example of such a reconstruction is shown in Fig. 1 for a significantly nonlinear dependence of the absorption coefficient on the radiation intensity. A small shift of the reconstructed absorption coefficient in the absence of noise results from the inaccuracy in calculating the absorption coefficient for the low radiation intensity. This shift appears as far as the Bouguer–Lambert–Beer law is fulfilled, in the general case, only approximately.

We note that solving Eq. (6) corresponds to an ill-posed problem, which makes it necessary to use the regularization methods, especially in the case of processing actual data possessing statistical errors. The results of numerical simulation in the presence of noise are also shown in Fig. 1. As could be expected, the distortions (because of the ill-posed formulation of the problem) are rather significant even for a low noise level.

LIMITING OF THE RADIATION INTENSITY IN A HIGH-SCATTERING MEDIUM

Application of the above method for the output characteristics of limiters made of the same material but with a different thickness can answer the question of whether the limiter material is a purely absorbing medium. For a purely absorbing medium, the dependences of the reconstructed absorption coefficient on the radiation intensity for any limiter thickness must be the same. The absence of such a coincidence implies that it is necessary to take into account not only radiation absorption but also radiation scattering. However, in the general case, the problem of determining charac-teristics of a limiter material with allowance for its scattering properties is rather difficult. For approximate description of limiting the laser radiation intensity in a scattering medium, we can apply the stationary case of the non-stationary axial (two-flux) model of radiation transfer [8]. Then, instead of Eq. (3), we can write the following equation:

$$U''(z) + [\mu^2(U) - \mu_s^2(U)]U(z) = 0, \qquad (7)$$

where $\mu = \mu_a + \mu_s$ is the extinction coefficient, μ_a is the absorption coefficient, and μ_s is the scattering coefficient. In addition, the boundary conditions

$$U(0) = U_0,$$
$$\frac{d}{dz}U(z)\bigg|_{z=d} + \mu(U(d))U(d) = 0 \qquad (8)$$

must be fulfilled.

Denoting, as before, $U(d) = \varphi(U_0)$, we can write in quadratures the solution to Eq. (7) with allowance for boundary conditions (8) at the point $z = d$:

$$\int_{U_0}^{\varphi(U_0)} \frac{dU}{\sqrt{\mu^2(\varphi(U_0))\varphi^2(U_0) - 2\int_U^{\varphi(U_0)} [\mu^2(E) - \mu_s^2(E)]E\,dE}} = -d. \qquad (9)$$

As in the case of a purely absorbing limiter material, Eq. (9) in implicit form defines the output characteristic $\varphi(U_0)$ for a given thickness d of a limiter and the known dependence of both the extinction coefficient $\mu(U)$ and the scattering coefficient $\mu_s(U)$ on the radiation intensity. For example, for the linear dependences $\mu(U) = \alpha + \beta U$ and $\mu_s(U) = \alpha_s + \beta_s U$ (note that, in this case, $\mu_a(U) = \alpha_a + \beta_a U = \alpha - \alpha_s + (\beta - \beta_s)U)$, we find

$$\int_{\varphi(U_0)}^{U_0} \frac{dE}{\sqrt{A - \varepsilon_1[\varphi^2(U_0) - E^2] - \frac{4}{3}\varepsilon_2[\varphi^3(U_0) - E^3] - \frac{1}{2}\varepsilon_3[\varphi^4((U_0) - E^4)]}} = d, \qquad (10)$$

where $\varepsilon_1 = \alpha^2 - \alpha_s^2$, $\varepsilon_2 = \alpha\beta - \alpha_s\beta_s$, $\varepsilon_3 = \beta^2 - \beta_s^2$, and $A = [\alpha + \beta\varphi(U_0)]^2\varphi^2(U_0)$.

Expression (10) can be used to calculate the output characteristics $U = \varphi(U_0)$ for the given d, α, β, α_s, and β_s. It is of interest to compare the output characteristics extracted from expression (5) and from Eq. (10) in the absence of scattering ($\mu_s(U) = 0$). In this case, $\mu(U) = \mu_a(U) = \alpha + \beta U$. Ideally, these characteristics must coincide, but due to the approximate form of Eq. (7), a certain difference must be expected. Figure 2 shows plots of the output characteristics for different values of the parameter $b = \alpha d$. As a whole, the coincidence of the models for this case is rather good, which makes it possible to use general expression (9) also in the presence of scattering. The effect of scattering on the output characteristics, which was calculated with the help of Eq. (10), is illustrated in Fig. 3.

In contrast to the case of a purely absorbing limiter material for the given value d and the output characteristic $\varphi(U_0)$, it is necessary to find two unknown functions $\mu = \mu(U)$ and $\mu_s = \mu_s(U)$, which is impossible without additional assumptions. Such an assumption can be, for example, setting one of the coefficients (of either
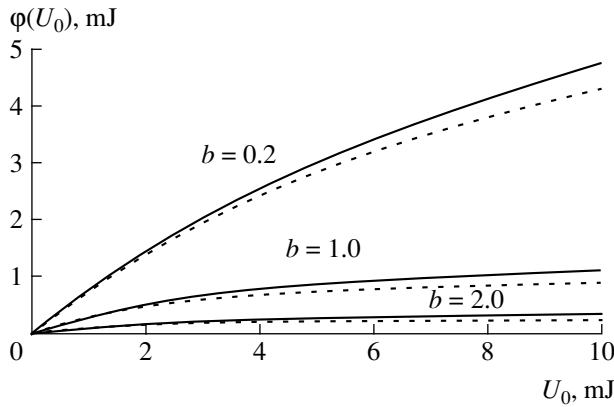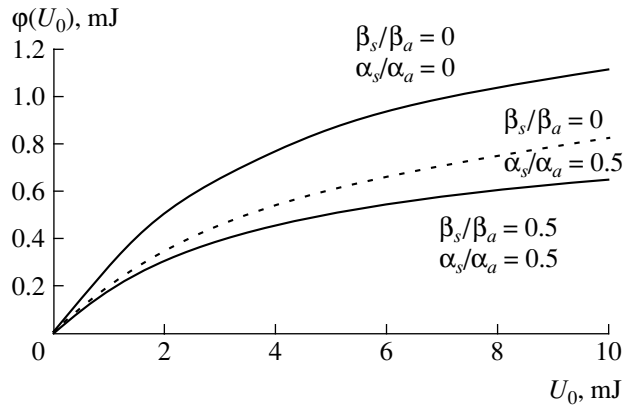
Fig. 2. Output characteristics calculated according to Eq. (4) (dotted curves) and to Eq. (9) in the absence of scattering (solid curves) for various values of the parameters $b = \alpha d$ ($\alpha = 2$ cm^{-1} and $\beta = 1$ cm^{-1} mJ^{-1}).

Fig. 3. Output characteristics calculated according to Eq. (10) for various values of parameters ($\alpha_a = 2$ cm^{-1} and $\beta_a = 1$ cm^{-1} mJ^{-1}).

absorption or scattering) independently as a function of radiation intensity (in particular, as a constant). Another method is setting a relation between the functions $\mu(U)$ and $\mu_s(U)$. One such relation can be the proportionality $\mu_s(U) = \gamma\mu(U)$, where γ is constant. Next, in order to find the remaining function, it is possible to use Eq. (9).

Thus, in this study, we proposed an approach for describing optical-radiation power limiting. This approach makes it possible to consider the problem independently of particular microscopic mechanisms of the interaction of radiation and a medium. A relation between the optical characteristics of a limiter material and the output characteristic of a radiation limiter (namely, the dependence of the transferred-radiation intensity on the intensity of the incident radiation) was examined. In the case that only the radiation absorption is taken into account, the exact solutions for determining both the output characteristic from the known dependence of the absorption coefficient on the radiation intensity and the dependence of the absorption coefficient on the radiation intensity, which was extracted from the experimental output characteristic, are presented. In the case that the scattering process was additionally taken into account, similar approximate equations were obtained. The extraction of optical characteristics of a limiter material directly from the experimental output characteristic provides a possibility to predict properties of the limiter material for other values of its thickness, as well as an efficient comparison between limiters of different types.

REFERENCES

1. *Protocol IV on 5.10.95 of the Conference of States Participating in the Convention on Prohibition or Limiting of the Use of Certain Conventional Weapons Capable of Being Excessively Injurious or Having Indiscriminate Effects*, Vienna, 1995.
2. *Proceedings of I Int. Conf. on Optical-Power Limiting, Cannes, 1999*; Nonlinear Opt., Nos. 1–6 (1999).
3. *Proceedings of the SPIE Conf. on Power-Limiting Materials and Devices, Denver, 1999*; Proc. SPIE **3798** (1999).
4. *Proceedings of the 10th Int. Conf. on Laser Techniques, St. Petersburg, 2001*; Proc. SPIE **4353** (2001).
5. L. Tutt and T. Bogges, Prog. Quantum Electron. **17**, 299 (1993).
6. I. M. Belousova, V. A. Grigor'ev, O. B. Danilov, *et al.*, Opt. Spektrosk. **90**, 341 (2001) [Opt. Spectrosc. **90**, 292 (2001)].
7. I. M. Belousova, N. G. Mironova, and M. S. Yur'ev, Opt. Spektrosk. **91**, 874 (2001) [Opt. Spectrosc. **91**, 820 (2001)].
8. S. V. Selishchev and S. A. Tereshchenko, Zh. Tekh. Fiz. **67** (5), 61 (1997) [Tech. Phys. **42**, 511 (1997)].

Translated by Yu. Vishnyakov

===== **PHYSICS** =====

An Effect of Defects in Nonmetallic Sublattice
on Properties of Titanium Carbide

Academician A. V. Elyutin, A. V. Manukhin, G. A. Kupreeva, and P. B. Lopatin

Investigating processes of structure formation of nonstoichiometric compounds in which order–disorder phase transitions are possible is of importance for both theory and practice of the development of new materials.

Effects of ordering render a substantial influence on the physicomechanical and operational properties of nonstoichiometric compounds. Studying an effect of a high external pressure on materials also is of particular interest because new modifications of substances with specific properties unusual for those obtained by conventional methods can be thus formed. Nowadays, investigations devoted to phase transitions of elements and compounds under high pressure are carried out. In this field of science, rather interesting data were obtained; however, in the literature, there is virtually no information concerning nonstoichiometric compounds of the interstitial-phase type.

The goal of this study is to investigate an effect of high pressure and temperature on the structure and properties of titanium carbide with a varying content of carbon in the nonmetallic sublattice. To do this, we analyzed nonstoichiometric titanium carbides with compositions of $0.76 \leq C/Ti \leq 0.87$ obtained at high temperatures and pressures. The composition region $0.75 \leq C/Ti \leq 0.90$ is the least investigated, because the methods of structural analysis existing nowadays do not show here satisfactory results, whereas according to theoretical calculations, an ordered superstructure should exist in this region [1–3].

For preparing nonstoichiometric titanium carbides, we used powders of titanium carbide with a mass fraction of common carbon of 18.25% and free carbon of 1.20%, as well as of metallic titanium and carbon black.

Powder-like components were mixed in an agate mortar (1.5 h) and in a mill of the "drunk-barrel" type (20–30 min). After mixing, the charge was pressed by a DO137A high-pressure press in toroidal working cells (10 mm in height and 9.4 mm in aperture diameter)

made of a sharpened lithographic stone. The heating was performed by an electric current flowing through both the working chamber and the working cell. Preliminarily, the high-pressure press and the working cell were pressure calibrated using a reference metal with the B1-type lattice and temperature calibrated using chromel–alumel, platinum–rhodium, and tungsten–rhenium thermocouples up to temperatures of 1200, 1500, and 2000°C, respectively.

The samples were prepared at a pressure of about 80 kbar and a temperature of about 1850–1950°C. After the desired pressure was obtained, the time of heating the working chamber with the working cell attained 1.5 min, and the exposure time was 3 min. After the exposure was terminated, the heating was stopped for 2–3 s (the current was reduced to zero, and the circuit was turned off). Then, the pressure was made to drop for 2–3 s, after which the working cell with a sample was naturally self-cooled down to a normal temperature in the working chamber.

After pressing, all the samples were extracted from the cells and trimmed by a diamond disk on a 3B70V machine tool.

Afterwards, we determined the density of the samples by hydrostatic weighing on a VLA-200-M balance. The grain size was measured with an MIM-8 microscope using the grid eyepiece with a 900× magnification. All the measurements were carried out for sample surface layers (the bottom sample base) to exclude an effect of a possible nonuniform (in height) structure of the samples obtained.

The phase composition and lattice spacing were determined for samples with polished metallographic sections according to diffraction patterns obtained on a DRON-3M X-ray diffractometer equipped with a scintillation counter. Recording reflections and their intensities with a KSP-4 potentiometer was also performed.

Chemical compounds were identified on the basis of the card file of the A.S.T.M. diffraction passport tables.

We measured the microhardness of the samples with a PMT-3 device and the specific electrical resistance with a Hall-0 precision calibrating setup using the four-probe method.

Moscow Institute of Steel and Alloys
(Technological University), Leninskiĭ pr. 4,
Moscow, 117936 Russia
e-mail: gkupreeva@omk.ru

The mass fraction of common and free carbon in the samples prepared was determined in laboratory 13 of the VNIITS (Moscow). The oxygen and nitrogen contents in the samples were measured with Leco automatic analyzers (France). The obtained titanium carbide samples were pellet-shaped (about 5–6 mm in diameter and 2–4 mm in height). We synthesized six nonstoichiometric compositions of titanium carbide. The samples were certified by metallographic, X-ray, and chemical analyses. The results of the investigations are shown in the table. The data obtained were used for plotting piecewise broken concentration dependences for both the lattice spacing and the microhardness (Fig. 1). All are of a nonlinear character.

An explanation for the obtained dependences of properties of nonstoichiometric titanium carbide with compositions within the region $0.76 < C/Ti < 0.87$, which was synthesized by us at high temperatures and pressures, can be given on the basis of a multistructural-composition model. From the analysis of the composition–property–ordering interrelation in carbides and nitrides of transition metals related to the IVa and Va subgroups and on the basis of the conclusions made in [1–9], it is apparently possible to speak of the complicated structurally nonuniform composition of these compounds, which is caused by multiple order–disorder transitions in the homogeneity region.

As is seen in Fig. 1, the composition–property plots exhibit breaks and extrema corresponding to the existence region of a new suggested ordered structure of titanium carbide with the $C/Ti \approx 0.8$ composition. It is well-known that hardening takes place in nonstoichiometric titanium carbide when its composition approaches the superstructure. This occurs due to the increasing fraction of ordered regions corresponding to a certain superstructure. If a combination of ordered structures exists near $TiC_{0.8}$, where the TiC-type region attains about 80% with respect to Ti_2C, then this combination can provide a more stable lattice of titanium carbide and, correspondingly, higher values of the microhardness at the point of the suggested superstructure, i.e., of $TiC_{0.8}$ (Fig. 1b). At the same time, the high-
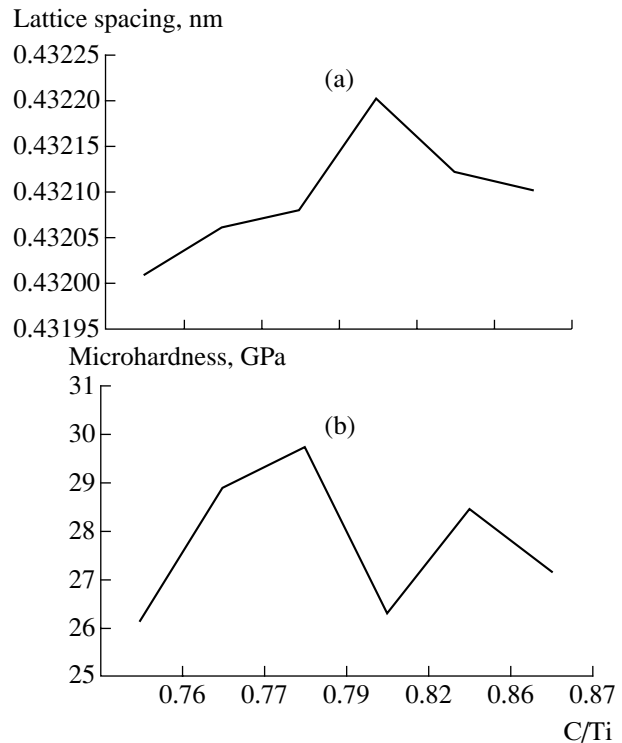
Fig. 1. Properties of titanium carbide of different nonstoichiometric compositions as a function of the concentration: (a) lattice spacing; (b) microhardness.

est microhardness index does not correspond in this case to the point $C/Ti \approx 0.8$ of the superstructure; the concentration dependence tends to a minimum from $TiC_{0.79}$ to $TiC_{0.82}$; and the minimum value of microhardness lies correspondingly in the region of the maximum value of the lattice spacing. Such a behavior of the microhardness is quite natural because the larger the lattice spacing, the lower the density and the smaller the microhardness, which is seen from the obtained dependences.

Thus, the analysis performed of plotted concentration curves for both the lattice spacing and the micro-

Characteristics of obtained titanium carbide samples

TiC_{bond}	Mass fraction, %			Preparation method
	C_{free}	O	N	
$TiC_{0.76}$	1.09	3.10	0.26	From the mixture of initial carbide powder with Ti_{metal} powder
$TiC_{0.77}$	0.94	3.00	0.30	"
$TiC_{0.79}$	0.80	3.11	0.27	"
$TiC_{0.82}$	2.52	3.30	0.28	From the mixture of initial carbide powder with carbon black
$TiC_{0.86}$	0.90	3.23	0.26	Pressing of initial carbide powder
$TiC_{0.87}$	1.56	3.32	0.31	From the mixtures of initial carbide powder with carbon black

Note: The average grain size is 8–10 μm (there are coarse grains of 18–20 μm); the sample porosity is 2%.

hardness of different-composition titanium carbides synthesized by us at high pressures and temperatures makes it possible to establish a nonlinear change in properties of this compound in the composition region of $0.76 < x < 0.87$. Nonadditive variation in the properties of obtained titanium carbide we explain on the basis of the model of its multistructural composition in the homogeneity region, which is caused by the existence of phase transitions. Based on the analysis of both experimental data and data on the ordering of nonstoichiometric compounds presented in the literature, we have shown that, irrespective of the method of titanium carbide preparation, the phase transitions are conserved for certain compositions and, thus, the properties acquired by a material as a result of these phase transitions are also conserved.

ACKNOWLEDGMENTS

REFERENCES

1. A. I. Gusev and A. A. Rempel', Dokl. Akad. Nauk **332**, 717 (1993).
2. A. V. Elyutin, A. V. Manukhin, and P. B. Lopatin, Dokl. Akad. Nauk **340**, 198 (1995).
3. A. V. Elyutin, A. V. Manukhin, and P. B. Lopatin, Dokl. Akad. Nauk **356**, 489 (1997).
4. A. V. Manukhin and P. B. Lopatin, Izv. Vyssh. Uchebn. Zaved., Chern. Metall., No. 5, 63 (1994).
5. A. V. Manukhin and P. B. Lopatin, Izv. Vyssh. Uchebn. Zaved., Chern. Metall., No. 7, 46 (1994).
6. A. V. Manukhin and P. B. Lopatin, Izv. Vyssh. Uchebn. Zaved., Chern. Metall., No. 9, 49 (1994).
7. A. V. Manukhin and P. B. Lopatin, Izv. Vyssh. Uchebn. Zaved., Chern. Metall., No. 5, 37 (1995).
8. A. V. Manukhin and P. B. Lopatin, Izv. Vyssh. Uchebn. Zaved., Chern. Metall., No. 7, 35 (1995).
9. E. Parthe and K. Yvon, Acta Crystallogr. B: Struct. Sci. **26**, 153 (1970).
10. A. I. Gusev, *Physical Chemistry of Refractory Nonstoichiometric Compounds* (Nauka, Moscow, 1991).
11. A. I. Gusev and A. A. Rempel', *Structure Phase Transitions in Nonstoichiometric Compounds* (Nauka, Moscow, 1988).

Translated by V. Bukhanov

TECHNICAL PHYSICS

The Use of Severe Deformations for Preparing Bulk Nanocrystalline Materials from Amorphous Alloys

R. Z. Valiev*, V. G. Pushin**, D. V. Gunderov*, and A. G. Popov**

Presented by Academician Yu.K. Kovneristyĭ January 12, 2004

Received March 12, 2004

In the last decade, a new scientific trend associated with developing and investigating bulk nanocrystalline (NC) materials with unique properties has formed and evolved in physical material science [1, 2]. One of the well-known methods of manufacturing NC materials is crystallization of amorphous alloys prepared by fast cooling of melts [3]. However, such amorphous alloys are usually produced in the form of fine powders and ribbons. To transform them into bulk materials, they need subsequent consolidation. In addition, attempts to obtain a homogeneous NC structure by annealing rapidly quenched amorphous alloys failed in most cases [4]. This is also true in the case of bulk amorphous alloys, for which the possibility of production was recently shown for certain metallic systems.

In recent years, methods of severe plastic deformation (SPD), which were proposed for the first time by Russian scientists with the goal of producing ultrafine-grained (UFG) materials [5, 6], have attracted great attention. The SPD methods include creating severe strains in materials under a high pressure applied at relatively low temperatures (usually not exceeding $0.4T_{melt}$) and are aimed at preparing bulk UFG samples without micropores and extraneous impurities [5, 6]. It should also be noted that the use of SPD allows rapidly quenched powders and ribbons to be consolidated into bulk samples at room temperature [6]. Recent investigations also showed [7] that SPD changes the crystallization kinetics of rapidly quenched amorphous alloys under subsequent annealing. This enables us to expect that, using SPD, it is possible to form a homogeneous NC structure by the crystallization of various amorphous alloys, which is impossible to obtain by only annealing. Thus, the severe plastic deformation of amorphous alloys could become a new method for production of bulk NC materials with unique properties.

In the present study, these new conveniences of SPD are shown for a Ti–Ni–Cu alloy possessing the shape-memory effect and for a Nd–Fe–B alloy, which is a hard magnetic material.

In the amorphous state, the $Ti_{50}Ni_{25}Cu_{25}$ and $Nd_{11.8}Fe_{82.3}B_{5.9}$ ($Nd_2Fe_{14}B$) alloys were prepared by rapidly quenching the corresponding melt on a rotating wheel at a cooling rate of 10^6 K/s. Thin flakes of rapidly quenched alloys (RQAs) were subjected to SPD by torsion at room temperature under pressure of 6 GPa and to six revolutions of anvils, which corresponded to a logarithmic-deformation degree equal to ~7 [6]. As a result of such a treatment, we have produced from thin rapidly quenched ribbons monolithic samples about 0.2 mm thick and 10 mm in diameter.

The structure obtained was investigated by methods of transmission electron microscopy (TEM) using a JEM-200CX microscope, X-ray diffraction analysis (XDA), and thermomagnetic analysis (TMA) on the basis of the techniques developed in [7]. The magnetic characteristics of $Nd_{11.8}Fe_{82.3}B_{5.9}$ samples were measured with a vibrating-coil magnetometer in a magnetic field up to 1.6 MA/m after a preliminary magnetization of samples in a pulsed magnetic field of 5 MA/m. According to the XDA and TEM data, the initial $Ti_{50}Ni_{25}Cu_{25}$ RQA had a completely amorphous structure (Fig. 1a). Annealing the amorphous alloy in various regimes did not result in the appearance of a homogeneous NC structure. For example, annealing at 350°C yet does not provide crystallization. At the same time, on heating to $T = 450$°C, the amorphous phase is crystallized nonuniformly, so that, alongside with the formation of nanocrystals, individual grains appear about 1 μm in size or larger (Fig. 1b). A similar conclusion on the nonuniform crystallization of $Ti_{50}Ni_{25}Cu_{25}$ RQA was made in [4].

In this case, very fine nanocrystals 2–3 nm in size are observed in the sample after SPD (Fig. 2a). In other words, the initial nanocrystallization in the

* *Ufa State Technical University of Aviation,*
  ul. K. Marksa 13, Ufa, Bashkortostan, 450000 Russia
** *Institute of Metal Physics, Ural Division,*
  Russian Academy of Sciences, ul. S. Kovalevskoĭ 18,
  Yekaterinburg, 620219 Russia
  e-mail: dimagun@mail.rb.ru

(a)
(b)
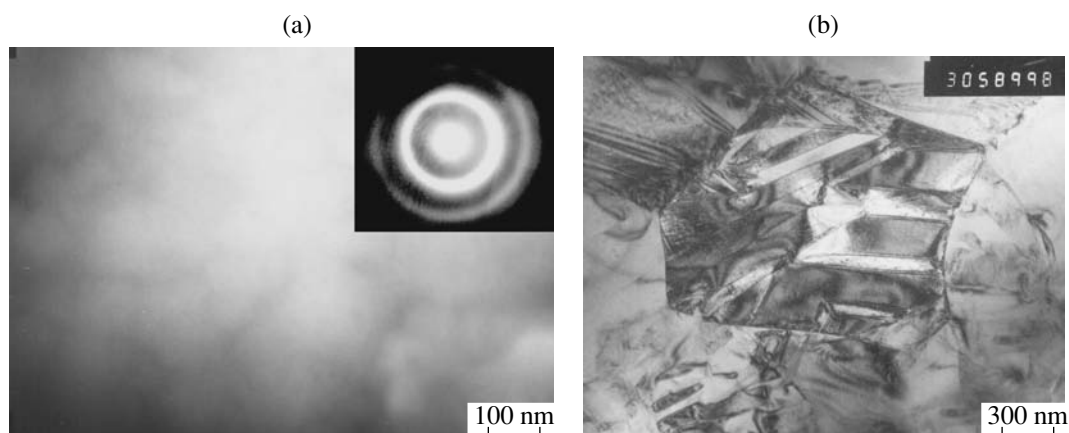
Fig. 1. Rapidly quenched $Ti_{50}Ni_{25}Cu_{25}$ alloy (a) in the initial state and (b) on annealing at 450°C for 10 min.

(a)
(b)
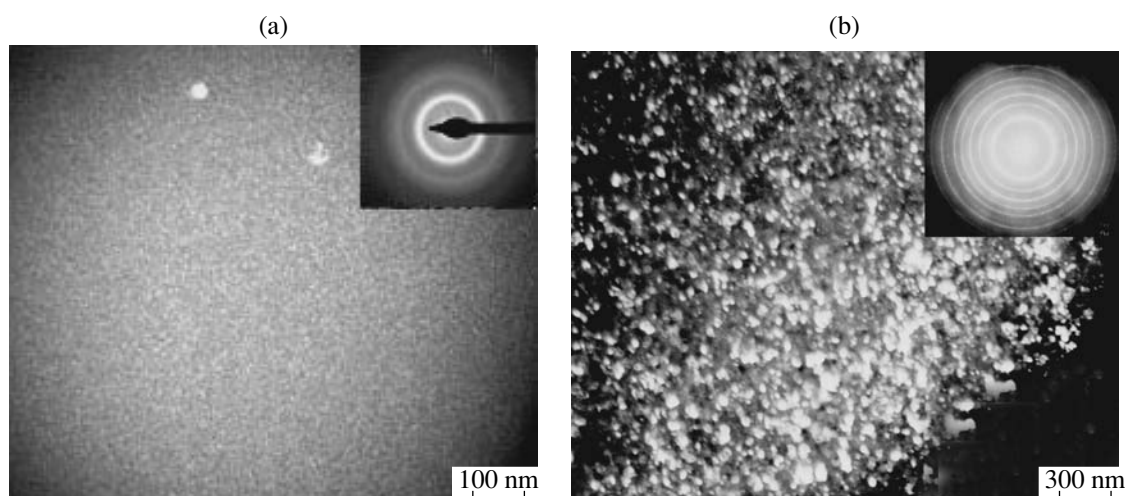
Fig. 2. Rapidly quenched $Ti_{50}Ni_{25}Cu_{25}$ alloy (a) after severe plastic deformation (dark-field image) and (b) after severe plastic deformation and on subsequently annealing at 450°C for 10 min (bright-field image).

$Ti_{50}Ni_{25}Cu_{25}$ RQA proceeds as a result of SPD already at room temperature, attaining $0.19T_{melt}$, which is almost 400°C lower than the crystallization temperature of the initial RQA. According to the TEM data, 10-min annealing of the alloy at 350°C after SPD results in the formation of a homogeneous NC structure with grains about 50 nm in size (Fig. 2b). At the same time, 10-min annealing at 450°C results in the growth of medium-size grains not exceeding 200 nm. Thus, SPD with subsequent annealing made it possible to form homogeneous ultrafine-grained structures with a variable average size of grains.

The measurements showed that the microhardness of monolithic samples obtained in the case of $Ti_{50}Ni_{25}Cu_{25}$ RQA as a result of SPD by torsion attains 5500 MPa (or twice as high as in conventional TiNi alloys with the shape-memory effects), and heating to 350°C does not result in its decrease. The attainment of these high strength properties of materials makes it pos-

sible to expect an increase in parameters of the shape-memory effect, since such an important characteristic as the reactive stress is usually proportional to the strength level.

According to the TEM, TMA, and XDA data, the rapidly quenched $Nd_{11.8}Fe_{82.3}B_{5.9}$ alloy also has, basically, an amorphous structure. However, annealing the alloy at temperatures of 600–700°C results in the formation of $Nd_2Fe_{14}B$-phase grains with an average size of about 40 nm. As a result, high values of coercive force H_c and residual magnetization σ_r (see the table) are attained [7]. This method is used for the industrial production of hard magnetic powders [8]. Nevertheless, according to the TEM observations, α-Fe-phase grains about 10 nm in size appear in the case of $Nd_{11.8}Fe_{82.3}B_{5.9}$ RQA as a result of SPD already at the room temperature. The appearance of the α-Fe phase (up to 30%) in the RQA as a result of SPD is also confirmed by the TMA data [7]. As can be seen in the table,

the $Nd_{11.8}Fe_{82.3}B_{5.9}$ RQA subjected to SPD and subsequent annealing exhibits higher values of H_c and σ_r than the corresponding values of the annealed initial RQA. Also in the table, for comparison, we display properties of a cast coarse-grained $Nd_{11.8}Fe_{82.3}B_{5.9}$ alloy subjected to SPD and annealing [9]. The observed improvement of magnetic properties is associated with the fact that an RQA subjected to SPD and annealing has the most disperse and homogeneous NC structure of the $Nd_2Fe_{14}B$ phase. This fact is of direct practical interest for the production of promising magnets.

Thus, the investigations performed show that the SPD of amorphous rapidly quenched alloys results in an abrupt decrease in their crystallization temperature and, as a result, in the formation of a considerably finer NC structure. It should also be noted that, in the case of an amorphous Ti–Ni–Cu alloy, B2-phase nanocrystals having the same composition as the amorphous matrix are formed in the case of SPD by the polymorphic-crystallization mechanism. As the SPD of a Nd–Fe–B amorphous alloy occurs, the initial α-Fe-phase nanocrystallization proceeds. As is shown in [11], SPD can induce a local redistribution of elements in alloys. In an amorphous Nd–Fe–B alloy, this results in the formation of clusters with an increased concentration of Fe atoms, which turn out to be nanocrystallization centers of the α-Fe phase.

Recently, it was found [10] that uniaxial deformation by compression or stretching at room temperature can promote the nanocrystallization of amorphous alloys. However, in this case, nanocrystals were found only in narrow regions along the shear bands or in fracture areas. In the case of SPD, nanocrystals are uniformly formed already throughout the bulk of the sample.

The size D of a grain formed as a result of the crystallization on heating is determined by both the number of crystallization nuclei N and the grain growth rate V:

$$D = \frac{1.1V}{N}$$ [13]. SPD results in the occurrence of a large number of disperse homogeneously distributed nanocrystals, i.e., nuclei of the subsequent crystallization on heating in an amorphous material. This leads to the formation of a much more homogeneous NC structure on annealing and, correspondingly, to an improvement of

Coercive force H_c and specific residual magnetization σ_r of the $Nd_{11.8}Fe_{82.3}B_{5.9}$ alloy in various states (annealing at 600°C for 10 min)

Alloy state	H_c, kA/m	σ_r, A m^2/kg
RQA + annealing	336	72
RQA + SPD + annealing	528	86.5
Coarse-grained alloy + SPD + annealing	369	87

such important material properties as the strength and coercive force.

REFERENCES

1. H. Gleiter, Prog. Mater. Sci. **33**, 223 (1989).
2. R. W. Siegel and G. E. Fougere, *Nanophase Materials*, Ed. by G. C. Hadjipanayis and R. W. Sigel (NATO ASI Ser., New York, 1989).
3. A. I. Gusev and A. A. Rempel', *Nanocrystalline Materials* (MAIK, Moscow, 2000).
4. P. Schlossmacher, N. Boucharat, H. Rösner, *et al.*, J. Phys. IV (France) **112**, 731 (2003).
5. R. Z. Valiev, A. V. Korznikov, and R. R. Mulyukov, Mater. Sci. Eng., A **168**, 141 (1993).
6. R. Z. Valiev and I. V. Aleksandrov, *Nanocrystalline Materials Prepared by a Severe Plastic Deformation* (Logos, Moscow, 2000).
7. D. V. Gunderov, A. G. Popov, N. N. Shchegoleva, *et al.*, in *Problems of Nanocrystalline Materials*, Ed. by V. V. Ustinov and N. I. Noskova (UrO RAN, Yekaterinburg, 2002), pp. 358–366.
8. J. Fidler and T. Schrefl, J. Appl. Phys. **79**, 5029 (1996).
9. V. S. Gaviko, A. G. Popov, A. S. Ermolenko, *et al.*, Fiz. Met. Metalloved. **92** (2), 58 (2001).
10. H. Chen, Y. He, G. J. Shiflet, and S. J. Poon, Nature **363**, 367 (1994).
11. V. L. Gapontsev, A. G. Kesarev, V. V. Kondrat'ev, and A. E. Ermakov, Fiz. Met. Metalloved. **89** (5), 430 (2000).
12. F. Hessner, *Recrystallization of Metallic Materials* (Metallurgiya, Moscow, 1982).

Translated by V. Bukhanov

===================== **MECHANICS** =====================

Bifurcations under Perturbations Violating Cosymmetry

V. I. Yudovich

Presented by Academician G.G. Chernyĭ March 5, 2004

The presence of one-parameter families of equilibria, in particular, an equilibrium cycle, is a characteristic property of cosymmetric dynamical systems [1, 2]. In the case of a system with *n* cosymmetries, it has *n*-dimensional submanifolds of equilibria [3, 4]. When disturbed by perturbations violating cosymmetry, the continuous families of equilibria disintegrate or even disappear. The latter case is of special interest, because more complicated regimes, as well as slow (long-period) periodic motions, could originate in the system.

This paper is devoted to such bifurcation phenomena.

To illustrate the general theory, we analyze the disintegration of families of equilibria in a plane with a skew-symmetric cosymmetry. We then consider the problem of plane filtration convection in the presence of low-intense heat sources or under weak fluid infiltration. In both these cases, the cosymmetry is violated so that a family of steady-state regimes disintegrates to produce either separate steady-state regimes or a long-period regime (slow cycle).

The cosymmetry of a mechanical system corresponds to a symmetry group of its potential energy (the reverse statement is also true). If the symmetry group does not conserve the kinetic energy, the corresponding cosymmetry is nonholonomic. For example, this occurs when two particles of different masses m_1 and m_2 move in an axisymmetric potential field. The angular momentum of such a system is conserved only if $m_1 = m_2$. When $m_1 \neq m_2$, the family of equilibria of the system is conserved, but its dynamics significantly changes so that the system becomes, generally speaking, nonintegrable with a variable equilibrium spectrum of the family. We consider here the decay of a family of equilibria under perturbations of the potential energy. In this case, the family cannot entirely disappear, because some of its members produce equilibrium branches of the perturbed system.

The basic relevant theoretical results have been presented in [5, 6]. The cosymmetry violation in the problem of filtration convection was considered in [7], where large perturbations were analyzed numerically.

––––––––––––––––––

Rostov State University,
ul. Zorge 5, Rostov-on-Don, 344090 Russia

DISINTEGRATION OF A MANIFOLD OF EQUILIBRIA FOR AN EQUATION WITH MULTICOSYMMETRY

We consider the nonlinear differential equation

$$\dot{x} = Fx + \delta Kx \qquad (1)$$

in a real Hilbert space H. We assume that the vector field F has a multicosymmetry $L = \{L_j\}_{j=1, 2, \dots, m}$ such that

$$(Fx, L_1x) = 0, (Fx, L_2x) = 0, \dots, (Fx, L_mx) = 0 \qquad (2)$$

for all $x \in H$. Here, δ is a perturbation parameter further assumed to be small. The fields F and K are assumed to be analytical, even though the assumption of their C^2 smoothness is sufficient to derive the majority of the subsequent results.

Let a certain equilibrium $\bar{x}$ of the unperturbed equation

$$\dot{x} = Fx, \qquad (3)$$

be known, so that $F\bar{x} = 0$. We suppose that the following hypotheses of the cosymmetric generalization of the implicit-function theorem are satisfied [3, 4]:

(*1*) The solution $\bar{x}$ is a regular point of the multicosymmetry L; i.e., the covectors $L_1\bar{x}$, $L_2\bar{x}$, …, $L_m\bar{x}$ are linearly independent.

(*2*) The degeneracy is minimal; i.e., $\ker F'^*(\bar{x}) = \mathrm{Lin}\{L_1\bar{x}, L_2\bar{x}, \dots, L_m\bar{x}\}$.

(*3*) The kernel of the derivative $F'(\bar{x})$ is finite-dimensional and $\dim \ker F'(\bar{x}) = m$.

(*4*) The image of the operator $F'(\bar{x})$ is closed.

Under these conditions and according to [3, 4], the set of equilibria of Eq. (1) in the neighborhood of the point $\bar{x}$ is an *m*-dimensional submanifold Σ in H, which is tangent to the subspace $\bar{x} + \ker F'(\bar{x})$ at the point $\bar{x}$.

We now introduce a cosymmetric defect of a given perturbation δK, namely, a mapping $S = S_K: H \longrightarrow R^m$, which is defined for any $x \in H$ by the equality

$$Sx$$
$$= (Kx, Lx) \overset{\text{def}}{=} ((Kx, L_1x), (Kx, L_2x), \ldots, (Kx, L_mx)). \tag{4}$$

Below, we are based on the following lemma and its corollary.

Lemma 1. *Let $\bar{x}$ be a solution of the equation $Fx = 0$ with a nonzero cosymmetric defect: $F\bar{x} = 0$, $S\bar{x} \neq 0$. In this case, there exists a neighborhood Ω of the point $\bar{x}$ such that Eq. (1) with an arbitrary $\delta \neq 0$ has no equilibria in this neighborhood:*

$$Fx + \delta Kx = 0. \tag{5}$$

Proof. The proof is evident. Multiplying the equilibrium equation $Fx + \delta Kx = 0$ by $L_1x, L_2x, \ldots, L_mx$, we arrive at the equality $Sx = 0$. Then, we take the continuity of the mapping S into account.

Corollary. *Let $\delta_n \longrightarrow 0$, x_n be the solution of the equation $Fx + \delta_n Kx = 0$ and $x_n \longrightarrow \bar{x} \in \Sigma$. Then, the equality*

$$S\bar{x} = 0 \tag{6}$$

is valid.

Equality (6) with the unknown $\bar{x}$ on the submanifold Σ is referred to as a selection equation. There are two methods for defining the submanifold Σ, namely, using either the implicit equation $Fx = 0$ or the parametrization $\Sigma = \{c(\theta)| c: M \longrightarrow H\}$, where c is the known mapping of a standard manifold M onto H. The selection equation can be written, respectively, in two forms: as the set

$$Fx = 0, \quad Sx = 0 \tag{7}$$

or as the equation

$$S(c(\theta)) = 0. \tag{8}$$

The following theorem states that each nondegenerate solution of the selection equation produces a continuous (smooth) branch of solutions of equilibrium equation (5).

Theorem 1. *Let hypotheses (1)–(4) be satisfied and $\bar{x}$ be a nondegenerate solution of selection equation (6) in the sense that $\mathrm{Im}\, S'(\bar{x}) \in R^m$. Then, there exists a neighborhood Ω of the point $\bar{x}$ and an interval $\mathscr{I} = (-\delta_0, \delta_0)$ with $\delta_0 > 0$ such that Eq. (5) with an arbitrary $\delta \in \mathscr{I}$ in Ω has a unique solution $x = \psi(\delta)$. In this case, the mapping $\psi: \mathscr{I} \longrightarrow H$ is smooth and $\psi(0) = \bar{x}$.*

Using Theorem 1 and the conventional procedure of finite covers of a compact set, we arrive at the following statement.

Theorem 2. *Let Σ be the compact closed submanifold of H formed by equilibria of the cosymmetric equa-*

tion $Fx = 0$. *All the equilibria are assumed to be regular (i.e., satisfy the hypotheses of the cosymmetric generalization of the implicit-function theorem).*

Let the number r of solutions $\bar{x}_1, \bar{x}_2\ldots, \bar{x}_r$ of selection equation (6) be finite and let all the solutions be nondegenerate.

In this case, there exist a neighborhood Ω of the submanifold Σ in H and a neighborhood $(-\Delta, \Delta)$ of zero such that Eq. (5) with an arbitrary $\delta \in (-\Delta, \Delta)$ has r solutions $x_1(\delta), x_2(\delta), \ldots, x_r(\delta)$ in Ω. All the solutions are nondegenerate and depend analytically on δ. If the selection equation has no solutions, then the equation $Fx + \delta Kx = 0$ also has no solutions in Ω for $\delta \in (-\Delta, \Delta)$.

When $m = 1$, the submanifold Σ is a cycle of equilibria. If the cycle is asymptotically stable in the linear approximation, then the number r of equilibria of the perturbed equation is even, whereas stable and unstable equilibria alternate.

It is worth noting that the finiteness condition for the number of solutions of the selection equation is always satisfied provided that the cosymmetry is unique and the fields F and K are analytical.

SLOW CYCLES

If the selection equation has no solutions and the family of equilibria disappears, the problem is reduced to studying dynamics of a perturbed system near its decayed family of equilibria. In the general form, the problem has not been solved to date. We consider here only the case of a single cosymmetry L and an isolated cycle of equilibria, i.e., $C = \{c(\theta)| \theta \in S^1\}$, where θ is an angular variable.

Theorem 3. *Let the hypotheses of Theorem 2 be satisfied and the field F have a single cosymmetry L. Let selection equation (8) have no solutions. Let the cycle C be assumed in a linear approximation to be exponentially asymptotically stable. In this case and for small δ, there exists an asymptotically stable limit cycle in the neighborhood of the cycle C. The period T_δ of the corresponding motion admits the asymptotic behavior $T_\delta = P_0\delta^{-1} + O(1)$, $\delta \longrightarrow 0$, where the coefficient P_0 is defined by the equalities*

$$P_0 = \oint_C \frac{(dc(\theta), Lc(\theta))}{s(\theta)} = \int_0^{2\pi} \frac{k(\theta)}{s(\theta)} d\theta,$$

$$s(\theta) = S(c(\theta)) = (Kc(\theta), Lc(\theta)), \tag{9}$$

$$k(\theta) = (c'(\theta), Lc(\theta)).$$

It is noteworthy that, under the conditions of Theorem 3, the functions $s(\theta)$ and $k(\theta)$ do not vanish anywhere. The theorem is proved by constructing the complete asymptotic solution as $\delta \longrightarrow 0$ with the help of the two-scale expansion method. The proof is obtained on the basis of the Kantorovich theorem [9] on the abstract Newton's method (to be more precise, on the

part concerning the existence and the local uniqueness of the solution; in this case, Newton's approximations need not be constructed).

TWO-DIMENSIONAL SYSTEMS WITH A SKEW-SYMMETRIC COSYMMETRY

An autonomous system on the plane $\mathbb{R}^2$, which has the cosymmetry L defined by the matrix $L = \begin{pmatrix} 0 & 1 \\ -1 & 0 \end{pmatrix}$, can be written in the form

$$\dot{x} = xf(x, y), \quad \dot{y} = yf(x, y) \qquad (10)$$

where f is assumed to be an analytical function. The zero equilibrium of system (10) is cosymmetric, while nonzero equilibria are not cosymmetric and are defined by the equation

$$f(x, y) = 0. \qquad (11)$$

We consider the perturbed system

$$\dot{x} = xf + \delta(xg + yh), \quad \dot{y} = yf + \delta(xu + yv), \quad (12)$$

where q, h, u, and v are given smooth functions of x and y, with δ being a perturbation parameter. The corresponding selection equation takes the form of the set

$$s(x, y) \overset{\text{def}}{=} y(xg + yh) - x(xu + yv) = 0, \qquad (13)$$
$$f(x, y) = 0.$$

In order for the equilibrium $\theta_0 = (x_0, y_0)$ to produce a branch $\theta(\delta) = (x(\delta), y(\delta))$, it is necessary that the equality $s(x_0, y_0)$ be satisfied and, according to Theorem 1, it is sufficient that the point (x_0, y_0) be a nondegenerate solution of selection equation (13), i.e., the inequality

$$\begin{vmatrix} s_x(x_0, y_0) & s_y(x_0, y_0) \\ f_x(x_0, y_0) & f_y(x_0, y_0) \end{vmatrix} \neq 0 \qquad (14)$$

be satisfied.

Proposition 1. *Let $\theta_0 = (x_0, y_0)$ be a solution of selection equation* (13) *on Γ. If condition* (14) *is fulfilled, then there exists a neighborhood of the point θ_0 such that, for any small $\delta \neq 0$, there exists in the neighborhood the unique equilibrium $\theta(\delta) = \{x(\delta), y(\delta)\}$ depending analytically on δ, with $\theta(0) = \theta_0$. The solution is stable for $x_0 f_x^0 + y_0 f_y^0 < 0$ and unstable for $x_0 f_x^0 + y_0 f_y^0 > 0$. If the set of solutions of Eq.* (11) *contains a closed curve with the nonvanishing selection function, then, for small δ, the perturbed system has a limit cycle.*

In the polar coordinates r and φ, the set of Eqs. (10) takes the form $\dot{r} = rq(r, \varphi)$, $r\dot{\varphi} = 0$, where $q(r, \varphi) = f(r\cos\varphi, r\sin\varphi)$. If $q = a^2 - r^2$ ($a = \text{const}$) and $K =$

$r^n(\cos n\varphi, \sin n\varphi)$, with n being a natural number, then selection equation (13) can be written as

$$s_K(\varphi) = (K\theta, L\theta)|_{\theta = (a, \varphi)} = -a^{n+1} \sin(n-1)\varphi = 0. \qquad (15)$$

When $n = 1$, the system of Eqs. (12) remains cosymmetric and has the stable cycle of equilibria $r^2 = a^2 + \delta$ for $\delta > -a^2$. When $n = 2, 3, \ldots$, selection function (13) vanishes only at $2(n - 1)$ points $\varphi_k = kh_n$, where h $h_n = \dfrac{\pi}{n-1}$ and $k = 0, 1, \ldots, 2(n-1) - 1$. Therefore, the system has $2(n-1)$ equilibria, with alternating stable and unstable equilibria.

BIFURCATION OF A STEADY-STATE CYCLE UNDER FILTRATION CONVECTION

The problem of filtration convection in a simply connected region $D \subset R^2$ is reduced to the following system of differential equations and boundary conditions for the stream function ψ and the temperature θ:

$$\frac{\partial \theta}{\partial t} = \Delta\theta - \lambda\psi_x - (\psi_y\partial_x - \psi_x\partial_y)\theta + \mu f(x, y), \quad (16)$$

$$-\Delta\psi = \theta_x, \qquad (17)$$

$$\psi|_{\partial D} = 0, \quad \theta|_{\partial D} = 0. \qquad (18)$$

Here, μf is the heat source density and μ and λ are real-valued parameters. If $\mu = 0$, then the system is cosymmetric [1]. Indeed, multiplying Eq. (16) by ψ and integrating the product over the region D with regard to Eq. (17), we arrive at the zero identity. As was noted in [10] and rigorously proved in [1], there exists a critical value $\lambda_0 > 0$ of the filtration Rayleigh number λ such that, for $\lambda > \lambda_0$ the system of Eqs. (16)–(18), if weakly unstable, has a one-parameter family of steady-state solutions, i.e., an equilibrium cycle. We now consider the bifurcation of the equilibrium cycle under the action of heat sources with a small parameter μ.

Using the reduction of the boundary value problem to operator equation (1), we can easily derive the selection equation corresponding to a given perturbation μf. Indeed, multiplying Eq. (16) by ψ and integrating the result over the region D, we arrive at the equation

$$\int_D f(x, y)\psi(x, y)dxdy = 0, \qquad (19)$$

which should be considered on the equilibrium cycle.

We introduce the solution h of the boundary value problem $-\Delta h = f$ with $h|_{\partial D} = 0$ and rewrite the selection equation in the equivalent form

$$\int_D h_x(x, y)\theta(x, y)dxdy = 0. \qquad (20)$$

The steady-state solutions can be expanded in a Lyapunov–Schmidt power series in terms of the small parameter $\varepsilon = \sqrt{\lambda - \lambda_0}$:

$$\theta = \varepsilon\theta_1 + \varepsilon^2\theta_2 + \ldots, \quad \psi = \varepsilon\psi_1 + \varepsilon^2\psi_2 + \ldots \quad (21)$$

In this case, the functions θ_1 and ψ_1 are defined with an accuracy to an arbitrary angular variable τ on the equilibrium cycle. Therefore,

$$\theta_1 = \rho_1(\varphi\cos\tau - \chi\sin\tau),$$
$$\psi_1 = -\lambda_0^{-1/2}\rho_1(\varphi\sin\tau + \chi\cos\tau). \quad (22)$$

Here, $\rho_1 > 0$ is a given constant; φ and χ are real-valued functions; and $\varphi + i\psi = w$ is an eigenfunction of the operator $L = GD$, where G is the Green's operator of the Dirichlet problem for the operator $-\Delta$ and $D = \dfrac{\partial}{\partial x}$ with $w = i\sqrt{\lambda_0}\,Lw$. Substituting Eqs. (22) into Eqs. (19) and (20), we arrive at the selection equation

$$A\cos\tau + B\sin\tau + \ldots = 0, \quad (23)$$

where the first- and higher-order terms in ε are omitted. The constants A and B are determined by the formulas

$$A = \int\limits_{D} f(x, y)\varphi(x, y)dxdy,$$
$$B = \int\limits_{D} f(x, y)\chi(x, y)dxdy. \quad (24)$$

When $A^2 + B^2 > 0$, Eq. (23) can be written as $\sin(\tau - \tau_0) = 0$ with an accuracy to the first order in ε. This equation has two roots, τ_0 and $\tau_0 + \pi$ (modulo 2π), which are simple and, therefore, do not vanish for small ε. We now formulate the result obtained above.

Proposition 2. *Let the function f be such that at least one of integrals (24) is nonzero. In this case, for small values of the parameter* $\varepsilon = \sqrt{\lambda - \lambda_0}$, *the effect of sources with small density* μf *on the system of Eqs. (16)–(18) results in the bifurcation of the steady-state cycle existing for* $\mu = 0$ *with only two (one stable and one unstable) steady-state regimes surviving.*

The general method employed above to derive the selection equation can be extended to fairly arbitrary small disturbances of system (16)–(18).

We now consider an infiltration problem, when an inhomogeneous boundary condition $\psi|_{\partial D} = \eta q(x, y)$ is imposed on ψ. Let $\mu = 0$. To derive the selection equation, we write out the scalar {in $L_2(D)$} product of Eq. (16) and ψ and integrate it by parts. As a result, we obtain the equality

$$\int\limits_{\partial D} q\frac{\partial\theta}{\partial n}ds - \lambda\eta\int\limits_{\partial D}\frac{q^2}{2}n_x ds = 0, \quad (25)$$

where $n = (n_x, n_y)$ is the unit outer normal. Assuming that $\theta \longrightarrow \bar{\theta}$ as $\eta \longrightarrow 0$, we arrive at the selection equation

$$\int\limits_{\partial D} q\frac{\partial\bar{\theta}}{\partial n}ds = 0. \quad (26)$$

The passage to the limit in integrals (25) taken over the boundary is easily substantiated by reducing them to surface integrals with the help of the solution Φ of the Dirichlet problem $\Delta\Phi = 0$, $\Phi|_{\partial D} = q$.

Proposition 3. *Let at least one of the constants*

$$A_1 = \int\limits_{\partial D} q\frac{\partial\varphi}{\partial n}ds, \quad B_1 = \int\limits_{\partial D}\frac{\partial\chi}{\partial n}ds \quad (27)$$

be nonzero (the functions φ *and* χ *were defined above). In this case, the weak injection of a fluid into the region D (provided that the parameter* $\lambda - \lambda_0$ *is small) results in the bifurcation of the cycle of equilibria (steady flows). Only two (one stable and one unstable) steady-state equilibria survive. As before, they are defined by Eq. (23) with the substitution of A (B) by* A_1 *(B_1).*

The case that the cycle of equilibria disappears can also take place in the infiltration problem. In particular, if $q(x, y) = y$, the system of Eqs. (16)–(18) with $\mu = 0$ has the steady-state solution $\theta_0 = 0$, $\psi_0 = \eta y$. Passing to perturbations and performing the change of variables $\theta \longrightarrow \theta$ and $\psi \longrightarrow \psi + \eta y$, we arrive at the heat conduction equation

$$\frac{\partial\theta}{\partial t} = \Delta\theta - \lambda\psi_x + \psi_x\theta_y - \psi_y\theta_x - \eta\theta_x. \quad (28)$$

Equation (17) and boundary conditions (18) remain valid as before. Multiplying Eq. (28) by ψ and integrating the product over the region D with $\eta \neq 0$, we obtain the relation

$$\int\limits_{D} (\nabla\psi)^2 dxdy = 0.$$

Thus, for any $\eta \neq 0$, Eqs. (28), (17), and (18) have no nonzero steady-state solutions. As the parameter η tends to zero, the cycle of steady motions disintegrates to produce a self-oscillating regime with a long period $O\left(\dfrac{1}{\eta}\right)$ as $\eta \longrightarrow 0$.

EQUILIBRIA OF A CONSERVATIVE SYSTEM

We now consider the equation of motion of a mechanical system in R^n or in H:

$$\ddot{x} = -\text{grad}(V(x) + \delta W(x)). \quad (29)$$

Here, $V + \delta W$ is the potential energy and δ is a small parameter. We assume that the unperturbed field $\text{grad}\,V$

has a cosymmetry L such that

$$(\mathrm{grad}\,V(x),\,Lx) = 0 \qquad (30)$$

for all x. Such a situation was discussed in [1, 3, 5, 11].

The case of the potential energy $V = V\left(\dfrac{x_1^2}{a_1^2} + \dfrac{x_2^2}{a_2^2}\right)$ with

the cosymmetry $Lx = \left(\dfrac{x_2}{a_2^2},\, -\dfrac{x_1}{a_1^2}\right)$ is a typical example.

Only if $a_1 = a_2$ does the cosymmetry become holonomic and imply the conserved angular momentum. The potential energy of this type describes the interaction of two particles with masses m_1 and m_2 moving in an axisymmetric field, provided that the change of variables $x_1 \longrightarrow \sqrt{m_1}\,x_1$ and $x_2 \longrightarrow \sqrt{m_2}\,x_2$ is performed with $a_1 = \sqrt{m_1}$, and $a_2 = \sqrt{m_2}$.

It follows from the existence of the cosymmetry L, though nonholonomic, that the function V is invariant with respect to translations along trajectories of the field Lx; namely, if $U_s = \exp(sL)$ is the corresponding evolution operator, then $V(U_s x) = V(x)$. Therefore, in addition to the solution x_0, the unperturbed equation

$$\mathrm{grad}\,V(x) = 0 \qquad (31)$$

has a family of solutions $c(s) = U_s x_0$, with $c(0) = x_0$. When $Lx_0 \neq 0$, the family, if compact, is a cycle of equilibria. The selection equation corresponding to Eq. (29) takes the form

$$(\mathrm{grad}\,W(x),\,Lx)|_{x = c(s)} = 0. \qquad (32)$$

The analysis of this equation yields the following proposition.

Proposition 4. *Let Eq.* (31) *with a cosymmetry L have a cycle of equilibria $C = \{c(s)\}$, where s is an angular variable. This cycle is assumed to be stable in a linear approximation. Let the selection function {see Eq.* (32)} *not vanish identically and all solutions of Eq.* (32) *be nondegenerate. In this case, perturbed equation* (29) *with small δ has k stable and k unstable alternating analytical branches of equilibria $x_1(\delta)$, $x_2(\delta)$, …, $x_{2k}(\delta)$. Here, k is a positive natural number. There exist no equilibria in the neighborhood of the cycle C, which is independent of δ.*

We note that, in this case, all equilibria of the cycle cannot disappear under a perturbation.

ACKNOWLEDGMENTS

REFERENCES

1. V. I. Yudovich, Mat. Zametki **49** (5), 142 (1991).
2. V. I. Yudovich, Chaos **5** (2), 402 (1995).
3. V. I. Yudovich, Mat. Zametki **60** (2), 313 (1996).
4. V. I. Yudovich, in *Linear Topological Spaces and Complex Analysis* (Ankara Univ., Ankara, 1995), Vol. 2, pp. 105–125.
5. V. I. Yudovich, *Bifurcations Caused by the Cosymmetry Breaking in Dynamical Systems*, Available from VINITI, No. 2002-V96 (Rostov-on-Don, 1996), Part 1.
6. V. I. Yudovich, *Bifurcations Caused by the Cosymmetry Breaking in Dynamical Systems*, Available from VINITI, No. 2736-V96 (Rostov-on-Don, 1996), Part 2.
7. D. Bratsun, D. Lyubimov, and B. Roux, Physica D **82**, 398 (1995).
8. V. I. Yudovich, in *Proceedings of the ICIAM'95, Hamburg, 1995* (Hamburg, 1995), Vol. 4, pp. 585–588.
9. L. V. Kantorovich and G. P. Akilov, *Functional Analysis in Normalized Spaces* (Fizmatgiz, Moscow, 1959).
10. D. V. Lyubimov, Prikl. Mekh. Tekh. Fiz. **2**, 131 (1975).
11. V. I. Yudovich, *Absence of Static Symmetry Groups for Cosymmetric Dynamical Systems*, Available from VINITI, No. 929-V93 (Rostov-on-Don, 1993).

Translated by V. Chechin

=========== **MECHANICS** ===========

Flight Overloading Effect on the Working-Process Instability in the Combustion Chamber of a Solid-Fuel Rocket Engine

Yu. M. Davydov*, I. M. Davydova*, and M. Yu. Egorov**

Presented by Academician G.G. Chernyĭ March 10, 2004

Received March 24, 2004

The problem of the working-process instability in its various manifestations arose with the beginning of the development and use of the first solid-fuel rocket engines [1–3], engines operating on liquid fuel [2, 4] and other types of fuels [5], and plasma rocket engines [6]. At present, in connection with the development of new-generation high-performance solid-fuel engines, the problem has only become even more urgent.

Generally, the working-process instability of a solid-fuel engine can be of both acoustic and nonacoustic, highly nonlinear nature [2–4, 5, 7]. The acoustic instability considered in this study is associated with the occurrence of periodic, both low-frequency and high-frequency, pressure fluctuations in the engine combustion chamber. The low-frequency pressure fluctuations within the approximate frequency range $f \approx$ 20–2500 Hz manifest themselves mainly in the longitudinal direction of the combustion chamber. The high-frequency pressure fluctuations at frequencies $f > 2500$ Hz manifest themselves in the transverse and tangential directions of the combustion chamber.

The most hazardous is the low-frequency acoustic instability of the solid-fuel engine working process. This type of instability is characterized by a considerable deviation of both the working pressure in the combustion chamber and the engine thrust from their mean values. This disturbs the normal working process of a nozzle, initiates the transfer of rigid periodic vibratory loads to the rocket system as a whole, is a source of intense unmasking noise, etc.

In monographs [7, 8], the actual oscillatory process was reproduced for the first time by direct numerical simulation, and the mechanism of the generation and the maintenance of the acoustic instability in the solid-fuel engine combustion chamber was investigated. The reasons for the occurrence (excitation and mainte-

nance) of the oscillatory process should be sought in the structure and nature of the combustion-product flow in the rocket engine combustion chamber (naturally, with regard for the interaction of the flow with the burning surface of the solid-fuel charge). Here, the fluctuations are of a hydrodynamic (gas-dynamic) deeply nonlinear nature. The fluctuation frequency (the first, second, and other longitudinal modes) and, especially, amplitude are dependent on a number of factors. The principal factor is the presence of a considerable radial stratification of the combustion-product flow in the chamber with respect to the flow parameters, mainly, to the velocity. At the nozzle inlet, the flow of such a complicated structure interacts irregularly with the wall of the rear engine bottom and is partially reflected from it (both the flow itself and the flow-induced disturbances are reflected). In the base region near the lateral wall of the combustion chamber, either a reverse flow (with respect to the main flow) is formed or the flow is considerably decelerated. Thus, in the solid-fuel engine combustion chamber, an unsteady, transient, low-frequency acoustic pulsating flow is generated and then periodically maintained due to finite dimensions of the combustion chamber.

This study is the first attempt of numerically investigating an effect of the flight overloading on the low-frequency acoustic operation instability of the solid-fuel engine combustion chamber. The operating conditions of a rocket engine on a test rig and in flight are quite different. One of the main distinctive factors is the gravity-field effect. The flight overloading, in particular, its large values in the final stage of rocket acceleration at almost complete burning-out of the fuel, has an appreciable and nonunique effect on the performance of the solid-fuel engine and the rocket system as a whole. At large flight overloading, an additional, even insignificant action of the rocket engine on the control system and on the payload can result in an emergency situation.

Direct numerical simulation of the low-frequency acoustic instability in solid-fuel engines with account for the flight overloading was performed using the large-particle method [9, 10], which provided good results in solving many nonlinear problems of mechanical engineering and mechanics of continuous and dry-

* *Institute of Engineering Industry Mechanics,*
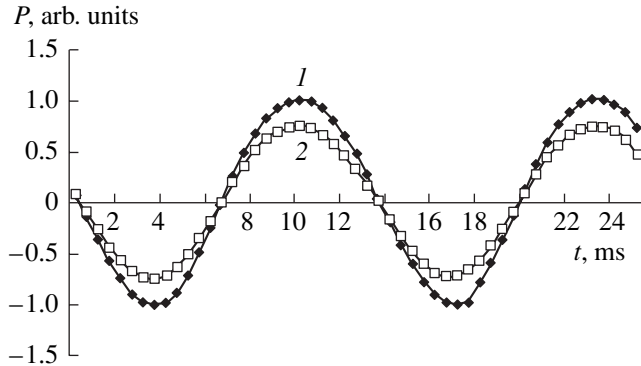 *Moscow, Russia*
  e-mail: institut@pochtamt.ru; davydova@pochtamt.ru
** *Perm State Technical University,*
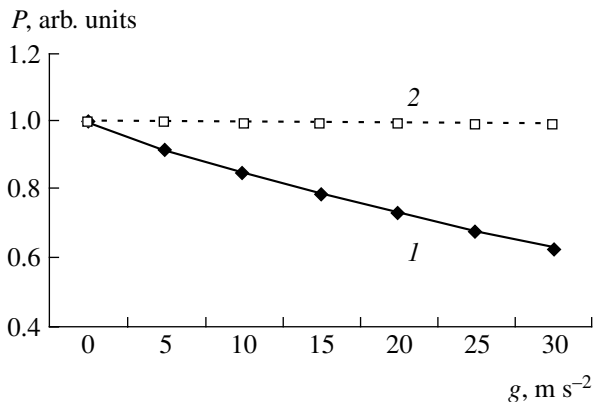 *Komsomol'skiĭ pr. 29a, Perm, 614600 Russia*
  e-mail: egorov@rstu.ac.ru
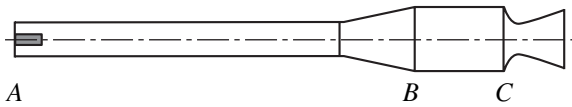
Fig. 1. Schematic diagram of the free-space arrangement of the combustion chamber of the solid-fuel rocket engine under consideration.

Fig. 2. Time variation of the combustion product pressure in the rocket engine chamber in the absence (*1*) and presence (*2*) of flight overloading.

Fig. 3. Dependence of the pressure fluctuation amplitude (*1*) and the mean pressure (*2*) in the rocket engine chamber on the flight overloading.

substance flowing media [11]. In the calculations, the explicit parametric (with four parameters) completely conservative finite-difference scheme of the method was used. The approaches developed in mechanics of multiphase heterogeneous media [12] were applied to the description of the flow in the solid-fuel engine combustion chamber and in the nozzle. As a baseline physical and mathematical model, the complete time-dependent system of vortical differential gas-dynamic equations for a heterogeneous medium (gas and solid particles) written in the conservation-law form was used. The model allows for the gravity-field effect at accelerated motion of a rocket. The problem was studied in the axisymmetric formulation. A uniform orthogonal computational grid ensuring the homogeneity of the computational space [8] was used. The fractional-

cell approach was used on irregular (i.e., not coinciding with the grid) boundaries of the computational domain. The solid-fuel charge coming from the burning surface is realized in the form of injection of combustion products with preliminarily determined parameters dependent on both the solid-fuel composition and parameters of the flow over the burning surface into computational cells located on the burning surface.

We now consider some results of the calculation.

The schematic diagram for the free space of the combustion chamber of the solid-fuel engine under consideration is presented in Fig. 1. Here, *A* is the leading bottom, *AB* is the burning surface, *BC* is the combustion chamber wall, and *C* is the rear bottom.

We first present (for further comparison) the results obtained in the absence of flight overloading. Curve *1* in Fig. 2 presents the time variation (for several oscillation periods) of the combustion-product pressure in the engine chamber. The current pressure is referred to the pressure fluctuation amplitude. The pressure is taken in the region of the leading wall of the engine (position *A* in Fig. 1). The pressure fluctuation frequency is $f = 77$ Hz. The oscillatory process is stable. After the chamber flow has attained its steady state regime, the pressure fluctuation amplitude almost does not vary.

The analogous (in principle) oscillatory process is observed in a solid-fuel engine in the presence of flight overloading, though the fluctuation intensity varies. In Fig. 2, the time variation (for several oscillation periods) of the combustion product pressure in the rocket engine chamber at a fixed flight overloading $P = 20g$ is plotted as curve *2*. Here, the current pressure is also referred to the pressure fluctuation amplitude in the absence of flight overloading, and the pressure is also taken in the region of the leading bottom of the engine (position *A* in Fig. 1). The pressure fluctuation frequency is $f = 77.5$ Hz. The oscillatory process is stable. After the chamber flow has reached the steady state, the pressure fluctuation amplitude does not vary.

Curve *1* in Fig. 3 shows the dependence of the pressure fluctuation amplitude in the rocket engine chamber on the flight overloading. Here, the current pressure fluctuation amplitude is also normalized to the pressure fluctuation amplitude in the absence of flight overloading.

Curve *2* in Fig. 3 corresponds to the variation of the average (over an oscillation period) pressure in a rocket engine combustion chamber as a function of the flight overloading. The current average pressure is also divided by the average pressure in the absence of flight overloading.

As the flight overloading increases, the pressure fluctuation amplitude in the solid-fuel engine combustion chamber decreases almost linearly (curve *1* in Fig. 3). Thus, the flight overloading $P = 20g$ (see Figs. 2 and 3) reduces the pressure fluctuation amplitude by a factor of 1.4, with the fluctuation frequency remaining practically the same. The mean pressure in

U_1, m s^{-1}
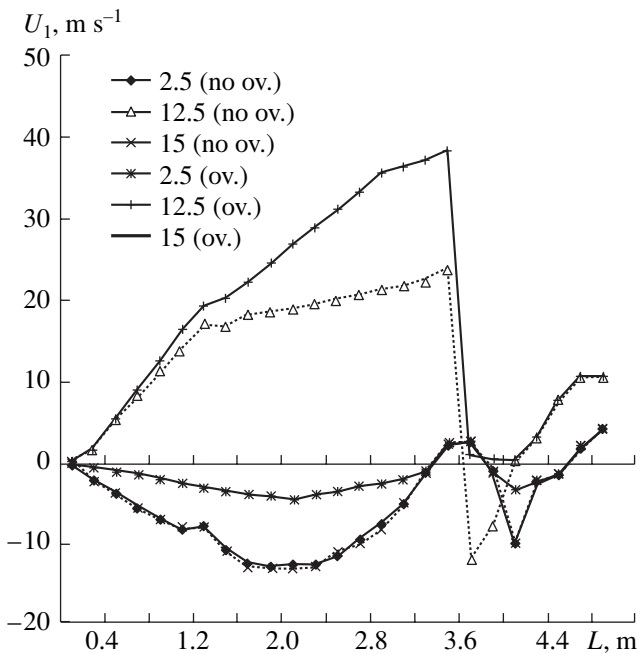
Fig. 4. Profiles of the longitudinal velocity of the gaseous combustion-product motion along the chamber wall and the burning surface of the engine charge at different instants of time within the oscillation period in the absence (no ov.) and presence (ov.) of flight overloading $P = 20g$.

the rocket engine combustion chamber also decreases, though only slightly (curve *2* in Fig. 3).

However, in this case, a certain reduction in the pressure fluctuation amplitude in the rocket-engine chamber and, consequently, in the thrust propulsion fluctuation amplitude practically does not lead to improvement of the solid-fuel engine operation. The conditions of the rocket flight at a considerable overloading accompanied by a low-frequency fluctuating operation mode of the rocket engine are critical even at low pressure and thrust fluctuation amplitudes, which is corroborated in practice. These solid-fuel engine operation regimes should be exhaustively studied under ground-based conditions before costly full-scale flight testing.

The calculated results are in good agreement with the full-scale flight testing data for several rocket systems, including a rocket system equipped with the solid-fuel engine under consideration in this study. Thus, the conclusions made in [7, 8] on the hydrodynamic (gas-dynamic), highly nonlinear nature of low-frequency acoustic pressure fluctuations associated with the structure and the nature of the flow in the solid-fuel engine combustion chamber are again confirmed. In this case, the secondary flow (reverse with respect to the main flow) in the solid-fuel engine combustion chamber, which moves from the rear bottom (Fig. 1, position *C*) along the chamber wall (position *BC*) and the burning surface (position *AB*) to the leading bottom of the engine (position *A*), is decelerated under the action of flight overloading. In Fig. 4, we have plotted the profiles of the longitudinal velocity of the gaseous

combustion-product motion along the chamber wall and the burning surface of the solid-fuel charge at different instants of time (within an oscillation period) in the absence (no ov.) and presence (ov.) of the $P = 20g$ flight overloading. The period of the low-frequency oscillations under study is about 13.0 ms; therefore, the curves corresponding to 2.5 and 15.5 ms are almost coincident. Under the action of flight overloading, the mass of combustion products arrived at the region of the leading bottom of the engine is reduced, which, in turn, reduces the pressure fluctuation amplitude in the solid-fuel engine combustion chamber and, hence, the rocket engine thrust fluctuation amplitude.

REFERENCES

1. *Solid Propellant Rocket Research,* Ed. by M. Summerfield (New York, 1960; IL, Moscow, 1965).

2. T. M. Mel'kumov, N. I. Melik-Pashaev, P. G. Chistyakov, and A. G. Shiutov, *Rocket Engines* (Mashinostroenie, Moscow, 1976).

3. B. T. Erokhin and A. M. Lipanov, *Unsteady and Quasi-Steady Operation Modes of Solid-Fuel Rocket Engines* (Mashinostroenie, Moscow, 1977).

4. K. S. Kolesnikov, *Longitudinal Oscillations of a Rocket with a Liquid-Fuel Engine* (Mashinostroenie, Moscow, 1971).

5. V. E. Alemasov, A. F. Dregalin, and A. P. Tishin, *Theory of Rocket Engines*, Ed. by Yu. M. Davydov (Mashinostroenie, Moscow, 1980).

6. *Encyclopedia of Low-Temperature Plasma*, Ed. by V. E. Fortov (Nauka, Moscow, 2000), Introductory Volume IV.

7. Yu. M. Davydov and M. Yu. Egorov, *Numerical Simulation of Unsteady Transient Processes in Active and Reactive Engines* (National Academy of Applied Sciences of Russian Federation, Moscow, 1999).

8. Yu. M. Davydov, I. M. Davydova, and M. Yu. Egorov, *Refinement and Optimization of Aircraft and Rocket Engines with Allowance for Nonlinear Unsteady Gasdynamic Effects*, Ed. by Yu. M. Davydov (National Academy of Applied Sciences of Russian Federation, Moscow, 2002).

9. Yu. M. Davydov, in *Mathematical Encyclopedia* (Sov. Éntsiklopediya, Moscow, 1982), Vol. 3, p. 125.

10. Yu. M. Davydov, Dokl. Akad. Nauk SSSR **247**, 1346 (1979) [Sov. Phys. Dokl. **24**, 614 (1979)].

11. Yu. M. Davydov, I. M. Davydova, M. Yu. Egorov, A. M. Lipanov, *et al.*, *Numerical Investigation of Topical Problems of Mechanical Engineering and Mechanics of Continuous and Dry-Substance Flowing Media Using the Large Particle Method* (National Academy of Applied Sciences of Russian Federation, Moscow, 1995), Vols. 1 to 5.

12. R. I. Nigmatulin, *Foundations of Mechanics of Heterogeneous Media* (Nauka, Moscow, 1978).

13. Yu. M. Davydov, Zh. Vychisl. Mat. Mat. Fiz. **11** (4), 1056 (1971).

Translated by M. Lebedev

=========== **MECHANICS** ===========

On the Optimal Structure of the Arterial Wall

Academician S. N. Bagaev*, V. N. Zakharov*, A. L. Markel**, A. E. Medvedev***, V. A. Orlov*, V. I. Samsonov***, and Corresponding Member of the RAS V. M. Fomin***

Smooth-muscle elements of the wall of large arteries are known [1] to be located at an angle of 30°–50° to the vessel axis. As the diameter of arteries decreases, this angle increases to 90°. Here, we demonstrate that this arrangement of smooth muscles in the arterial wall is optimal for the durability of arteries through which blood permanently flows in pulses.

THE STRUCTURE OF BLOOD VESSELS

The wall of an artery or an arteriole may be regarded as a multilayer envelope or tunica (Fig. 1) consisting of three main layers: internal, middle, and external (tunica intima, tunica media, and tunica adventitia, respectively). Each of them, in turn, also has a complex multilayer structure. The middle layer (tunica media) contains numerous smooth-muscle cells, whose number and spatial arrangement depend on the type of the artery (elastic, muscular–elastic, or muscular). In general, smooth-muscle cells and elastic fibers form an integrated elastic-and-motor helix located at an angle to the vessel axis. Apparently, the slant position of smooth muscles in large arteries favors the rotational–translational movement of the blood [2].

THE MODEL OF A BLOOD VESSEL

Let us consider the wall of a blood vessel (Fig. 2) as a binding basis with muscle elements (reinforcing fibers) incorporated in it. In Fig. 2, L is the vessel length, h is the half-width of the vessel wall, and R is the vessel radius; the reinforcing muscle fibers are shown in gray.

---

* *Institute of Laser Physics, Siberian Division,*
 Russian Academy of Sciences,
 pr. Akademika Lavrent'eva 13/3, Novosibirsk,
 630090 Russia
** *Institute of Cytology and Genetics, Siberian Division,*
 Russian Academy of Sciences,
 pr. Akademika Lavrent'eva 10, Novosibirsk,
 630090 Russia
*** *Institute of Theoretical and Applied Mechanics,*
 Siberian Division, Russian Academy of Sciences,
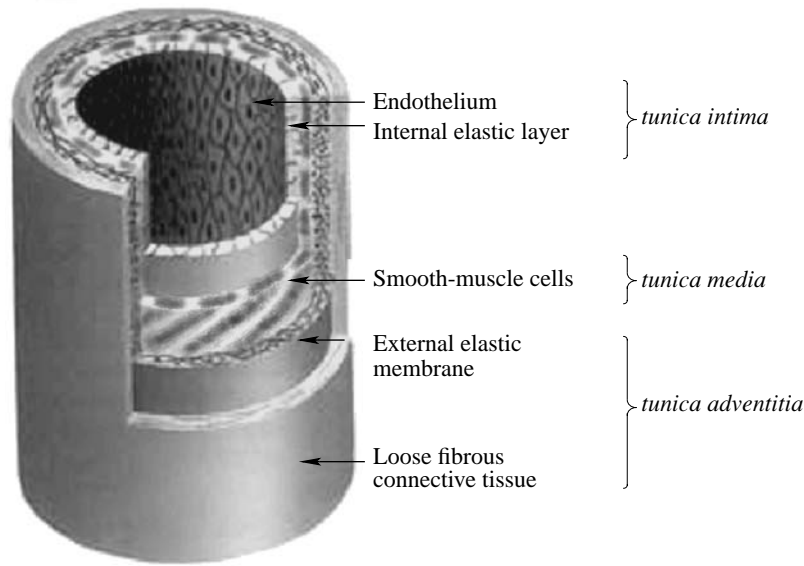 *ul. Institutskaya 4/1, Novosibirsk, 630090 Russia*

Let the volume proportion of the fibers be ω_s. The volume proportion of the binding base is then

$$\omega_0 = 1 - \omega_s. \tag{1}$$

The family of reinforcing fibers is located at an angle φ to the vessel axis (the dashed line in Fig. 2). Let us assume the reinforcing fibers to consist of an elastic material with Young's modulus E_s. It is also assumed that all fibers remain elastic at the loads specified. The binding base is assumed to consist of a linearly viscoelastic material with Young's modulus E_0 and Poisson's ratio ν. The following equation has been obtained [3] for the critical load (the maximum internal pressure that the vessel can resist):

$$\tilde{q} = \frac{\beta}{3}\varphi_1 + \frac{4\theta^4}{\beta\varphi_2}, \tag{2}$$

where

$$\varphi_1 = a_{11}\theta^2 + 2(a_{12} + 2a_{33}) + \frac{a_{22}}{\theta^2},$$

$$\varphi_2 = A_{22}\theta^2 + 2A_{12} + A_{33} + \frac{A_{11}}{\theta^2}.$$

Here, $\varepsilon = [a_{ij}]$ $(i, j = 1, 2, 3)$ is a symmetric matrix of the elasticity coefficients of the binding base and the fibers for a plane stress state.

In the case of an isotropic viscoelastic binding base, the coefficients of matrix ε have the form

$$a_{ii} = \frac{1}{1-\nu^2} + P_s\chi_i^4, \quad a_{12} = a_{21} = \frac{\nu}{1-\nu^2} + P_s\chi_1^2\chi_2^2,$$

$$a_{13} = a_{31} = P_s\chi_2\chi_1, \quad a_{23} = a_{32} = P_s\chi_1\chi_2, \tag{3}$$

$$a_{33} = \frac{1}{2(1+\nu)} + P_s\chi_1^2\chi_2^2,$$

Fig. 1. The scheme of the arterial-wall structure.

where $P_s = \dfrac{\omega_s \tilde{E}_s}{\omega_0}$, $\chi_i = $ const is the direction cosine of the fiber trajectory with respect to direction i. In the coordinate system shown in Fig. 2, the direction cosines are the following: $\chi_1 = \chi$, $\chi_2 = \sqrt{1-\chi^2}$, and $\chi_3 = 0$; here, $\chi = \cos\varphi$. The matrix $\|A_{ij}\| = \|a_{ij}\|^{-1}$ ($i, j = 1, 2, 3$). In Eqs. (2) and (3), dimensionless variables are used: $\tilde{q} = \dfrac{q}{(\omega_0 E_0 \tilde{h}^2)}$ (q is the dimensional internal pressure acting on the vessel); $\tilde{h} = \dfrac{h}{R}$; $\tilde{E}_s = \dfrac{E_s}{E_0}$; $\tilde{R} = \dfrac{R}{L}$ is the dimensionless radius of the vessel; $\beta = 2\tilde{h}\pi^2\tilde{R}^2$;

and $\theta = \dfrac{\pi\tilde{R}}{n}$. Here, n is the number of waves characterizing the form of vessel deformation. Hereinafter, we assume $n = 2$, which corresponds to the oval deformation of the vessel.

Equation (2) yields the maximum internal pressure that the vessel resists depending on the angle φ between the reinforcing fibers and the vessel axis. This dependence is shown in Fig. 3 (the values of the calculated parameters are indicated). As is seen from Fig. 3, the maximum pressure that the vessel resists corresponds to the angle of muscle-fiber arrangement $\varphi \approx 60°$.

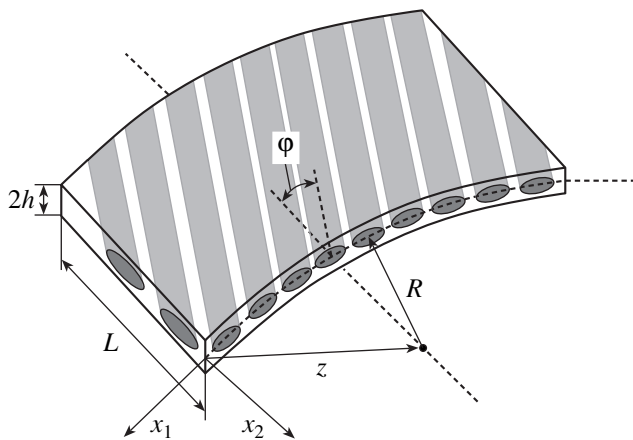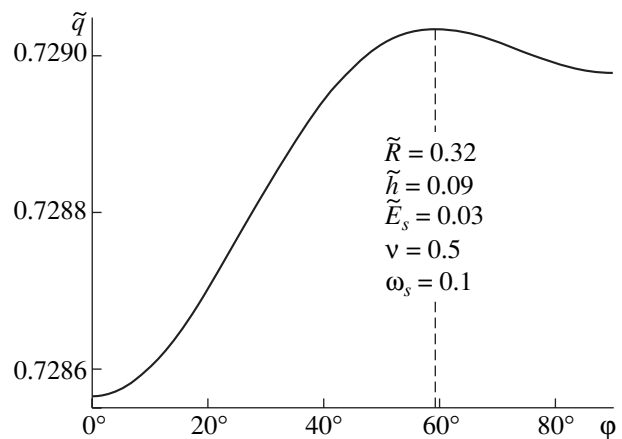**Fig. 2.** The model scheme of the blood-vessel wall.

Fig. 3. The dependence of the maximum internal pressure on the angle of the arrangement of muscle fibers.

$\tilde{R} = 0.32$
$\tilde{h} = 0.09$
$\tilde{E}_s = 0.03$
$\nu = 0.5$
$\omega_s = 0.1$

THE ELASTIC CHARACTERISTICS
OF BLOOD VESSELS

To analyze the characteristics of the arrangement of smooth-muscle elements, the elastic characteristics of blood vessels should be determined. The viscoelastic properties of arterial walls have been reviewed in detail in [1, 4].

According to [4], Poisson's ratio ν of vessel walls may be assumed to be 0.5 without causing much inaccuracy.

It was demonstrated previously [5] that the wall of the carotid artery of a dog resisted an internal pressure of $(88 \pm 10) \times 10^5$ Pa. When the muscular layer of this wall was studied separately (after the removal of the external and internal layers), it resisted a pressure as low as $(2.73 \pm 10) \times 10^5$ Pa. We now consider a homogeneous elastic cylindrical envelope exposed to internal pressure. The maximum pressure that the homogeneous envelope resists is [6]

$$q_{max} = \frac{\pi\sqrt{6}}{9(1-\nu^2)^{0.75}} E \frac{h^2}{RL} \sqrt{\frac{h}{R}}. \qquad (4)$$

To estimate the ratio between Young's moduli, $\tilde{E}_s = \frac{E_s}{E_0}$, we consider the ratio of the ultimate pressures for the muscular layer and the carotid artery. Then, according to Eq. (4), the ratio between Young's moduli of the reinforcing fibers (E_s) and the binding base (E_0) may be estimated as $\tilde{E}_s = 0.03$.

The ratio between the wall width and the radius of blood vessels is relatively constant [4]; therefore, the value $D = \dfrac{r_a - r_i}{r_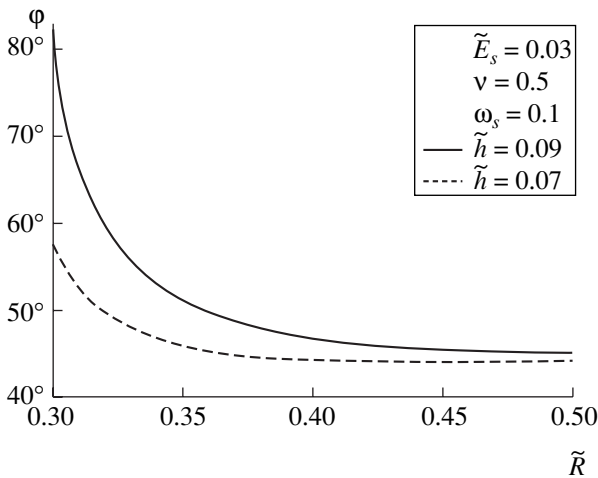i}$, where r_a and r_i are the external and internal radii of the artery, respectively, may be assumed to be constant without much inaccuracy. According to [4], $D = 0.15$ and $D = 0.20$ for arteries of the elastic and muscular types, respectively. Then, $\tilde{h}$ varies from 0.07 to 0.09 (for arteries of the elastic and muscular types, respectively).

The volume proportion of muscle fibers in the vessel wall (ω_s) is the most difficult to estimate. Obviously, this proportion depends on the artery type (elastic, muscular–elastic, or muscular). Here, we show the results for $\omega_s = 0.1$. The observed effect of the optimal angle of the muscle elements with respect to the vessel axis does not depend qualitatively on the volume proportion ω_s of muscle fibers.

THE OPTIMAL ARRANGEMENT
OF SMOOTH-MUSCLE FIBERS

The dependence of the internal pressure that the vessel resists on the angle at which muscle fibers are arranged is determined from Eq. (2). As is shown in Fig. 4, there is an optimum slope of the fibers at which pressure $\tilde{q}$ peaks. This dependence is determined by the equation

$$\frac{\partial \tilde{q}(\varphi; \tilde{R}, \tilde{E}_s, \nu, \omega_s, \tilde{h})}{\partial \varphi} = 0, \qquad (5)$$

from which we can find the optimum angle at which the fibers are arranged:

$$\varphi = \varphi(\tilde{R}; \tilde{E}_s, \nu, \omega_s, \tilde{h}). \qquad (6)$$

Figure 4 shows the plot for the optimum angle of muscle fibers (φ) versus vessel radius ($\tilde{R}$). As is seen from Fig. 4, in the case of large blood vessels ($\tilde{R} = 0.5$), the slope of muscle fibers is close to $43°$. As the vessel diameter decreases to $\tilde{R} = 0.3$, the angle of arrangement of muscle fibers increases to $83°$ and $58°$ for arteries of the muscular ($\tilde{h} = 0.09$) and elastic ($\tilde{h} = 0.07$) types, respectively. This dependence of the angle of arrangement of smooth-muscle elements corresponds to morphological data of [1] on the arrangement of muscles in arterial walls.

CONCLUSIONS

Thus, we have demonstrated that the spatial arrangement of smooth-muscle fibers in the walls of arteries and arterioles is optimal. Depending on the vessel size, muscle fibers are located in the arterial wall at the angle that ensures the maximum possible durability of the vessel. This confirms once more that the structure of living organisms (in the given case, their circu-

Fig. 4. The dependence of the optimum angle of the arrangement of muscle fibers on the blood-vessel radius.

latory system) also is optimal from the standpoint of mechanics.

ACKNOWLEDGMENTS

REFERENCES

1. *Physiology of Circulation: Physiology of the Vascular System*, Ed. by B. I. Tkachenko (Nauka, Leningrad, 1984).

2. V. N. Zakharov, S. N. Bagaev, and V. A. Orlov, in *Proceedings of World Congr. of World Society of Cardio-Thoracic Surgeons* (Cardiovascular Engineering, Vancouver, 2000), p. 102.

3. V. I. Samsonov, Prikl. Mekh. **13** (1), 107 (1982).

4. N. N. Savitskiǐ, *Biophysical Principles of Circulation and Clinical Methods for Studying Hemodynamics* (Medgiz, Leningrad, 1963).

5. Ph. Dobrin and A. Rovick, Am. J. Physiol. **217**, 1644 (1969).

6. A. S. Vol'mir, *Stability of Deformed Systems* (Nauka, Moscow, 1967).

Translated by V. Ushakov

===================== **MECHANICS** =====================

An Approach to Solving the Problems on Interaction between Elastic Bodies in the Presence of Adhesion

Academician I. G. Goryacheva and Yu. Yu. Makhovskaya

Received May 20, 2004

1. Present-day approaches to solving the problems on adhesion of elastic bodies can be divided into two classes. The first comprises numerical methods in which integral equations of the contact problem are solved numerically for a given form of the adhesion interaction potential (such as the Lennard-Jones potential [1]). The second presents approximate models (among them the classical Johnson–Kendall–Roberts theory and the classical Derjaguin–Müller–Toporov theory [2]) that yield asymptotic solutions to the adhesion problem in the case of two contacting elastic spheres. There are a number of approximate methods [3–5] developed for solving this problem in a wide range of changing problem parameters. These methods are based on the approximation by given functions of adhesion pressure arising on the surfaces of interacting bodies. In this study, we propose a more general approach using the representation of the adhesion pressure in the form of a piecewise-constant multistep function. This provides the possibility of considering arbitrary forms of the adhesion interaction potential (including the case of capillary adhesion), as well as of taking into account the presence of another additional load, in particular, the effect of neighboring asperities on adhesion of both rough bodies (Fig. 1) and bodies with a regular surface relief.

2. We consider the interaction between two axisymmetric elastic asperities (dashed-line circle domain in Fig. 1). The shape of their surfaces is described by a power function

$$f(r) = f_1(r) + f_2(r) = Ar^{2n},$$

where n is an integer. The boundary conditions at $z = 0$ have the form

$$u(r) = -f(r) - d, \quad 0 < r < a, \tag{1}$$

$$p(r) = -p_a(r), \quad a \le r \le b, \tag{2}$$

where $u(r) = u_1(r) + u_2(r)$ is the total normal displacement of the surfaces of the interacting bodies due to

their deformation, $p(r)$ is the pressure on the body surfaces, and d is the variable gap between two fixed points of the interacting bodies. These points are located on the symmetry axis of the bodies and are separated from the contact surface due to deformation of the bodies. From condition (1), it follows that the bodies are in contact over the circular domain $0 < r < a$. If the contact is absent ($a = 0$), this condition is ignored. Condition (2) implies that the surfaces are loaded by an additional pressure $-p_a(r)$ outside the contact area. This can be either adhesion pressure or an additional load of a different nature. In the section $a \le r \le b$, the function $p_a(r)$ is considered to be multiple step:

$$p_a(r) = \begin{cases} p_1, & b_0 \le r \le b_1, \\ p_2, & b_1 \le r < b_2, \\ \dots \\ p_N, & b_{N-1} \le r \le b_N, \end{cases} \tag{3}$$

where $b_0 = a$ and $b_N = b$.

The dependence of the normal displacement $u(r)$ on pressure $p(r)$ is determined by the well-known expression for axisymmetric loading of an elastic half-space [6]:

$$u(r) = A[p(r), b], \quad 0 \le r \le b,$$

$$A[p(r), c] = \frac{4}{\pi E^*} \int_0^c p(r') \mathbf{K}\left(\frac{2\sqrt{rr'}}{r+r'}\right) \frac{r'dr'}{r+r'}, \tag{4}$$

$$\frac{1}{E^*} = \frac{1-\nu_1^2}{E_1} + \frac{1-\nu_2^2}{E_2},$$

where E_i and ν_i ($i = 1, 2$) are the Young's moduli and

Institute for Problems in Mechanics,
Russian Academy of Sciences,
pr. Vernadskogo 101, Moscow, 119526 Russia
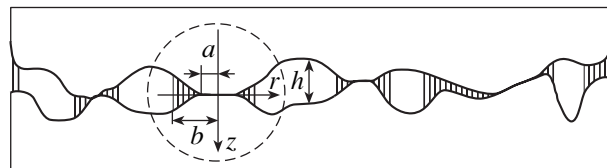*e-mail: goryache@ipmnet.ru; makhovskaya@ipmnet.ru*

Fig. 1. Adhesion interaction of two rough elastic bodies. The cross-hatched regions correspond to the adhesion attraction of the bodies' surfaces.

Poisson's ratios of the interacting bodies, respectively, and $\mathbf{K}(x)$ is the complete elliptic integral of the first kind.

In addition, the equilibrium condition

$$q = 2\pi \int_0^b r p(r) dr, \qquad (5)$$

(where q is the normal external force acting on a single asperity) should be fulfilled.

3. For $0 \leq r \leq a$, the function $p(r)$ is represented as

$$p(r) = p_*(r) - p_1. \qquad (6)$$

Using conditions (2) and (3), relationship (4) can be transformed into the form

$$u(r) - \sum_{k=1}^{N} (p_{k+1} - p_k)\chi(r, b_k) = A[p_*(r), a], \qquad (7)$$

where the function $\chi(r, c)$ is defined by the expression [7]

$$\chi(r, c) = A[1, c]$$

$$= \frac{4}{\pi E^*} \begin{cases} c\mathbf{E}\left(\dfrac{r}{c}\right), & r \leq c, \\ r\left[\mathbf{E}\left(\dfrac{c}{r}\right) - \left(1 - \dfrac{c^2}{r^2}\right)\mathbf{K}\left(\dfrac{c}{r}\right)\right], & r > c. \end{cases}$$

Here, $E(x)$ is the complete elliptic integral of the second kind. In (7) and hereinafter, it is assumed that $p_{N+1} = 0$.

In the absence of a contact between the surfaces ($a = 0$), relationship (7), in which the right-hand side is then equal to zero, is responsible for the elastic displacements of the surfaces $u(r)$ under the action of a given pressure $-p_a(r)$ (3) within the region $0 \leq r < b$.

When the surfaces are in contact, from (7) (with allowance for contacting condition (1)), we find the integral equation for determining the function $p_*(r)$:

$$A[p_*(r), a] = -f_*(r) - d, \quad r \leq a, \qquad (8)$$

$$f_*(r) = f(r) + \frac{4}{\pi E^*}\sum_{k=1}^{N}(p_{k+1} - p_k)b_k\mathbf{E}\left(\frac{r}{b_k}\right).$$

Then, taking into account (3) and (6), equilibrium condition (5) takes the form

$$q + \pi a^2 p_1 + \pi\sum_{k=1}^{N} p_k(b_k^2 - b_{k-1}^2) \quad 2\pi\int_0^a r p_*(r) dr. \qquad (9)$$

Since $p_*(a) = 0$ [in view of (6)], integral equation (8) is similar to that in the problem on indenting an axisymmetric stamp of a given shape $f_*(r)$ into an elastic half-space under the action of a force described by the expression on the left-hand side of condition (9). In this

case, for $a < r \leq b$, the right-hand side of relationship (7) defines the elastic displacements $u(r)$ outside the contact area. Solving this problem with the use of the series-expansion method described in [8] yields the following expressions for the contact pressure and boundary displacements of interacting bodies:

$$p(r) = \frac{AE^* a^{2n-1}}{\pi}\left[\frac{(2n)!!}{(2n-1)!!}\right]^2\sqrt{1 - \frac{r^2}{a^2}}$$

$$\times \sum_{k=1}^{n}\frac{(2k-3)!!}{(2k-2)!!}\left(\frac{r}{a}\right)^{2(n-k)} - p_1 - \frac{2}{\pi}\sum_{k=1}^{N}(p_{k+1} - p_k)$$

$$\times \arctan\sqrt{\frac{a^2 - r^2}{b_k^2 - a^2}}, \quad r \leq a, \qquad (10)$$

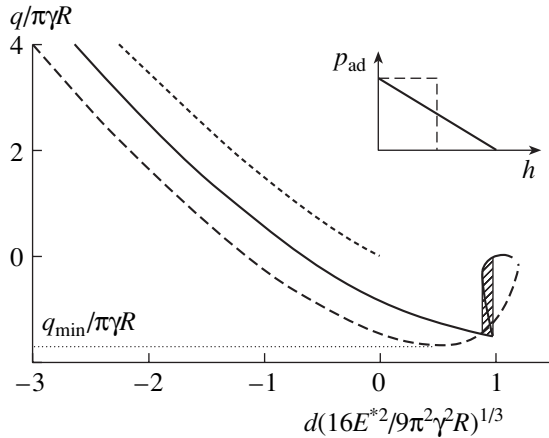$$u(r) = -\frac{2}{\pi}(d + Ar^{2n})\arcsin\frac{a}{r} + \frac{2Ar^{2n}}{\pi}\sqrt{\frac{r^2}{a^2} - 1}$$

$$\times \sum_{i=1}^{n}\frac{(2i-2)!!}{(2i-1)!!}\left(\frac{a}{r}\right)^{2i} - \frac{4}{\pi E^*}\sum_{j=1}^{k}(p_{j+1} - p_j)r\left\{\mathbf{E}\left(\frac{b_j}{r}\right)\right.$$

$$-\mathbf{E}\left(\arcsin\frac{a}{b_j}, \frac{b_j}{r}\right) - \left(1 - \frac{b_j^2}{r^2}\right)\left[\mathbf{K}\left(\frac{b_j}{r}\right)\right.$$

$$\left.\left.-\mathbf{F}\left(\arcsin\frac{a}{b_j}, \frac{b_j}{r}\right)\right]\right\} + \frac{4}{\pi E^*}\sum_{j=k+1}^{N}(p_{j+1} - p_j)b_j$$

$$\times\left[\mathbf{E}\left(\frac{r}{b_j}\right) - \mathbf{E}\left(\arcsin\frac{a}{r}, \frac{r}{b_j}\right)\right], \qquad (11)$$

$$b_k \leq r \leq b_{k+1}.$$

The distance between the bodies is given by the expression

$$d = -\frac{(2n)!!}{(2n-1)!!}Aa^{2n}$$

$$-\frac{2}{E^*}\sum_{k=1}^{N}(p_{k+1} - p_k)b_k\sqrt{1 - \frac{a^2}{b_k^2}}, \qquad (12)$$

and the load q has the form

$$q = \frac{(2n)!!}{(2n+1)!!}4E^*Ana^{2n+1} - \pi p_1 a^2$$

$$-\pi\sum_{k=1}^{N} p_k(b_k^2 - b_{k-1}^2) - 2\sum_{k=1}^{N}(p_{k+1} - p_k)b_k^2$$

$$\times\left(\arcsin\frac{a}{b_k} - \frac{a}{b_k}\sqrt{1 - \frac{a^2}{b_k^2}}\right). \qquad (13)$$

Fig. 2. Dependence of the dimensionless load on the dimensionless distance between the bodies for linear (solid line) and step (dashed line) functions $p_{ad}(h)$ at $\lambda = 0.6$. The plots of the functions $p_{ad}(h)$ are presented in the upper right corner. The dotted curve is obtained according to the Hertz theory in the absence of adhesion.

The relationships obtained make it possible to solve the problems on the interaction of elastic bodies in the presence of adhesion of various nature.

4. An example of the application of the above approach is solving the problem on the interaction of two elastic asperities in the presence of the adhesion attraction given as a function of the distance between surfaces $p_{ad}(h)$. An example of such a dependence is the Lennard-Jones function describing the molecular interaction of surfaces. To solve this problem, we set a partition b_j ($j = 1, 2, ..., N$) of the region of the adhesion interaction $a \leq r \leq b$, the values of p_j being assumed to be unknown. Determining the elastic displacements $u(r)$ outside the contact area according to either relationship (7) (when the right-hand side is zero) in the absence of the contact or (11) in the presence of the contact, it is possible to express the value of the gap at the points b_j using the expression

$$h(r) = f(r) + u(r) + d. \qquad (14)$$

Then, the values of p_j are found from the system of equations

$$p_j = p_{ad}(h(b_{j-1})), \quad j = 1, 2, ..., N.$$

Additional equations for determining the coordinates a, b of the boundaries of the areas of contact and adhesion interaction are the continuity condition for pressure $p(a) = p_1$ at the boundary of the contact area (in the case of contact, when $a > 0$) and relationship (13) for an external load.

Figure 2 shows the calculation results for the external force q as a function of the distance d between the surfaces in the cases when the function $p_{ad}(h)$ represents a step function and a linear function, and the shape of interacting bodies is described by a parabolic

function $f(r) = \dfrac{r^2}{2R}$, i.e., $A = \dfrac{1}{2R}$, $n = 1$. The parameters of both functions $p_{ad}(h)$ under consideration are chosen in such a manner that the surface energies for both surfaces

$$\gamma = \int_0^\infty p_{ad}(h)dh,$$

and the values of adhesion pressure $p_{ad}(0) = p_0$ at the zero distance between the surfaces are equal to each other, respectively. We have used the parametrization proposed in [3] for which the solution depends on only the parameter

$$\lambda = p_0 \left(\dfrac{9R}{2\pi\gamma E^{*2}} \right)^{1/3}.$$

The results indicate that the shape of the function $p_{ad}(h)$ most significantly affects the character of the dependences obtained for negative (separating the bodies) forces q, especially in the absence of a contact between the surfaces. It is also seen that the dependence of the force q on the distance d is nonmonotonic and not uniquely defined. This implies that, if the surfaces move apart under a controlled force q, the contact break occurs in the case of a negative pull-off force corresponding to the minimum value of q on the plot. If the surfaces approach and move apart under a controlled distance d, then there is an energy loss corresponding to the cross-hatched area in Fig. 2. The calculations indicate that, in the case of the step function $p_{ad}(h)$, the energy loss always differs from zero at $\lambda > 0$. At the same time, the energy loss for the linear function $p_{ad}(h)$ takes place only for values of λ exceeding a certain quantity. Note that the calculation results for the dependence of the force q on the distance d for the step function of adhesion attraction $p_{ad}(h)$ coincide with the solution obtained in [3]. The detailed analysis of this case, including the calculation of the pull-off force q_{min} and energy loss Δw in the approach–separation cycle of elastic bodies with different shapes (for various values of n), was performed in [9].

5. One more example illustrating the application of the above method is the case of capillary adhesion, when surface films of a liquid are merged into menisci around the interacting asperities (Fig. 1). Suppose that two elastic asperities are in contact over a region $r < a$ and a meniscus occupies a region $a \leq r \leq b$. The liquid in the meniscus exerts a permanent negative pressure $-p_0$ on the surface of the asperities. This pressure is defined by the relation $p_0 \approx \dfrac{2\sigma}{h(b)}$, which follows from the Laplace formula under the assumption that the gap between the surfaces is small compared to the meniscus radius. Here, σ is the surface tension in the liquid.
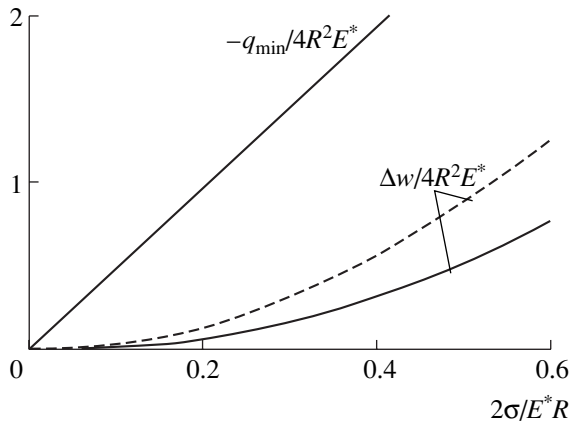
Fig. 3. Dimensionless pull-off force and dimensionless energy loss as functions of the dimensionless surface tension in the liquid in the case of capillary adhesion for $\dfrac{v}{R^3} = 0.40$ (solid line) and 0.08 (dashed line).

Fig. 4. Dependence of the dimensionless radius of the contact area on the dimensionless spacing between neighboring asperities in the case of the adhesion of surfaces with a regular relief; $\dfrac{\gamma}{RE^*} = 2 \times 10^{-4}$ and $\dfrac{p_0}{E^*} = 0.02$.

Imposing also the condition of the constant volume v of the liquid in the meniscus,

$$v = 2\pi \int_a^b rh(r)dr,$$

we arrive at the additional relation for determining the value of p_0.

The analysis of the solution to this problem presented in [8, 9] showed, in particular, that an approach and separation of elastic bodies in the presence of a meniscus is accompanied by an energy loss, as is the case for adhesion defined by the function of adhesion pressure $p_{ad}(h)$. For parabolic bodies ($n = 1$), the dependences of the energy loss Δw and the pull-off force q_{min}, on the surface tension in the liquid are shown in Fig. 3 (for different volumes of liquid in the meniscus). The results indicate that the greater the surface tension of liquid and the smaller the amount of liquid v, the greater the energy loss. The pull-off force depends virtually linearly on the surface tension and weakly depends on the volume of liquid in the meniscus.

6. The above method is also applicable for analyzing the adhesion interaction between elastic bodies with a regular surface relief. Suppose that an elastic half-space interacts with a periodic system of axisymmetric identical asperities whose shape is described by the function $f(r)$. The asperities are assumed to be situated at the sites of a hexagonal lattice with a step l. The boundary conditions in the neighborhood of each of the asperities correspond to the adhesion attraction of the surfaces with a given function $p_{ad}(h)$ or to the case that each asperity is surrounded by a meniscus of liquid.

To solve this problem, we used the localization method of [10]. In the simplest variant of this method,

only the interaction between the half-space and a single asperity in the presence of an additional load in the form of uniform pressure $\bar{p}$ acting within the region $L \leq r < +\infty$ is taken into account. The mean pressure is calculated by the formula $\bar{p} = \dfrac{2q}{\sqrt{3}l^2}$, and the value of L is found from the equality condition of the mean pressure inside and outside of the region $r \leq L$, i.e., $\bar{p} = \dfrac{q}{\pi L^2}$. As a result, we have to solve the axisymmetric problem for the half-space with boundary conditions similar to those described in Section 2, in which the region of loading by an additional step pressure $-p_a(r)$ is infinitely large: $a \leq r < +\infty$. The results of solving this problem for the step function of the adhesion attraction $p_{ad}(h)$ and $n = 1$ (parabolic asperities) are presented in [11].

Figure 4 shows the dependences of the contact-area radius a on the spacing l between the neighboring asperities at a fixed mean pressure $\bar{p}$ onto the half-space. The results indicate that, for the positive mean pressure $\bar{p}$, a decrease in the spacing l reduces the size of the contact area. On the contrary, for negative pressures, provided that the surfaces are still in contact, a decrease in l leads to increasing radius a of the contact area. This implies that the character of the dependence of the actual contact area on the localization density of the asperities on a rough surface is determined by the sign of the external nominal pressure applied to interacting bodies.

7. The approach developed makes it possible to solve the problems on interacting elastic bodies in the presence of different-type adhesion determined by the interaction potential of an arbitrary shape, including the

case of capillary adhesion. In addition, it turns out to be possible to investigate an effect of adhesion on the interaction between bodies with a regular surface relief.

The method described enables one to calculate contact pressures, the actual contact area, elastic displacements of surfaces, and other characteristics of the adhesion interaction depending on diverse parameters, such as the shape of the adhesion interaction potential, its characteristics (in particular, surface energy of bodies and liquid films covering them), the amount of liquid in gaps, elastic constants of the bodies, the shape of interacting asperities, and their localization density.

Analysis of the results obtained also makes it possible to study various effects intrinsic to the adhesion interaction of elastic bodies (energy loss as a result of surface approach–separation cycle, a phenomenon of the jump-like separation of surfaces, expanding the actual contact area with increasing density of surface asperities for negative values of an external force, etc.).

ACKNOWLEDGMENTS

REFERENCES

1. J. A. Greenwood, Proc. R. Soc. London Ser. A **453**, 1277 (1997).

2. D. Tabor, J. Colloid Interface Sci. **58**, 2 (1977).

3. D. Maugis, J. Colloid Interface Sci. **150**, 243 (1992).

4. J. A. Greenwood and K. L. Johnson, J. Phys. D: Appl. Phys. **31**, 3279 (1998).

5. E. Barthel, J. Colloid Interface Sci. **200**, 7 (1998).

6. L. A. Galin, *Contact Problems in Theory of Elasticity and Viscoelasticity* (Nauka, Moscow, 1980).

7. K. L. Johnson, *Contact Mechanics* (Cambridge University Press, Cambridge, 1985; Mir, Moscow, 1989).

8. I. G. Goryacheva and Yu. Yu. Makhovskaya, Prikl. Mat. Mekh. **63**, 128 (1999).

9. I. G. Goryacheva and Yu. Yu. Makhovskaya, Prikl. Mat. Mekh. **65**, 279 (2001).

10. I. G. Goryacheva, Prikl. Mat. Mekh. **62**, 1036 (1998).

11. Yu. Yu. Makhovskaya, Izv. Ross. Akad. Nauk: Mekh. Tverd. Tela, No. 2, 49 (2003).

Translated by Yu. Vishnyakov

<center>═══════════ MECHANICS ═══════════</center>

On Particle's Trajectories of Moon-to-Earth Space Flights with the Gravitational Escape from the Lunar Attraction

V. V. Ivashkin

Presented by Academician T. M. Éneev May 18, 2004

Received May 21, 2004

Investigations of space trajectories for flights from the immediate vicinity of the Moon to the Earth are important for both celestial mechanics and astronautics. Usual trajectories (see, e.g., [1]) for direct Moon-to-Earth space flights within the Earth's sphere of influence with respect to the Sun are well studied. In this case, perturbations caused by the Sun are small, and the model of a restricted three-body problem (Moon, Earth, and a particle of negligible mass) is used in practice. Trajectories of this type were employed for space flights from the Moon (in both the USA project of the manned Apollo flight and the Soviet project of automatic capture of the lunar matter and its delivery to the Earth [2]). These trajectories are characterized by small (several days) flight time and by the fact that the departure of a particle from the Moon occurs along a hyperbola. Recently [3–7], a new class of trajectories of indirect detour Moon-to-Earth space flight was discovered in the framework of the four-body system (Earth–Moon–Sun–particle). These trajectories initially use space flights towards the Sun (or away from the Sun) beyond the sphere of the Earth's influence, and only afterwards, space flights towards the Moon. These space flights are similar to bielliptic ones proposed by Sternfeld [8] but differ in their dynamics. Here, the perigee distance rises due to the Sun's gravitation. In addition, a particle flies up to the Moon along an elliptic trajectory, i.e., the capture by the Moon takes place. Thus, for the spacecraft capture to a lunar-satellite orbit or for its landing onto the Moon, these detour space flights are more profitable than direct, or bielliptic ones. An idea arises to employ this detour scheme for Moon-to-Earth space flights [4].

The present paper describes basic conclusions of numerical and analytical studies of the given problem. As a result, a family of trajectories for passive space flight to the Earth from an elliptic orbit of a lunar satellite have been constructed, and characteristics of these

Keldysh Institute of Applied Mathematics,
Russian Academy of Sciences,
Miusskaya pl. 4, Moscow, 125047 Russia
e-mail: ivashkin@spp.Keldysh.ru

trajectories are analyzed. In addition, an effect of gravitational perturbations resulted in the formation of given trajectories, particularly, in both the particle's gravitational escape from the lunar attraction and passive lowering of the perigee distance of a particle's orbit (from the value of the lunar radius to almost zero), which makes possible passive flights of a particle to the Earth, has been analyzed.

As a result of this analysis and with regard to the experience of the Earth-to-Moon trajectory studies [7], a numerical algorithm has been obtained that has allowed us to find a family of detour trajectories for space flights to the Earth from an elliptic orbit of a lunar satellite. The trajectories correspond to the spacecraft start from both the Moon's surface and the low orbit of a Moon satellite for several positions of the Moon in its orbit. The spacecraft trajectories are determined by integration (using the method described in [9]) of equations for particle motion. The equations are written in the Cartesian irrotational geocentric-equatorial orthogonal $OXYZ$ coordinate system in the attraction field of the Earth (with regard to its c_{20} main harmonic), the Moon, and the Sun with the high-precision determination of the lunar and solar coordinates, which is based on the DE403 JPL ephemerides. Particle motion in the $MXYZ$ selenocentric coordinate system is also determined. Characteristics of a typical detour trajectory are presented in Figs. 1–3. The solid curve in Fig. 1 presents geocentric motion of a spacecraft, whereas the dashed-dotted curve shows the lunar orbit M. At the point D, the spacecraft flies away from the Moon on May 11, 2001 (for the position of the Moon near the apogee), from the perilune of an initial elliptic orbit with the perilune altitude $H_{\pi 0} = 100$ km and semimajor axis $a_0 = 38\,455$ km. This orbit is close to the final orbit of the Earth-to-Moon space flight, which was presented in [7]. All further motions of the particle are passive (without allowance for possible corrections). Under the effect of the Earth's gravitation, the orbit evolution and

an increase in the selenocentric energy $E_s = \dfrac{V^2}{2} - \dfrac{\mu_M}{\rho}$

occur, where V and ρ are the velocity of the particle and its distance from the Moon, respectively, and $\mu_M \approx$
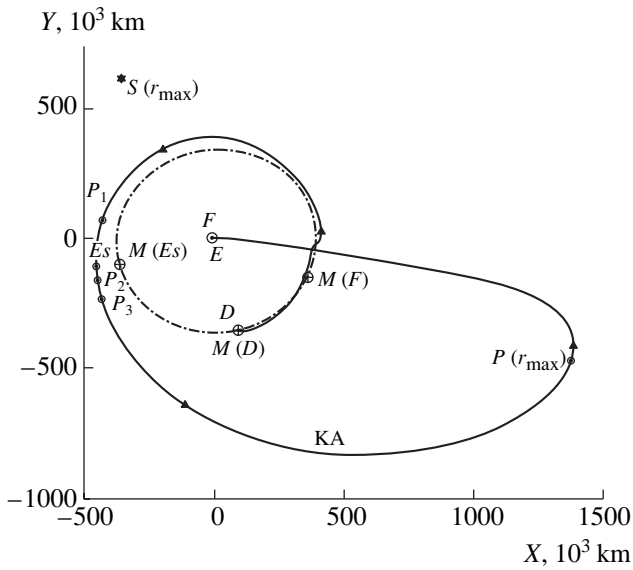
Fig. 1. Geocentric trajectory of detour Moon-to-Earth space flight (*XY* projection).
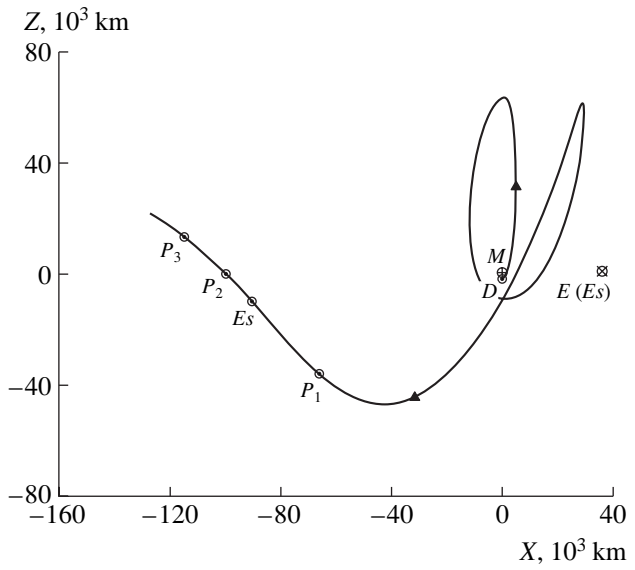

Fig. 2. Selenocentric trajectory of detour Moon-to-Earth space flight at the initial stage of motion with the escape from lunar gravitational attraction (*XZ* projection).

4902 km^3 s^{-2} is the lunar gravitational parameter. At the point P_1 for the space flight time $\Delta t \approx 19$ days, the energy is $E_s \approx -0.031$ km^2 s^{-2}, $a \approx 79 \times 10^3$ km, and $\rho \approx 76 \times 10^3$ km. At the point Es for $\Delta t \approx 20.6$ days and $\rho \approx 91.85 \times 10^3$ km, in the region of the translunar libration point L_2, the escape from the lunar attraction occurs, i.e., $E_s = 0$, and the orbit is parabolic with the zero velocity at infinity, $V_\infty = 0$. Furthermore, space flight from the Moon proceeds along a hyperbola. At the point P_2 for $\Delta t \approx 21.1$ days and $\rho \approx 101 \times 10^3$ km, the energy is $E_s \approx 0.011$ km^2 s^{-2}, $V_\infty = 0.15$ km s^{-1}. At the point P_3 for $\Delta t \approx 21.9$ days and $\rho \approx 120.2 \times 10^3$ km, the energy becomes equal to $E_s \approx -0.031$ km^2 s^{-2} and $V_\infty = 0.25$ km s^{-1}. Then, the spacecraft flies away from both the lunar orbit and the Earth and for $\Delta t \approx 70$ days reaches the maximal distance $r_{max} \approx 1.47 \times 10^6$ km from the Earth. At that instant of time, the point S determines the direction to the Sun. Under the action of the Sun, the perigee gradually lowers, and for $\Delta t \approx 113$ days at the point F, the spacecraft approaches the Earth E having the osculating (before the Earth's atmosphere) perigee altitude $H_\pi = 50$ km. Figures 2 and 3 show the evolution of spacecraft motion with respect to the Moon at the initial stage of the space flight. The point E (E_s) determines the direction to the Earth at the moment of the escape from the lunar gravitational attraction. The initial (at the point D) spacecraft velocity is $V_0^- \approx 2282$ m s^{-1}. Upon leaving a circular lunar-satellite orbit with an altitude of 100 km ($V_0^- \approx 1633$ m s^{-1}), the velocity increment is $\Delta V_0 \approx 649$ m s^{-1}. For the usual direct space-flight scheme and the minimal departure energy, $V_\infty \approx$

0.8 km s^{-1}, for the flight time $T \approx 5.5$ days, we have $V_0^+ \approx 2443$ m s^{-1}, $\Delta V_0 \approx 810$ m s^{-1}, which is ~161 m s^{-1} higher than in the case of the detour space flight. For a spacecraft leaving the Moon's surface, the detour trajectory is very close to the indicated one and the decrease in the velocity increment is equal to ~156 m s^{-1}.

We now qualitatively analyze the gravitational effect on the formation of a detour trajectory. First, we
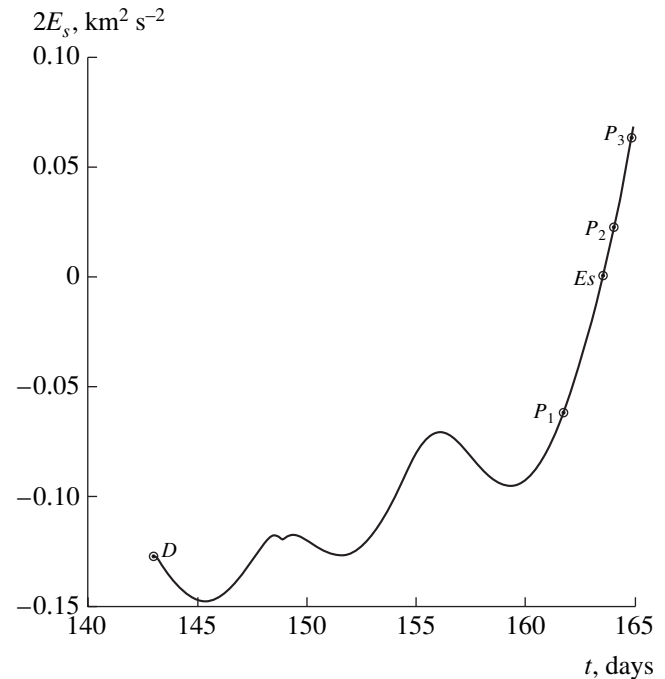
Fig. 3. Time variation of the selenocentric energy constant at the initial stage of space flight from the Moon with the escape from the lunar gravitational attraction.

estimate how the Earth affects an energy increase $\Delta E_s = -E_0$ with respect to the Moon from the negative value E_0 (for the initial elliptic orbit) to the zero energy (in the arc $D\,Es$) in the process of particle motion. Based on the orbit evolution theory [10] and assuming that the eccentricity is $e \approx 1$, the mean energy is $E_s \approx -\dfrac{\Delta E_s}{2}$. Taking into account the change in the Moon–Earth direction of motion, we obtain [7]

$$\Delta E_s \approx \operatorname{sgn}\beta \left(\frac{15}{2}\pi\mu_E \left(\frac{\mu_M}{a_M}\right)^3 n_M \beta \right)^{2/9} > 0. \qquad (1)$$

Here, μ_E is the Earth's gravitational parameter, a_M is the semimajor axis of the Moon's orbit, n_M is the angular velocity of Moon's orbital motion, $\beta = \cos^2\gamma\sin 2\alpha$, γ is the slope of the radius vector $\mathbf{r}_B$ of an external body (in the given case, of the Earth) to the plane of the particle orbit, and α is the angle between the projection of the radius vector onto this plane and the direction to the pericenter (here, perilune). For $\Delta E_s > 0$, we have $\sin 2\alpha > 0$, $0 < \alpha < \pi/2$ or $\pi < \alpha < \dfrac{3\pi}{2}$. From estimate (1), we arrive at $\Delta E_s \sim 0.09$ km^2 s^{-2} for $\beta = 0.5$, which is qualitatively consistent with the results of our numerical calculations. We can see that, in the case of an appropriate orientation of the Earth and initially rather prolate elliptic orbit of the lunar satellite, the Earth's gravitation provides a sufficient increase in the particle energy and allows the passive escape from the lunar attraction.

The acceleration of particle motion with respect to the Moon (from the zero energy to the hyperbolic one) with V_∞ of about 0.2–0.3 km s^{-1} in the subsequent short arc $Es\,P_2P_3$ (even in the somewhat larger arc P_1P_3 from the energy $E_s < 0$) is qualitatively described by the approximate model of one-dimensional rectilinear particle motion, the Earth being localized on the same line at a distance r_M beyond the Moon [7]. In the given case, $\dfrac{d\rho}{dt} > 0$, i.e., the particle moves away from the Moon.

The Earth's perturbation $a_E = \dfrac{\mu_E}{r_M^2} - \dfrac{\mu_E}{(r_M + \rho)^2} > 0$ accelerates particle motion. In the framework of this model, and assuming that, approximately, $r_M = \mathrm{const}$, we can integrate the equation for the perturbed motion of a particle:

$$E_s(\rho) - E_0 = \frac{\mu_E}{r_M^2}(\rho - \rho_0) + \frac{\mu_E}{r_M + \rho} - \frac{\mu_E}{r_M + \rho_0}, \qquad (2)$$

$$E_s(\rho_0) = E_0;$$

$$\rho = \frac{B}{2} + \left[\frac{B^2}{4} + r_M B \right]^{1/2},$$

$$B = \frac{(E_s - E_0)r_M^2}{\mu_E} + \frac{\rho_0^2}{r_M + \rho_0}; \qquad (3)$$

$$V^2(\rho) = 2E_s(\rho) + \frac{2\mu_M}{\rho}, \quad t - t_0 = \int_{\rho_0}^{\rho} \frac{d\rho}{V(\rho)}. \qquad (4)$$

Example. Let for a given trajectory at the point Es of the gravitational escape, $E_s = E_0 = 0$, $\rho = \rho_0 = 91850$ km, $r_M = 376000$ km. Then, model (2)–(4) yields $\rho \approx 102.5 \times 10^3$ km at $V_\infty = 0.15$ km/s (point P_2), $\rho \approx 120.4 \times 10^3$ km at $V_\infty = 0.25$ km s^{-1} (point P_3), and $\rho \approx 55 \times 10^3$ km for $E_s = -0.031$ km^2 s^{-2} (point P_1). We can see the qualitative correspondence with the numerical results presented above, especially for $E_s > 0$.

Thus, for the given class of space flights, the Earth's gravitation in the region of the translunar libration point L_2 allows the energy of selenocentric particle motion to be increased from the zero value to that characteristic of motion along a hyperbolic trajectory. Afterwards, the particle moves away from the Earth at a large distance.

Next, we estimate the effect of the Sun on the variation Δr_π of the particle orbit perigee distance r_π in the final space-flight arc $\sim P_3F$. Assuming the Sun to be immobile, we apply the orbit evolution theory for one orbital revolution of a planet satellite under the action of an exterior body [10]. Since the final distance in the perigee is very small ($r_{\pi f} \ll r_{\pi 0} \approx -\Delta r_\pi$), we assume $e \approx 1$ and take for r_π its mean value, namely, $r_\pi = \dfrac{2r_{\pi f} - \Delta r_\pi}{2} \approx -\dfrac{\Delta r_\pi}{2}$. Thus, we arrive at

$$\Delta r_\pi \approx \operatorname{sgn}\beta \left(\frac{15}{2}\pi\frac{\mu_S}{\mu_E}\beta \right)^2 \frac{a^7}{a_E^6} < 0. \qquad (5)$$

Here, μ_S is the gravitational parameter of the Sun, a_E is the semimajor axis of the Earth's orbit, and the quantity β is determined by the Sun as by an external body. For $\Delta r_\pi < 0$, it follows that $\sin 2\alpha < 0$, $\dfrac{\pi}{2} < \alpha < \pi$ or $\dfrac{3\pi}{2} < \alpha < 2\pi$. Then, we estimate the desired value of the semimajor axis for the spacecraft orbit as

$$a \approx \left[\frac{|\Delta r_\pi| a_E^6}{\left(\dfrac{15}{2}\pi\dfrac{\mu_S}{\mu_E}\beta \right)^2} \right]^{1/7} \qquad (6)$$

In this estimate, we have assumed that $\Delta r_\pi = -500 \times 10^3$ km and $\beta = -0.5$. Then, a is approximately 870×10^3 km and the apogee distance is $r_\alpha \approx 1500 \times 10^3$ km. The allowance for the variable direction to the Sun only slightly affects the final result. Thus, in the case of an appropriate orientation of the Sun, moving off to a distance of $\sim 1500 \times 10^3$ km results in lowering of the particle orbit perigee from the lunar-orbit radius to almost zero and allows passive approach to the Earth.

Reviewing the results of our analysis, we can see that gravitational perturbations of the Earth and Sun make it possible to escape the particle motion from the lunar attraction, to transfer to a detour trajectory, and then to approach the Earth. This leads to noticeable decrease in the energy consumption for Moon-to-Earth space flights. Such a conclusion is confirmed by the numerical calculations of relevant trajectories.

ACKNOWLEDGMENTS

REFERENCES

1. V. A. Egorov and L. I. Gusev, *Dynamics of Earth-to-Moon Space Flights* (Nauka, Moscow, 1980).

2. K. Gatland, *The Illustrated Encyclopedia of Space Technology* (Salamander Book Ltd., London, 1982; Mir, Moscow, 1986).

3. E. A. Belbruno and J. K. Miller, Guidance, Control, and Dyn. **16**, 770 (1993).

4. H. Yamakawa, J. Kawagushi, N. Ishii, *et al.*, in *Proceedings of AAS//AIAA Astrodynamics Special Conf., Victoria, 1993,* AAS 93-633.

5. M. Bello Mora, F. Graziani, P. Tiofilatto, *et al.*, in *Proceedings of 51st Int. Astronautical Congress, Rio de Janeiro, 2000*, IAF-00-A.6.03.

6. W. S. Koon, M. W. Lo, J. E. Marsden, *et al.*, Celest. Mech. Dyn. Astron. **81**, 63 (2001).

7. V. V. Ivashkin, Dokl. Akad. Nauk **387**, 196 (2002) [Dokl. Phys. **47**, 825 (2002)].

8. A. Sternfeld, C. R. Acad. Sci. **198**, 711 (1934).

9. V. A. Stepan'yants and D. V. L'vov, Mat. Model. **12** (6), 9 (2000).

10. M. L. Lidov, Artificial Earth's Satellites, No. 8, 5 (1961).

Translated by G. Merzon

===== **MECHANICS** =====

A Model of the Helical Pulsed Flow of Blood in Arteries

Yu. A. Ustinov

Presented by Academician V.A. Babeshko September 16, 2003

Received August 8, 2003

On a number of websites (listed at the end of the paper), the discovery of the formation of the helical flow of blood in the cardiovascular system of human beings and animals is announced. In particular, in the informative report "New in the Biomechanics of Blood Circulation" by S.N. Bagaev, V.N. Zakharov, and V.A. Orlov working at the Institute of Laser Physics, Siberian Division, Russian Academy of Sciences (RAS), Novosibirsk, reported that they discovered the formation of the helical flow of blood in the cardiovascular system of human beings and animals: blood circulation is accompanied by the formation of the rotational–translational flow of blood in the heart and blood vessels that is caused by the helical orientation of the muscular elements of the heart and blood vessels. In the General Meeting of the Siberian Division of the RAS, April 24, 2003, Academician N. Dobretsov, Chairman of the Siberian Division of the RAS, reported:

> Investigations carried out at the Institute of Laser Physics, Siberian Division, RAS, Novosibirsk; the Institute of Theoretical and Applied Mechanics, Siberian Division, RAS, Novosibirsk; and the Institute of Cytology and Genetics, Siberian Division, RAS, Novosibirsk, showed that the helical flow of biological media exists in the cardiovascular and other transport systems of the organism. This flow is based on the interaction of transport channel walls with a medium due to a twisting wave generated by a helix and muscular elements.

It is worth noting that the formation of the helical flow in the heart due to both its geometric shape and the mechanical structure of the myocardium was indicated already in [1] (the referee called my attention to this work). A model based on the working principles of various pumps was proposed in that work.

Causes of the helical flow of blood in vessels can be different. In particular, various results showing that the rotational velocity component with respect to the vessel axis can arise in sections where an artery has curvature

were reviewed in [2]. In arteries directly connected with the heart, the helical flow can be caused by a vortex flow in the heart, which arises during systole.

In the present paper, a model is proposed in which the wall of a blood vessel is considered as an elastic shell with helical anisotropy and blood is treated as a viscous fluid. The helical pulsed flow of blood described in the above citations can be mathematically reproduced (at least, qualitatively) in this model. Similar models disregarding the helical anisotropy of the wall, as well as detailed bibliography, were described in [2].

STRUCTURE OF THE ARTERIAL WALLS

According to extensive experimental data [2, 3], the walls of arteries can be treated as multilayer anisotropic shells. According to [2], the walls of all arteries have a similar structure and consist of the same materials. The relations between materials in the walls of vessels in different sections of the circulation system are different. A wall is traditionally divided into three layers: inner (tunica intima), medium (tunica media), and outer (tunica adventitia). It is commonly accepted that the tunica intima and tunica adventitia slightly affect the mechanical properties of the wall. The elastic properties of the shell are determined by the tunica media, which has different structures in large and small arteries. In large arteries, it consists of many layers of elastic tissue, including elastin and muscular tissue that are braided with very thin collagen fibers. Cavities between layers are filled with various spongy tissues and liquid. In small arteries, the tunica media almost completely consists of spirally arranged smooth-muscular cells also located as layers with small amount of collagen and elastin [2]. Elastin, collagen, and muscular tissue form about half the material of the wall. As was mentioned in [3], the mechanical properties of specific vessels change with age.

Thus, the material of the wall can be treated as a fiber composite whose elastic properties are determined by its components and their concentrations.

Rostov State University,
ul. Zorge 5, Rostov-on-Don, 344104 Russia
e-mail: ustinov@math.rsu.ru

BASIC RELATIONS OF SHELL THEORY WITH HELICAL ANISOTROPY

In the proposed model, a vessel is treated as a circular cylindrical shell with thickness h, middle-surface radius a and density of the vessel-wall material ρ_0, and blood is treated as a viscous incompressible fluid with kinematic viscosity ν and density ρ. The problem is axisymmetric. The basic relations describing the dynamic stress–strain state of the vessel wall are constructed by using the momentless theory of shells.

The origin of the Cartesian coordinate system (x_1, x_2, x_3) is related to a vessel cross section. This coordinate system is called basic. The accompanying coordinate system (r, θ, z) is related to the basic coordinate system as

$$x_1 = r\cos(\theta + \tau z), \quad x_2 = r\sin(\theta + \tau z), \quad x_3 = z, \quad (1)$$

where $\tau = \text{const}$.

Relations (1) with $r = \text{const}$ and $\theta = \text{const}$ are parametric equations of a helix (geometric image of a muscular fiber), where $\tau = \dfrac{\tan\alpha}{a}$ and α is the angle between the tangent to the helix and the vessel axis.

The material of the vessel wall is treated as transversally isotropic with the principal axes of the elastic-property tensor that are directed along the unit vectors $\mathbf{e}_1$, $\mathbf{e}_2$, and $\mathbf{e}_3$ of the principal normal, binormal, and tangent to the helix, respectively. In this case, strains and stresses are related as [4]

$$e_j = a_{ij}\sigma_i, \quad a_{ji} = a_{ij}, \quad i, j = 1, 2, \ldots, 6,$$

$$a_{11} = a_{22} = \frac{1}{E_1}, \quad a_{33} = \frac{1}{E_3}, \quad a_{12} = -\frac{\nu_1}{E_1},$$

$$a_{13} = a_{23} = -\frac{\nu_3}{E_3},$$

$$a_{44} = a_{55} = \frac{1}{G}, \quad a_{66} = \frac{1}{2E_1(1 + \nu_1)},$$

$$\sigma_1 = \sigma_{11}, \quad \sigma_2 = \sigma_{22}, \quad \sigma_3 = \sigma_{33},$$

$$\sigma_4 = \sigma_{23}, \quad \sigma_5 = \sigma_{13}, \quad \sigma_6 = \sigma_{12}.$$

The relations of generalized Hooke's law in the cylindrical coordinate system can be obtained by means of known linear transformations [4–7].

In classical shell theory, it is assumed that $\sigma_{rr} = \sigma_{r\theta} = \sigma_{rz} = 0$. These assumptions make it possible to obtain the following expressions related strains and stresses in the middle surface of the shell:

$$e_{zz} = g_{11}T_{zz} + g_{12}T_{\theta\theta} + g_{13}T_{z\theta},$$
$$e_{\theta\theta} = g_{12}T_{zz} + g_{22}T_{\theta\theta} + g_{23}T_{z\theta}, \quad (2)$$
$$e_{\theta z} = g_{13}T_{zz} + g_{23}T_{\theta\theta} + g_{33}T_{z\theta};$$

$$g_{11} = \frac{1}{hg^4}\left[\frac{1}{E_1} - x^2\left(\frac{2\nu_3}{E_3} - \frac{1}{G}\right) + \frac{x^4}{E_3}\right],$$

$$g_{12} = \frac{1}{hg^4}\left[\frac{1 - \nu_1}{E_1} + x^2\left(\frac{1 - \nu_3}{E_3} - \frac{1}{G}\right)\right],$$

$$g_{22} = \frac{1}{hg^4}\left[\frac{1}{E_3} - x^2\left(\frac{2\nu_3}{E_3} - \frac{1}{G}\right) + \frac{x^4}{E_1}\right],$$

$$g_{13} = -\frac{x}{hg^4}\left[\frac{2(1 + \nu_1)}{E_1} - \frac{1}{G} + x^2\left(\frac{2(1 + \nu_3)}{E_3} - \frac{1}{G}\right)\right], \quad (3)$$

$$g_{23} = \frac{x}{hg^4}\left[\frac{2(1 + \nu_3)}{E_3} - \frac{1}{G} - x^2\left(\frac{2(1 + \nu_3)}{E_3} - \frac{1}{G}\right)\right],$$

$$g_{33} = \frac{1}{hg^4}\left[\frac{(1 - x^2)^2}{G} + 4x^2\left(\frac{1 + \nu_1}{E_1} + \frac{1 + \nu_3}{E_3}\right)\right],$$

$$g = (1 + x^2)^{1/2}, \quad x = a\tau = \tan\alpha.$$

In the case under consideration, all field characteristics depend only on z and t. Therefore, strains and equations of motion take the form

$$e_{\theta\theta} = \frac{u_r}{a}, \quad e_{zz} = \partial u_z, \quad 2e_{z\theta} = \partial u_\theta; \quad (4)$$

$$-\frac{T_{\theta\theta}}{a} - h\rho_0\partial^2 u_r + q_r = 0, \quad \partial T_{zz} - h\rho_0\partial^2 u_z + q_z = 0,$$

$$\partial T_{\theta z} - h\rho_0\partial^2 u_\theta + q_\theta = 0, \quad (5)$$

$$\partial_r = \frac{\partial}{\partial r}, \quad \partial_z = \frac{\partial}{\partial z}, \quad \partial_t = \frac{\partial}{\partial t}.$$

Here, q_r, q_z, and q_θ are external stresses transferred to the middle surface of the vessel wall.

CONSTRUCTION OF THE SOLUTION DESCRIBING THE JOINT MOTION OF THE VESSEL WALL AND BLOOD

We now describe the joint motion of the vessel wall and blood by the above equations of the momentless theory of shells, Navier–Stokes equations, and incom-

pressibility equation [8]. We assume that the kinematic no-slip conditions

$$\partial_t u_r = v_r, \quad \partial_t u_z = v_z, \quad \partial_t u_\theta = v_\theta, \qquad (6)$$

are satisfied on the vessel wall, and the hydrodynamic action on the vessel wall is expressed by the relations

$$q_r = [p - 2\rho\nu\partial_r v_r]_{r=a}, \quad q_z = -\rho\nu[\partial_r v_z + \partial_z v_r]_{r=a},$$

$$q_\theta = -\rho\nu\left[\partial_r v_\theta - \frac{r v_\theta}{r}\right]_{r=a}. \qquad (7)$$

Here, v_r, v_z, and v_θ are the radial, axial, and circular velocity components, respectively, and p is pressure.

A solution is sought in the form

$$u_j = U_j e^{i(k\zeta - \omega t)}, \quad v_j = V_j(\xi) e^{i(k\zeta - \omega t)},$$

$$p = p_0 e^{i(k\zeta - \omega t)}, \quad \xi = \frac{r}{a}, \quad \zeta = \frac{z}{a}. \qquad (8)$$

Here, U_j, where $j = r$, z, and θ, are arbitrary constants.

Solving hydrodynamical equations under the assumption that $\partial_r p = 0$, we obtain

$$V_z = \frac{jka}{\rho\nu\beta^2}p_0 + \frac{J_0(\beta\xi)}{J_0(\beta)}X_z,$$

$$V_r = \frac{k^2 a}{2\rho\nu\beta^2}\xi p_0 - \frac{ikJ_1(\beta\xi)}{\beta J_0(\beta)}X_z, \qquad (9)$$

$$V_\theta = \frac{J_1(\beta\xi)}{J_1(\beta)}X_\theta, \quad \beta^2 = i\gamma^2 - k^2, \quad \gamma^2 = a^2\omega/\nu,$$

where p_0, X_z, and X_θ are arbitrary constants.

The substitution of Eqs. (8) and (9) into Eqs. (2)–(5) and (7) yields a homogeneous algebraic system for X_z, X_θ, and p_0. Equating the determinant of this system to zero, we arrive at the dispersion equation. Analysis of this equation and system as a whole reveals some new properties of the pulsed blood flow.

SOME RESULTS OF NUMERICAL ANALYSIS

The difficulties of numerical analysis of the problem in the model under consideration are primarily associated with the absence of the complete set of data for the determination of shell responses g_{ij}. According to available information, the possibilities of their *in vivo* experimental determination are limited. Therefore, the below results of numerical experiments should be treated as qualitative. However, it is not excluded that they are numerically correct to a certain extent for the phenomenon under investigation.

Numerical experiments were carried out for various arteries of a dog. Certain parameters were taken from

Table 1.1 in [2]. In particular, parameters a, h, ν, and E_3 are taken from this table. To obtain numerical values of g_{ij} whose analytical expressions (3) include three elastic moduli, one Poisson's ratio (independent, because $\nu_1 E_3 = \nu_3 E_1$), and parameter $x = \tan\alpha$ ($0° \le \alpha \le 90°$), one modulus (E_3) was taken from the table, and other moduli were set and varied. When fitting, the condition of the positive definiteness of matrix g_{ij} was controlled. The roots of the dispersion equation are determined for frequencies $\omega_n = 4\pi n$, where $n = 1$–9.

Numerical and asymptotic analyses showed that, for low frequencies, six complex roots $k_s^+ = k_s$, $k_2^- = -k_s$ ($\mathrm{Im}\,k_s > 0$, $s = 1, 2, 3$) always exist. Six inhomogeneous waves correspond to these roots. The general solution, where the appearance of reflected waves for a fixed ω value are disregarded, can be represented in the form

$$v_j = \sum_{s=1}^{3} C_s V_{js}(\xi) e^{i(k_s\zeta - \omega t)}, \quad p = \sum_{s=1}^{3} C_s p_s e^{i(k_s\zeta - \omega t)}, \quad (10)$$

where C_s are arbitrary constants determined by the integral values of three field characteristics (e.g., v_z, v_θ, and $\mathrm{grad}\,p$) specified at the entry for $\zeta = 0$.

The dependences of the phase velocities c_s and attenuation coefficients K_s on the parameter α were determined from the real and imaginary parts of k_s. One of the calculated phase velocities (in this case, the lowest velocity c_3) was compared with the experimental values presented in [2]. The closeness of numerical and experimental results corroborates the correct choice of the parameters to a certain extent. To estimate an effect of the rotational flow of blood, comparative analysis of $V_{rs}(1)$, $V_{zs}(1)$, and $V_{\theta s}(1)$ was performed. To this end, the α dependences of the dimensionless coefficients

$$m_{rs} = \frac{V_{rs}(1)}{V_s}, \quad m_{zs} = \frac{V_{zs}(1)}{V_s}, \quad m_{\theta s} = \frac{V_{\theta s}(1)}{V_s},$$

$$V_s = \sqrt{V_{rs}(1)^2 + V_{zs}(1)^2 + V_{\theta s}(1)^2},$$

were analyzed.

Calculations with variation of ω in the above range provided the following conclusions. First, c_s, K_s, and V_s are virtually independent of frequency. Second, the coefficient m_{rs} is much lower than the coefficients m_{zs} and $m_{\theta s}$ for any phase velocity. Third, for $\alpha = 0°$ and $90°$ (helical anisotropy is absent), $m_{\theta 1} = m_{\theta 3} = 0$, and $m_{\theta 2} \ne 0$ only if $V_{\theta s}|_{\zeta = 0} \ne 0$ at the entry; in the case of $\alpha \ne 0°$, $m_{\theta s} \ne 0$ for each wave, which testifies to the appearance and development of blood rotation upon motion of the wave along the vessel tube even if $V_{\theta 2}|_{\zeta = 0} = 0$. However, the degree of this effect on a particular wave depends strongly on the combination of parameters.
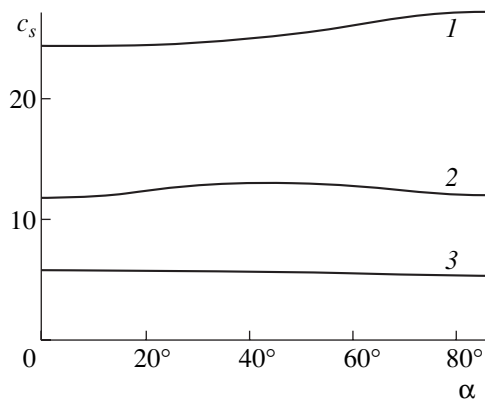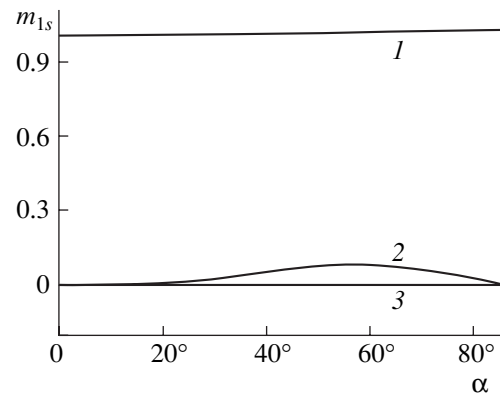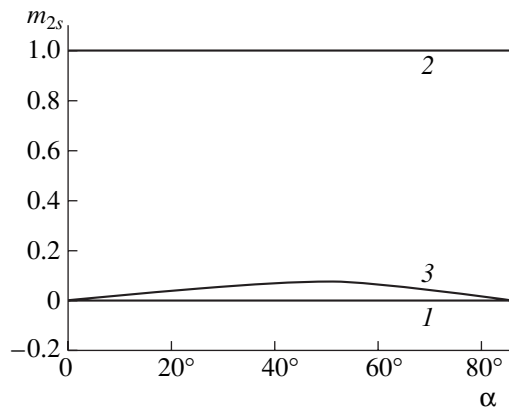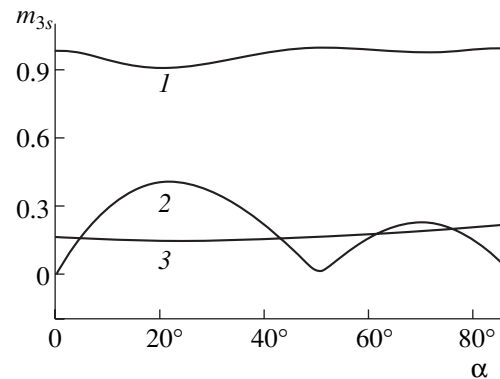
Fig. 1.

Fig. 2.

Fig. 3.

Fig. 4.

As an illustration, we present some calculation results for $\omega = 4\pi$ and an artery with the parameters $a = 0.75$ cm, $h = 0.6$ mm, $E_3 = 490.5$ kN/m^2 (according to [2], measured values are $E_3 = (3–7) \times 10^2$ kN/m^2, $E_1 = 0.833E_3$, $G = 0.25E_3$, $\nu_3 = 0.45$, $\nu_1 = 0.54$, $\rho_0 = 115$ kg/m^3, $\nu = 4$ mm^2/s, and $\rho = 102$ kg/m^3).

Figure 1 shows the α dependences of phase velocities. Line *1* corresponds to the longitudinal wave of the vessel wall ($c_1 = 24.26$ m/s) for $\alpha = 0$, line *2* is obtained for a pure torsion wave ($V_z = V_r \equiv 0$, $c_2 = 11.70$ m/s) for $\alpha = 0$, and line *3* corresponds to a pressure wave ($c_3 = 5.73$ m/s is virtually independent of α, measured values of c_3 are $c_3 = 4–6$ m/s).

Figures 2–4 show the α dependences of the coefficients (line *1*) $|m_{z1}|$, (line *2*) $|m_{\theta1}|$, and (line *3*) m_{r1}; (line *1*) $|m_{z2}|$, (line *2*) $|m_{\theta2}|$, and (line *3*) m_{r2}; and (line *1*) $|m_{z3}|$, (line *2*) $|m_{\theta3}|$, and (line *3*) $|m_{r3}|$, respectively. As is seen in Figs. 2 and 3, the coefficients m_{r1} and m_{r2} are negligibly small.

We emphasize that the coefficient of the rotational velocity component $|m_{\theta3}|$ has two pronounced maxima, $|m_{\theta3}| \simeq 0.43$ and 0.2 for $\alpha_1 \simeq 25°$ and $65°$, respectively. However, the phases of these coefficients have opposite signs, which corresponds to untwisting and twisting for

small and rather large α values, respectively, that accompany the tension of the shell and were described in [5–7].

Note. Using relation (9), one can easily see that the rotational flow of blood in any mode behaves as a boundary layer, and the degree of its localization increases with frequency.

According to the above analysis, the helical anisotropy of the elastic properties of the vessel wall can be one of the causes of the helical flow of blood.

LIST OF WEBSITES

http://vesta.ict.nsc.ru/HBC/1998/n45-46/f33/html

http://www.bio-form.ru/index_framed/files/biomer_frm/biomer_au2001.htm

http://catalysis.nsk/su/shem/medicina/_1/1_12.html

http://www-sbras.nsc.ru/HBC/2003/n17/f06/html

REFERENCES

1. N. B. Dobrov, N. B. Kuz'mina, and I. B. Roeva, Vestn. Akad. Med. Nauk SSSR, No. 6, 22 (1974).

2. T. J. Pedley, *The Fluid Mechanics of Large Blood Vessels* (Cambridge University Press, Cambridge, 1980; Mir, Moscow, 1983).

3. B. A. Purinya and V. A. Kas'yanov, *Biomechanics of Large Blood Vessels* (Znanie, Riga, 1980).

4. S. G. Lekhnitskiĭ, *Theory of Elasticity of Anisotropic Body* (Nauka, Moscow, 1977).

5. Yu. A. Ustinov, Dokl. Akad. Nauk **380**, 770 (2001) [Dokl. Phys. **46**, 756 (2001)].

6. Yu. A. Ustinov, Prikl. Mat. Mekh. **67**, 99 (2003).

7. Yu. A. Ustinov, *Saint-Venant's Problems for Pseudocylinders* (Nauka, Moscow, 2003).

8. L. G. Loĭtsyanskiĭ, *Mechanics of Fluids and Gases* (Nauka, Moscow, 1978).

Translated by R. Tyapaev